

AD-A243 649



AFIT/GE/ENG/91D-18



①

**A RIGOROUS UNIFORM DIFFRACTION
ANALYSIS OF THE ELECTROMAGNETIC
SCATTERING FROM IMPEDANCE
EDGES AND JUNCTIONS**

THESIS

Joseph Carroll Fortney, Captain, USAF

AFIT/GE/ENG/91D-18

Approved for public release; distribution unlimited



91 12 24 045

REPORT DOCUMENTATION PAGE

Form Approved
OMB No. 0704-0188

Public reporting burden for this collection of information is estimated to average 1 hour per response, including the time for reviewing instructions, searching existing data sources, gathering and maintaining the data needed, and completing and reviewing the collection of information. Send comments regarding this burden estimate or any other aspect of this collection of information, including suggestions for reducing this burden, to Washington Headquarters Services, Directorate for Information Operations and Reports, 1215 Jefferson Davis Highway, Suite 1204, Arlington, VA 22202-4302, and to the Office of Management and Budget, Paperwork Reduction Project (0704-0188), Washington, DC 20503.

1. AGENCY USE ONLY (Leave blank)		2. REPORT DATE December 1991		3. REPORT TYPE AND DATES COVERED Master's Thesis	
4. TITLE AND SUBTITLE A RIGOROUS UNIFORM DIFFRACTION ANALYSIS OF THE ELECTROMAGNETIC SCATTERING FROM IMPEDANCE EDGES AND JUNCTIONS				5. FUNDING NUMBERS	
6. AUTHOR(S) Joseph Carroll Fortney, Capt, USAF					
7. PERFORMING ORGANIZATION NAME(S) AND ADDRESS(ES) Air Force Institute of Technology WPAFB OH 45433-6583				8. PERFORMING ORGANIZATION REPORT NUMBER AFTT/GE/ENG/91D-18	
9. SPONSORING / MONITORING AGENCY NAME(S) AND ADDRESS(ES)				10. SPONSORING / MONITORING AGENCY REPORT NUMBER	
11. SUPPLEMENTARY NOTES					
12a. DISTRIBUTION / AVAILABILITY STATEMENT Approved for public release; distribution unlimited				12b. DISTRIBUTION CODE	
13. ABSTRACT (Maximum 200 words) <p>This paper investigates the scattering from impedance strips and impedance-loaded conducting strips. The impedance strips are analyzed using Senior's impedance half plane formulation. Once the primary diffraction from the impedance half plane is presented, it is used to develop multiple diffraction mechanisms on an impedance strip. The scattering from impedance-loaded strips are analyzed using Maliuzhinets' impedance wedge formulation. The primary diffraction mechanism from an impedance wedge is used to develop the multiple diffractions on an impedance double wedge. The multiple diffractions on both types of strips are developed using the Extended Spectral Ray Method. Sample calculations are made for impedance strips and impedance-loaded strips for a large purely capacitive impedance, a large purely inductive impedance, a large real impedance, and a small real impedance.</p> <p>Measurements are made for impedance strips and impedance loaded strips and are used to compare against predictions. The impedance materials used are two magnetic radar absorbing materials and two resistive materials.</p>					
14. SUBJECT TERMS Electromagnetic Scattering, Strip Scattering, Impedance loading, Impedance Measurements, Multiple Diffractions				15. NUMBER OF PAGES 119	
				16. PRICE CODE	
17. SECURITY CLASSIFICATION OF REPORT Unclassified	18. SECURITY CLASSIFICATION OF THIS PAGE Unclassified	19. SECURITY CLASSIFICATION OF ABSTRACT Unclassified	20. LIMITATION OF ABSTRACT UL		

GENERAL INSTRUCTIONS FOR COMPLETING SF 298

The Report Documentation Page (RDP) is used in announcing and cataloging reports. It is important that this information be consistent with the rest of the report, particularly the cover and title page. Instructions for filling in each block of the form follow. It is important to *stay within the lines* to meet optical scanning requirements.

Block 1. Agency Use Only (Leave blank).

Block 2. Report Date. Full publication date including day, month, and year, if available (e.g. 1 Jan 88). Must cite at least the year.

Block 3. Type of Report and Dates Covered. State whether report is interim, final, etc. If applicable, enter inclusive report dates (e.g. 10 Jun 87 - 30 Jun 88).

Block 4. Title and Subtitle. A title is taken from the part of the report that provides the most meaningful and complete information. When a report is prepared in more than one volume, repeat the primary title, add volume number, and include subtitle for the specific volume. On classified documents enter the title classification in parentheses.

Block 5. Funding Numbers. To include contract and grant numbers; may include program element number(s), project number(s), task number(s), and work unit number(s). Use the following labels:

C - Contract	PR - Project
G - Grant	TA - Task
PE - Program Element	WU - Work Unit Accession No.

Block 6. Author(s). Name(s) of person(s) responsible for writing the report, performing the research, or credited with the content of the report. If editor or compiler, this should follow name(s).

Block 7. Performing Organization Name(s) and Address(es). Self-explanatory.

Block 8. Performing Organization Report Number. Enter the unique alphanumeric report number(s) assigned by the organization performing the report.

Block 9. Sponsoring/Monitoring Agency Name(s) and Address(es). Self-explanatory.

Block 10. Sponsoring/Monitoring Agency Report Number. (If known)

Block 11. Supplementary Notes. Enter information not included elsewhere such as: Prepared in cooperation with...; Trans. of...; To be published in.... When a report is revised, include a statement whether the new report supersedes or supplements the older report.

Block 12a. Distribution/Availability Statement. Denotes public availability or limitations. Cite any availability to the public. Enter additional limitations or special markings in all capitals (e.g. NOFORN, REL, ITAR).

DOD - See DoDD 5230.24, "Distribution Statements on Technical Documents."

DOE - See authorities.

NASA - See Handbook NHB 2200.2.

NTIS - Leave blank.

Block 12b. Distribution Code.

DOD - Leave blank.

DOE - Enter DOE distribution categories from the Standard Distribution for Unclassified Scientific and Technical Reports.

NASA - Leave blank.

NTIS - Leave blank.

Block 13. Abstract. Include a brief (*Maximum 200 words*) factual summary of the most significant information contained in the report.

Block 14. Subject Terms. Keywords or phrases identifying major subjects in the report.

Block 15. Number of Pages. Enter the total number of pages.

Block 16. Price Code. Enter appropriate price code (*NTIS only*).

Blocks 17. - 19. Security Classifications. Self-explanatory. Enter U.S. Security Classification in accordance with U.S. Security Regulations (i.e., UNCLASSIFIED). If form contains classified information, stamp classification on the top and bottom of the page.

Block 20. Limitation of Abstract. This block must be completed to assign a limitation to the abstract. Enter either UL (unlimited) or SAR (same as report). An entry in this block is necessary if the abstract is to be limited. If blank, the abstract is assumed to be unlimited.

AFTT/GE/ENG/91D-18

**A RIGOROUS UNIFORM DIFFRACTION ANALYSIS
OF THE ELECTROMAGNETIC SCATTERING
FROM IMPEDANCE EDGES AND JUNCTIONS**

THESIS

**Presented to the Faculty of the School of Engineering
of the Air Force Institute of Technology**

Air University

**In Partial Fulfillment of the
Requirements of the Degree of
Master of Science in Electrical Engineering**

**Joseph Carroll Fortney, B.S.E.E
Captain, USAF**

December 1991



Accession For	
NTIS GRA&I	<input checked="checked" type="checkbox"/>
DTIC TAB	<input type="checkbox"/>
Unannounced	<input type="checkbox"/>
Justification	
By	
Distribution/	
Availability Codes	
Dist	Avail and/or Special
A-1	

Approved for public release: distribution unlimited

Acknowledgements

I would like to express my appreciation to my advisor, Captain Philip Joseph Ph.D., for his help throughout this effort. I would also like to thank the members of my thesis committee, Captain Byron Welsh Ph.D and Dr. Vittal Pyati, for their comments on this project.

There are many others who have helped me during my time at AFIT. I would like to thank Mr. Bob Lindsay for his help in making RCS and waveguide measurements; Major Dan McGrath for his numerous indispensable discussions and explanations of Impedance Boundary Conditions; and Capt Chuck Makekau for the data conversion program to change HP formatted RCS data to ANSI formatted RCS data. I would also like to thank my fellow low observables students, who were an excellent source of encouragement and support while at AFIT.

I would especially like to thank Dr. Martin I. Herman for his patience, many lengthy phone conversations, and data analysis given during this effort. This effort would not have been completed without the numerous suggestions and comments of Dr. Martin I. Herman.

I would like to thank Michelle Champion for her support and efforts to acquire my selection to AFIT.

I would like to thank my wife, Kimberly, for her patience and support during the course of this work. I would like to thank my parents, James and Mary Fortney, for giving me a strong sense of motivation, for conveying to me the value

of education, and their unwavering support in all my endeavors. I would like to thank my brother, Jon Fortney, and Daniel Carroll for their support.

Finally, I would like to thank the United States Air Force for giving me this opportunity to further my education.

Table of Contents

	page
Acknowledgements	ii
List of Figures	vii
Abstract	xi
I. Introduction	1.1
Background	1.1
Radar	1.1
Radar Cross Section	1.1
RCS Reduction	1.2
Historical Development	1.4
Method of Moments	1.4
High Frequency Techniques	1.4
Problem Statement	1.5
Summary of Remaining Chapters	1.6
II. Impedance Boundary Conditions	2.1
General Boundary Conditions	2.1
Approximate Boundary Conditions	2.2
Half Space Surface Impedance Boundary	2.3
Thin Impedance Half Plane	2.6
III. Theory	3.1
Impedance Half Plane	3.2

Impedance Strips	3.5
Single Diffraction on Resistive Strip	3.6
Double Diffraction on Resistive Strip	3.7
Triple Diffraction on Resistive Strip	3.11
Conductive and Impedance Strips	3.13
Impedance Wedge	3.14
Impedance Double Wedge	3.19
Single Diffractions	3.20
Double Diffractions	3.20
Triple Diffractions	3.24
Convex Cylindrical Polygon	3.27
Flat Impedance Structure	3.29
IV. Scattering Predictions	4.1
Diffraction Sources	4.1
Strips	4.1
Loaded Strips	4.2
Application of the Double Wedge Diffraction Mechanisms	4.4
Scattering Prediction Results	4.5
Strips	4.5
Loaded Perfectly Conducting Strips	4.6
V. Scattering Measurements	5.1
Impedance Materials	5.1

Measurement	5.2
Scattering Configurations	5.5
Target Construction	5.5
Measurements	5.6
Predictions vs Measurements	5.8
Impedance Strips	5.10
Loaded-Impedance Strips	5.23
VI. Conclusions	6.1
Summary	6.1
Recommendations for Further Study	6.4
Bibliography	BIB.1

List of Figures

Figure	Page
2.1 Impedance half space modelled as an equivalent surface impedance . . .	2.4
3.1 Geometry for an impedance half plane	3.4
3.2 Contour of integration for determination of the scattered field from and impedance half plane	3.4
3.3 Geometry for an impedance strip	3.7
3.4 Double diffraction ray mechanisms on an impedance strip	3.9
3.5 Triple diffraction ray mechanisms on an impedance strip	3.12
3.6 Geometry for an impedance wedge	3.15
3.7 Steepest descent path used in the impedance wedge formulation from the Sommerfeld contour in the complex plane	3.15
3.8 Geometry of an impedance double wedge	3.20
3.9 Double diffraction ray mechanism from Q_1 to Q_2 on an impedance double wedge	3.21
3.10 Triple diffraction ray mechanism on an impedance double wedge at Q_1	3.25
3.11 Three vertex triple diffraction ray mechanism on an impedance polygon	3.27
3.12 Geometry for the three vertex triple diffraction ray mechanism on an impedance polygon	3.30
4.1 Scattering predictions for 4λ impedance strips of impedances $j3.0$, $-j3.0$, and PEC, E-polarization	4.7
4.2 Scattering predictions for 4λ impedance strips of impedances $j3.0$, $-j3.0$, and PEC, H-polarization	4.8
4.3 Scattering predictions for 4λ impedance strips of impedances 1.2 , 6.0 , and PEC, E-polarization	4.9

4.4	Scattering predictions for 4λ impedance strips of impedances 1.2, 6.0, and PEC, H-polarization	4.10
4.5	Scattering predictions for a 4λ perfectly conducting strip and 2λ perfectly conducting strips with 1λ loads of impedances, $j3.0$ and $-j3.0$, E-polarization	4.12
4.6	Scattering predictions of a 4λ perfectly conducting strip and 2λ perfectly conducting strips with 1λ loads of impedances, $j3.0$ and $-j3.0$, H-polarization	4.13
4.7	Scattering predictions of a 4λ perfectly conducting strip and 2λ perfectly conducting strips with 1λ loads of impedances, 1.2 and 6.0, E-polarization	4.14
4.8	Scattering predictions of a 4λ perfectly conducting strip and 2λ perfectly conducting strips with 1λ loads of impedances, 1.2 and 6.0, H-polarization	4.15
5.1	Comparison of measured and predicted monostatic scattering pattern for a 4 inches by 6 inches perfectly conducting strip at 11.8 GHz, E-polarization	5.13
5.2	Comparison of measured and predicted monostatic scattering pattern for a 4 inches by 6 inches perfectly conducting strip at 11.8 GHz, H-polarization	5.14
5.3	Comparison of measured and predicted monostatic scattering pattern for a 4 inches by 6 inches, SF 10, impedance strip at 11.8 GHz, E-polarization	5.15
5.4	Comparison of measured and predicted monostatic scattering pattern for a 4 inches by 6 inches, SF 10, impedance strip with a perfect conductor backing at 11.8 GHz, E-polarization	5.16
5.5	Comparison of measured and predicted monostatic scattering pattern for a 4 inches by 6 inches, SF 10, impedance strip at 11.8 GHz, H-polarization	5.17
5.6	Comparison of measured and predicted monostatic scattering pattern for a 4 inches by 6 inches, FG 40, impedance strip at 11.8 GHz, E-polarization	5.18

5.7	Comparison of measured and predicted monostatic scattering pattern for a 4 inches by 6 inches, FG 40, impedance strip with a perfect conductor backing at 11.8 GHz, E-polarization	5.19
5.8	Comparison of measured and predicted monostatic scattering pattern for a 4 inches by 6 inches, FG 40, impedance strip at 11.8 GHz, H-polarization	5.20
5.9	Comparison of measured and predicted monostatic scattering pattern for a 4 inches by 6 inches conducting strip with 1 inch by 6 inches loads, SC 100, at 11.8 GHz, E-polarization	5.24
5.10	Comparison of measured and predicted monostatic scattering pattern for a 4 inches by 6 inches conducting strip with 1 inch by 6 inches loads, SC 100, at 11.8 GHz, H-polarization	5.25
5.11	Comparison of measured and predicted monostatic scattering pattern for a 4 inches by 6 inches conducting strip with 1 inch by 6 inches loads, VF 10, at 11.8 GHz, E-polarization	5.26
5.12	Comparison of measured and predicted monostatic scattering pattern for a 4 inches by 6 inches conducting strip with 1 inch by 6 inches loads, VF 10, at 11.8 GHz, H-polarization	5.27
5.13	Comparison of measured and predicted monostatic scattering pattern for a 4 inches by 6 inches conducting strip with 1 inch by 6 inches loads, SF 10, at 11.8 GHz, E-polarization	5.29
5.14	Comparison of measured and predicted monostatic scattering pattern for a 4 inches by 6 inches conducting strip with 1 inch by 6 inches loads, SF 10 and a perfect conductor backing at 11.8 GHz, E-polarization	5.30
5.15	Comparison of measured and predicted monostatic scattering pattern for a 4 inches by 6 inches conducting strip with 1 inch by 6 inches loads, SF 10, at 11.8 GHz, H-polarization	5.31
5.16	Comparison of measured and predicted monostatic scattering pattern for a 4 inches by 6 inches conducting strip with 1 inch by 6 inches loads, SF 10 and a perfect conductor backing at 11.8 GHz, H-polarization	5.32
5.17	Comparison of measured and predicted monostatic scattering pattern for a 4 inches by 6 inches conducting strip with 1 inch by 6 inches loads, FG 40, at 11.8 GHz, E-polarization	5.33

- 5.18 Comparison of measured and predicted monostatic scattering pattern for a 4 inches by 6 inches conducting strip with 1 inch by 6 inches loads, FG 40 and a perfect conductor backing at 11.8 GHz, E-polarization 5.34
- 5.19 Comparison of measured and predicted monostatic scattering pattern for a 4 inches by 6 inches conducting strip with 1 inch by 6 inches loads, FG 40 at 11.8 GHz, H-polarization 5.35
- 5.20 Comparison of measured and predicted monostatic scattering pattern for a 4 inches by 6 inches conducting strip with 1 inch by 6 inches loads, FG 40 and a perfect conductor backing at 11.8 GHz, H-polarization 5.36

Abstract

This paper investigates the scattering from impedance strips and impedance-loaded conducting strips. The impedance strips are analyzed using Senior's impedance half plane formulation. Once the primary diffraction from the impedance half plane is presented, it is used to develop multiple diffraction mechanisms on an impedance strip. The scattering from impedance-loaded strips are analyzed using Maliuzhinets' impedance wedge formulation. The primary diffraction mechanism from an impedance wedge is used to develop the multiple diffractions on an impedance double wedge. The multiple diffractions on both types of strips are developed using the Extended Spectral Ray Method.

Sample calculations are made for impedance strips and impedance-loaded strips for a large purely capacitive impedance, a large purely inductive impedance, a large real impedance, and a small real impedance.

Measurements are made for impedance strips and impedance loaded strips and are used to compare against predictions. The impedance materials used are two magnetic radar absorbing materials and two resistive materials.

A RIGOROUS UNIFORM DIFFRACTION ANALYSIS OF THE ELECTROMAGNETIC SCATTERING FROM IMPEDANCE EDGES AND JUNCTIONS

I. Introduction

Background

Radar. A radar operates by emitting energy in the form of an electromagnetic wave. When the emitted wave strikes an object, the object scatters the energy in all directions. The energy scattered toward the radar is received and may provide information concerning the object's position and velocity relative to the radar.

Radar Cross Section. Radar cross section (RCS) is a quantity denoting the amount of incident energy scattered by an object in a certain direction. The RCS of an object is a function of the transmitting antenna's polarization, the receiving antenna, frequency, relative orientation of the object and the radar, as well as the object's shape, size, and material properties. On the other hand, RCS is independent of range. The mathematical definition of RCS is

$$\sigma = \lim_{R \rightarrow \infty} 4\pi R^2 \left| \frac{E_s}{E_i} \right|^2 \quad (1.1)$$

where R is the distance between the radar and the object, E_s is the scattered field, and E_i is the incident field at the object.

RCS Reduction. Reducing an object's RCS decreases the ability of a radar to detect the object. Therefore, if an aircraft's RCS is reduced to a minimum, the survivability of the aircraft during a mission is increased. The four methods to reduce an object's RCS are shaping, radar absorbing material or radar absorbing structure (RAM and RAS), active cancellation, and passive cancellation (10:190).

The objective of shaping is to mold the object's surfaces and edges to deflect the scattered energy away from the radar. The disadvantages of shaping are the RCS is increased in the deflected direction, and desirable low RCS shapes may not be aerodynamic. Therefore, the designer of the shaped object must decide on directions where the increased RCS will not increase the probability of detection. For military aircraft, the airframe is shaped to deflect the energy to the side or to the back of the aircraft. Also, the airframe is designed to eliminate known sources of high RCS such as dihedral and trihedral shapes.

Radar absorbing material, which is applied to the surface of the object or aircraft, may convert the scattered energy into heat and/or form a destructive interference pattern to cancel the scattered energy. Sufficient absorption over a wide frequency range usually implies bulky electric absorber or heavy magnetic absorbers. Therefore, RAM decreases the performance of the aircraft. A radar absorbing structure (RAS) differs from RAM in that it is not an add-on treatment. A final disadvantage of RAM and RAS is high cost and complexity of the materials.

Active cancellation is the process of the aircraft detecting the incident energy - specifically its frequency, polarization, and angle of arrival - then predicting the scattered energy so interfering energy can be transmitted to cancel the scattered energy in the direction of the radar. This technique is difficult to implement considering the required energy for interference must be predicted and then transmitted.

Passive cancellation involves the application of impedance loads on the surface of the object to alter the characteristics of the scattered energy (2). The effect of the impedance load is to change the frequency response of the object by producing scattering sources which form destructive interference at certain frequencies, but not at others (4:1.4). The effect on the RCS pattern is a reduction in the sidelobe levels and mainlobe level and the creation of nulls in the pattern. Haupt and Liepa (3:57) calculated a 15 dB decrease in the edge-on scattering of a conducting strip by applying a parabolically tapered resistive load. The main disadvantage of impedance loading is that it is very frequency dependent. A main advantage of impedance loading is its potential to design low sidelobe antennas and low RCS structures.

This thesis will develop an accurate and computer efficient method to predict the scattering from impedance strips and conducting strips which are loaded with constant impedance strips.

Historical Development

Method of Moments. The method of moments can be used to solve for the currents induced on an object by an incident wave. From the induced currents, the scattered field can be calculated. Method of moments has been used to predict the scattering from resistive strips (14;17;22) and resistively loaded conducting strips (4). The method of moments is accurate, but not computer efficient. The method requires the object to be partitioned into sections which are fractions of a wavelength long. If the frequency of the incident wave is large, the object must be split up into many subsections. The method forms a linear system of N equations with N unknowns, where N is the number of subsections. The next step is to solve the system of equations using matrix theory. This requires a computer program to invert the N by N matrix. The inversion of matrices by a computer requires a great amount of computer time.

High Frequency Techniques. High frequency techniques use asymptotic series expansions and asymptotic integral evaluations to predict the scattering from objects. High frequency techniques are accurate for electrically large targets.

The geometrical theory of diffraction (GTD) developed by Keller (9) was the first high frequency technique to predict the scattering from perfectly conducting wedges. GTD uses ray tracing and yields shadowed and lit regions. At the boundaries of the shadow and lit regions, singularities in the fields exist. GTD is accurate, except in the vicinity of the shadow boundaries. The field singularities at the shadow boundaries were eliminated by Kouyoumjian and

Pathak (11) who introduced transition functions which force the fields to the correct (continuous) values across the shadow boundaries. This method is called the Uniform Theory of Diffraction (UTD).

Herman (5) has developed the diffracted fields from an impedance half plane and an impedance wedge using impedance boundary conditions (16). Using the Extended Spectral Ray Method, he developed the secondary diffraction mechanisms on impedance strips and impedance double wedges. The analysis accounts for the surface waves which are predicted by electromagnetic wave theory to exist when energy is incident on impedance materials. The impedance double wedge formulation was used to predict the scattering from impedance cylindrical polygons, impedance inserts in full plane structures, and thick impedance half planes.

Problem Statement

Accurate and computer efficient predictions of the scattering from 2 dimensional conductive strips with constant impedance loads are needed for the analysis of passive cancellation techniques for radar cross section reduction and for the analysis and design of low sidelobe parabolic reflector antennas.

The objectives of this thesis are to:

1. Develop computer subroutines that calculate the 2 dimensional edge diffraction of impedance edges and junctions.
2. Use the developed subroutines to predict the scattering patterns of 2 dimensional conductive strips with constant impedance loads and 2

dimensional impedance strips. Verify the accuracy of the subroutines against measurements.

3. Perform experimental work to verify the 2 dimensional scattering predictions.

Summary of Remaining Chapters

Chapter II explains the Impedance Boundary Conditions used in this thesis.

Chapter III presents the development of the non-uniform primary diffraction mechanisms and uniform secondary diffraction mechanisms used to predict scattering from impedance edges and junctions. Also, the modifications to the secondary diffraction mechanisms for planar surfaces are presented.

In Chapter IV, scattering predictions of impedance strips and impedance loaded perfectly conducting strips are investigated. Specifically, the scattering characteristics of purely inductive, purely capacitive, large non-reactive impedances and small non-reactive impedance strips and impedance loaded strips are presented.

In Chapter V, the accuracy of the scattering predictions for impedance strips and loaded impedance conducting strips are compared to measurements.

Finally, chapter VI presents a summary and conclusions. Recommendations for areas of further research are presented.

II. Impedance Boundary Conditions

This chapter investigates the Impedance Boundary Condition (IBC) which is an approximate boundary condition used in the analysis of electromagnetic problems. In a continuous media, Maxwell's equations are used to solve for the fields, which are assumed to be single-valued, bounded, and continuous. When two media with different electrical properties meet, the fields are no longer continuous at the interface of the two media. To solve for the fields on either side of the interface, the boundary conditions are used. Therefore using Maxwell's equations and boundary conditions, the fields for a two media problem can be solved.

General Boundary Conditions

The general boundary conditions are the classical boundary conditions applied at the interface between two media. Consider the situation of a finite body in free space with fields E_o , H_o , outside and E , H inside the body. To solve for the fields, the boundary value problem must be solved at the surface of the body using the general boundary conditions:

$$\mathbf{n} \times (\mathbf{E}_o - \mathbf{E}) = -\mathbf{M}_s \quad (2.1)$$

$$\mathbf{n} \times (\mathbf{H}_o - \mathbf{H}) = \mathbf{J}_s \quad (2.2)$$

$$\mathbf{n} \cdot (\mathbf{D}_o - \mathbf{D}) = q_{es} \quad (2.3)$$

$$\mathbf{n} \cdot (\mathbf{B}_e - \mathbf{B}) = q_{ms} \quad (2.4)$$

where

\mathbf{M}_s = magnetic surface current

\mathbf{J}_s = electric surface current

q_{ms} = electric surface charge

q_{es} = magnetic surface charge

\mathbf{n} = outward normal unit vector

Given the permittivity and permeability and geometry of the body it is possible to solve for all the fields. The solution is rigorous so it is desirable to develop another set of boundary conditions which are approximate, but accurate to a tolerable error. An approximate set of boundary conditions are the impedance boundary conditions.

Approximate Boundary Conditions

Approximate boundary conditions are used to simplify the numerical analysis of the fields when a complex structure is inside a media. The structure may be inhomogeneous, anisotropic, and have an arbitrary shape. The approximate boundary conditions simplify the numerical analysis by transforming the two media problem into a one medium problem. The material characteristics and geometry of the complex structure are accounted for in the analysis by one quantity which relates the fields at the interface. One such approximate boundary

condition is the Impedance Boundary Condition (IBC). This IBC has been applied to impedance wedges and impedance half planes.

Half Space Impedance Boundary Condition(16). The Impedance Boundary Condition was developed by Leontovich for the analysis of a plane wave incident on an infinite half space. Since the half space is infinite in extent, the Impedance Boundary Condition assumes the fields penetrating the boundary do not reemerge at some point on the boundary. The IBC is

$$\mathbf{n} \times (\mathbf{n} \times \mathbf{E}) = -\eta Z_0 \mathbf{n} \times \mathbf{H} \quad (2.5)$$

where

\mathbf{n} = outward normal unit vector of the half space

\mathbf{E} = Electric field just above the interface

\mathbf{H} = Magnetic field just above the interface

η = the quantity accounting for the electrical properties of the material half space, called the surface impedance.

Z_0 = the characteristic impedance of the surrounding media.

Figure 2.1 graphically shows the boundary where the IBC is applied. The IBC transforms the impedance half space into an equivalent impenetrable impedance surface with a surface impedance of η .

The surface impedance, η , is a quantity which is not given a value by Leontovich. It depends on the electrical properties of the boundary where the

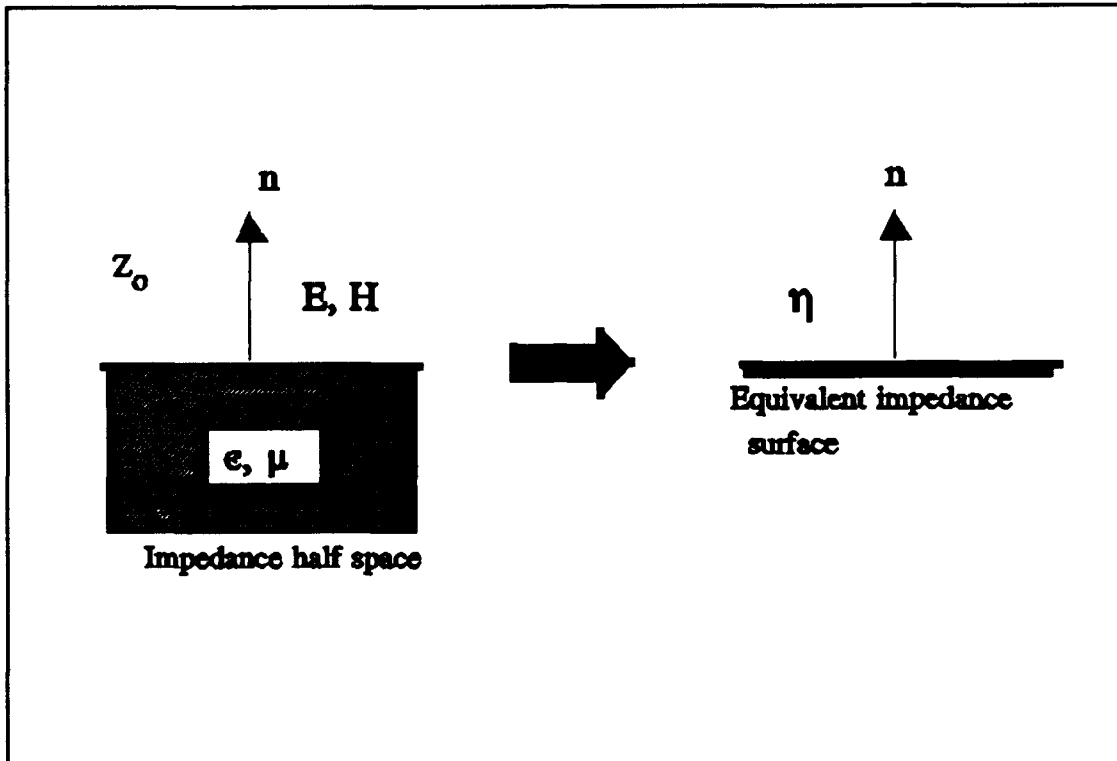


Figure 2.1. Impedance half space modelled as an equivalent impedance surface.

approximate boundary condition is applied. Therefore, the surface impedance is a quantity which must be modelled by the user and usually involves an approximation.

One way to derive an appropriate surface impedance, η , is to demand that the equivalent impedance surface satisfying Eq (2.5) reproduce the same reflected field as the half space does. In doing so for the planar half space, the value of the surface impedance can be approximated as

$$\eta = \sqrt{\frac{\mu}{\epsilon}} \quad (2.6)$$

where

ϵ = the complex permittivity of the half space

μ = the complex permeability of the half space

The use of a constant value for η does not allow the equivalent impedance surface to produce the correct reflected field as the angle of incidence varies. However, if the refractive index of the material half space is large in magnitude, then setting η to a constant is a good approximation for all but large oblique angles of incidence. This constraint on the refractive index ensures the wave in the half space travels normal to the interface for all incident angles. The value for the surface impedance in Eq (2.6) can also be used for a curved boundary provided

$$|Im(\sqrt{\epsilon \mu})| k_o \rho_i > 1 \quad (2.7)$$

where ρ_i are the principal radii of curvature associated with the surface. The condition in Eq (2.7) ensures the material is sufficiently lossy so that the fields penetrating the surface do not reemerge at some other point on the surface.

For a perfectly conducting body, $\eta = 0$, and the I.B.C. satisfies the general boundary conditions.

The IBC for the half space is the IBC which can be used for the analysis of

the scattering from an impedance wedge. Using the half space IBC, the impedance wedge is simulated by a thin impedance surface having the same wedge angle as the original impedance wedge. The surface impedance of the wedge is approximated to be the surface impedance in Eq (2.6).

Thin Impedance Half Plane (5). Senior has applied the Impedance Boundary Condition to a thin impedance half plane. A thin impedance half plane is a half plane with arbitrary permeability, arbitrary permittivity, thickness less than the wavelength of the incident field, and thickness greater than the skin depth of the material. The constraint requiring the thickness be less than the wavelength ensures that there are no normal polarization currents in the half plane; only tangential currents exist. The other constraint requiring the thickness be greater than the skin depth ensures no fields reemerge from the half plane.

The method of applying the IBC to the half plane is to replace the half plane with an equivalent impenetrable impedance sheet having a surface impedance of η and a magnetic current and an electric current on the surface. Senior has shown that both the electric and magnetic tangential fields on the impedance sheet are discontinuous across the impedance sheet by an electric current and a magnetic current, respectively. In addition, Senior has shown that the IBC becomes

$$\begin{aligned} \mathbf{n} \times [\mathbf{n} \times (\mathbf{E}_+ + \mathbf{E}_-)] &= -\eta Z_0 \mathbf{n} \times (\mathbf{H}_+ - \mathbf{H}_-) \\ \mathbf{n} \times [\mathbf{n} \times (\mathbf{H}_+ + \mathbf{H}_-)] &= \frac{1}{\eta Z_0} \mathbf{n} \times (\mathbf{E}_+ - \mathbf{E}_-) \end{aligned} \quad (2.8)$$

where

\mathbf{n} = the outward unit normal vector on the sheet

\mathbf{E}_+ = electric field on top of the sheet

\mathbf{E}_- = electric field on the bottom of the sheet

\mathbf{H}_+ = magnetic field on the top of the sheet

\mathbf{H}_- = magnetic field on the bottom of the sheet

Z_o = the impedance of the surrounding media

The first IBC in Eq (2.8) is derived directly from Eq (2.5) whereas the second IBC in Eq (2.8) is derived from Eq (2.5) using duality. Using the general boundary conditions, the electric current, \mathbf{J}_e , and magnetic current, \mathbf{J}_m , on the impedance sheet are

$$\begin{aligned}\mathbf{J}_e &= \mathbf{n} \times (\mathbf{H}_+ - \mathbf{H}_-) \\ \mathbf{J}_m &= -\mathbf{n} \times (\mathbf{E}_+ - \mathbf{E}_-)\end{aligned}\tag{2.9}$$

A special case of the thin impedance half plane is a pure dielectric half plane where the relative permeability of the material is unity. For this case the impedance material only supports an electric current and the sheet is called "resistive." The IBC for the "resistive" sheet is

$$\begin{aligned}\mathbf{n} \times (\mathbf{E}_+ - \mathbf{E}_-) &= 0 \\ \mathbf{n} \times (\mathbf{n} \times \mathbf{E}) &= -R_e \mathbf{J}_e\end{aligned}\tag{2.10}$$

where

E_+ = the electric field on the top of the sheet

E_- = the electric field on the bottom of the sheet

\mathbf{n} = the outward normal on the sheet

\mathbf{E} = the total electric field on the top of the sheet

\mathbf{J}_e = the electric current on the sheet

R_e = the resistance of the sheet

Another special case of a thin impedance sheet is a pure ferrite sheet which has a relative permittivity of unity. For this special case, the impedance sheet only supports a magnetic current: this type of sheet is called "conductive." The IBC for a "conductive" sheet is

$$\begin{aligned} \mathbf{n} \times (\mathbf{H}_+ - \mathbf{H}_-) &= 0 \\ \mathbf{n} \times (\mathbf{n} \times \mathbf{H}) &= -R_m \mathbf{J}_m \end{aligned} \quad (2.11)$$

where

\mathbf{H}_+ = the magnetic field on the top of the sheet

\mathbf{H}_- = the magnetic field on the bottom of the sheet

\mathbf{H} = the total magnetic field on top of the sheet

R_m = the conductance of the sheet

Senior has shown that the two current sheets that exist on a thin impedance sheet are uncoupled. Therefore, a thin impedance half plane can be modelled as the superposition of a partially transparent "resistive" sheet obeying the IBC in Eq (2.10) and a partially transparent "conductive" sheet obeying the IBC in Eq (2.11). Therefore, combining the "resistive" sheet and "conductive"

sheet IBCs, the IBC for the impedance sheet is

$$\begin{aligned} \mathbf{n} \times [\mathbf{n} \times (\mathbf{E}_+ + \mathbf{E}_-)] &= -2Z_o R_e \mathbf{n} \times (\mathbf{H}_+ - \mathbf{H}_-) \\ \mathbf{n} \times [\mathbf{n} \times (\mathbf{H}_+ + \mathbf{H}_-)] &= 2Y_o R_m \mathbf{n} \times (\mathbf{E}_+ - \mathbf{E}_-) \end{aligned} \quad (2.12)$$

The resistance and conductance of the two sheets are related to the surface impedance of the total impedance sheet by $R_e = \eta/2$ and $R_m = 1/2\eta$, respectively. If the values of R_e and R_m are substituted into Eq (2.12), the IBC reduces to the original impedance sheet IBC in Eq (2.8). The relationship between R_e and R_m is $4R_e R_m = 1$ which is called the opaque condition.

Another concern is the value of R_e and R_m in terms of the material properties of the impedance sheet. These values can be found by using the volume equivalence theorem from basic electromagnetic theory. The layer will be assumed to lie in the x-z plane.

An impedance layer with a relative permeability of one is a pure dielectric layer which will only support an electric current. Using the volume equivalence theorem, the layer can be replaced by the equivalent directional currents, \mathbf{J}_{eq} .

$$\begin{aligned} J_{x,eq} &= jk_o Y_o (\epsilon_r - 1) E_x \\ J_{y,eq} &= jk_o Y_o (\epsilon_r - 1) E_y \\ J_{z,eq} &= jk_o Y_o (\epsilon_r - 1) E_z \end{aligned} \quad (2.13)$$

where

k_o = the wavenumber of free space

E = the electric field inside the layer

Y_o = the admittance of free space

The sheet is considered to be thin so J_y can be neglected and the current densities

$J_{x,z}$ can be replaced by the sheet currents, $J_{s,(x,z)}$

$$J_{s,x} = \tau J_{x,eq} \quad J_{s,z} = \tau J_{z,eq} \quad (2.14)$$

Using Eqn (2.13) in (2.14), the following equations are derived

$$E_x = Z_o R_s J_{s,x} , \quad E_z = Z_o R_s J_{s,z} \quad (2.15)$$

where

$$R_s = \frac{-j}{k_o \tau (\epsilon_r - 1)} \quad (2.16)$$

and

R_s = resistance of the sheet

$E_{x,z}$ = the tangential electric fields on the sheet

Z_o = the free space impedance

k_o = the free space wave number

τ = the layer thickness

ϵ_r = relative permittivity of the layer

The same analysis can be used for an impedance sheet having a relative permittivity of unity. This is the case of a perfect ferrite. Using duality, the sheet

would have a conductance, R_m , of

$$R_m = \frac{-j}{k_o \tau (\mu_r - 1)} \quad (2.17)$$

where

μ_r = the relative permeability of the layer.

III. Theory

This chapter presents the development of the diffracted fields for impedance strips, impedance double wedges, and multiple impedance double wedges (convex polygons). The single, double, and triple diffractions for the impedance strip and impedance double wedge are presented, but for the multiple impedance double wedge there is another diffraction considered. This other diffraction is a three vertex triple diffraction.

Before the diffracted fields can be presented for a strip, the diffracted field from a half plane must be derived. The multiple diffracted fields can be derived on a strip using the Extended Spectral Ray Method (ESRM) and the diffracted field from an impedance half plane. Likewise, the diffracted field from an impedance wedge must be derived before the multiple diffractions on a double wedge can be derived.

The impedance boundary condition for the impedance half plane is used to derive the diffracted fields for the strip and the half space impedance boundary condition is used in the analysis of the impedance wedge. Both of these boundary conditions are presented in Chapter 2.

Finally, the time convention assumed in this thesis is $\exp(j\omega t)$ and all impedances are assumed to have a positive real part such that all impedance materials are passive.

Impedance Half Plane(5:7-35)

As discussed in Chapter 2, an impedance half plane can be analyzed as the sum of a "resistive" half plane and a "conductive" half plane. The "resistive" half plane produces the fields from the electric current on the half plane and the "conductive" half plane produces the fields from the magnetic current on the half plane. Senior (19) has shown that for the case of the impedance half plane the magnetic currents and electric currents are uncoupled.

For an E-polarized plane wave normally incident on the impedance half plane shown in figure 3.1, Senior (19) derived an integral representation for the scattered field as

$$E^s = \frac{-j}{2\pi} \int_C \frac{1}{\cos\alpha + \cos\phi_0} [1 \mp \eta \sqrt{(1 + \cos\alpha)(1 + \cos\phi_0)}] K_+(\alpha) K_+(\phi_0) e^{-jk\rho \cos(\alpha - \phi)} d\alpha; \quad y > 0 \quad (3.1)$$

where the contour of integration is shown in figure 3.2, ϕ is the observation angle, ϕ_0 is the incident angle, η is the normalized impedance, and $K_+(\alpha)$ is the split function, defined by

$$K_+(\alpha) = 2^{\frac{2}{3}} \sqrt{\frac{2}{\eta}} \sin\left(\frac{\alpha}{2}\right) \left\{ \frac{\Psi_{\pi}\left(\frac{3\pi}{2} - \alpha - \theta\right) \Psi_{\pi}\left(\frac{\pi}{2} - \alpha + \theta\right)}{\Psi_{\pi}^2\left(\frac{\pi}{2}\right)} \right\}^2$$

$$/ \{ [1 + \sqrt{2} \cos\left(\frac{\frac{\pi}{2} - \alpha + \theta}{2}\right)] [1 + \sqrt{2} \cos\left(\frac{\frac{3\pi}{2} - \alpha - \theta}{2}\right)] \}$$
(3.2)

and

$$\Psi_{\pi}(z) \approx \begin{cases} 1 - 0.0139z^2, & \text{Im}(z) \leq 4.2 \\ 1.05302 \sqrt{\cos\left[\frac{1}{4}(z - j\ln 2)\right]} \exp\left[\frac{jz}{2\pi} e^{jz}\right], & \text{Im}(z) > 4.2 \end{cases}$$
(3.3)

provided $\text{Re}(z) < \pi/2$; otherwise, the following identities must be used as many times as needed until the argument is in the form useable by Eq (3.3).

$$\Psi_{\pi}(z) = [\Psi_{\pi}\left(\frac{\pi}{2}\right)]^2 \frac{\cos\left(\frac{z}{4} - \frac{\pi}{8}\right)}{\Psi_{\pi}(z - \pi)},$$
(3.4)

$$\Psi_{\pi}(-z) = \Psi_{\pi}(z),$$
(3.5)

$$\Psi_{\pi}(z^*) = \Psi_{\pi}^*(z),$$
(3.6)

where the asterisk denotes the complex conjugate.

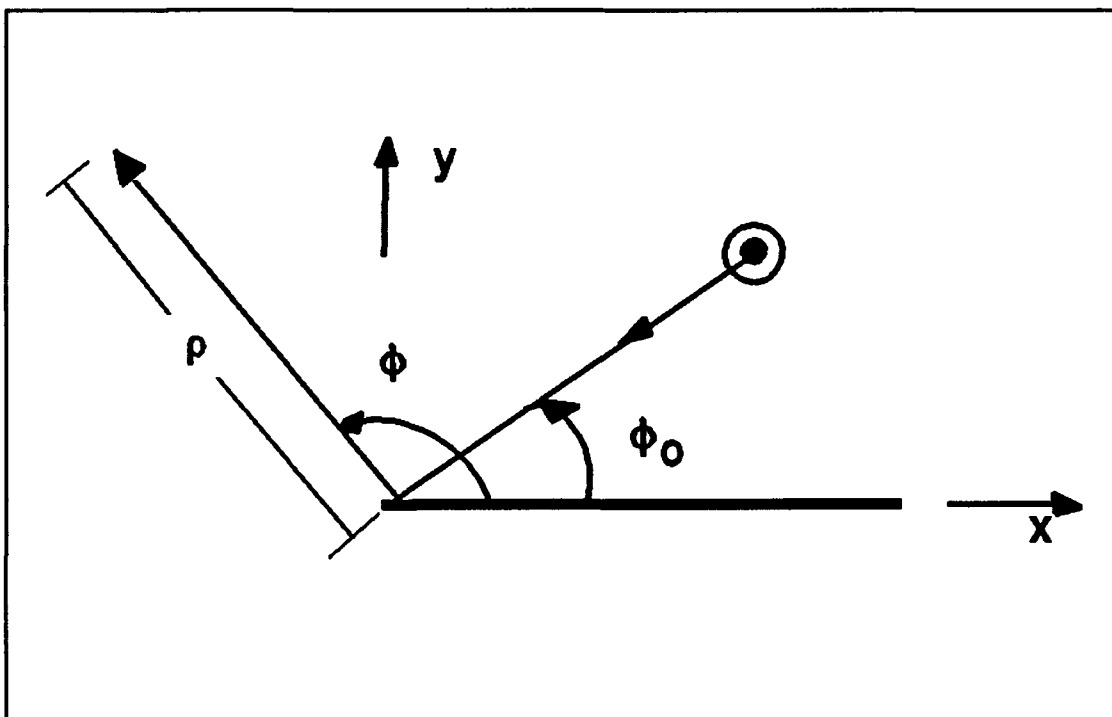


Figure 3.1. Geometry for an impedance half plane.

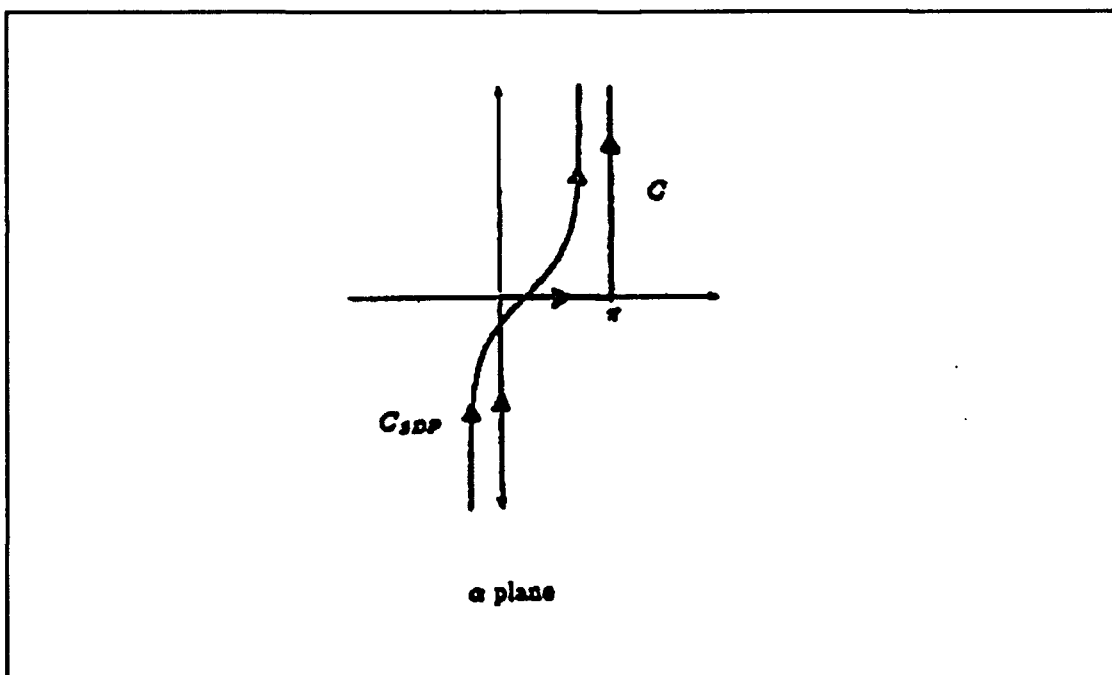


Figure 3.2. Contour of integration for determination of the scattered field from an impedance half plane.

This is a highly accurate approximation for the Maliuzhinets function, $\Psi_{\pi}(z)$, and was developed by Volakis and Senior (27). The variable θ above is related to the normalized surface impedance. For E-polarization, $\sin \theta = 1/\eta$, whereas for H-polarization $\sin \theta = \eta$.

Herman (5) performs an asymptotic non-uniform evaluation of the integral in Eq (3.1) using a technique developed by Volakis and Herman (7). Since one is concerned with plane wave incidence and far field observation, a non-uniform solution is sufficient. The non-uniform evaluation of Eq (3.1) gives

$$E^s(\phi, \phi_o) = -\frac{j}{2\pi} \sqrt{\frac{2\pi}{k\rho}} e^{\frac{\pi}{4}} e^{-jk\rho \cos\phi} \left\{ \frac{1}{\cos\phi + \cos\phi_o} \right\} \quad (3.7)$$

$$* \{ 1 \mp \eta \sqrt{(1 + \cos\phi)(1 + \cos\phi_o)} \} * K_+(\phi) K_-(\phi_o) e^{jkr}; \quad y \gtrless 0$$

where r is a phase factor to be used when the diffracted field is applied to an impedance strip. In this evaluation, the normalized surface impedance is assumed to be constant for all incident angles.

In Eq (3.8), the terms multiplied by η are associated with the "conductive" half plane while the rest of the terms are associated with the "resistive" half plane.

Impedance Strips

Herman (5:33-88) develops the single, double, and triple diffraction mechanisms on a resistive strip which rigorously accounts for the surface wave interactions. Since the electric and magnetic currents on an impedance strip are uncoupled, Herman solves for the resistive strip which is an easier formulation

and then uses the resistive diffractions to solve for the conductive strip diffractions. Once both the conductive strip and resistive strip diffractions are known, the impedance strip diffractions are found by the summation of the conductive and resistive diffractions. The Extended Spectral Ray Method (ESRM) is used to derive the double and triple diffractions on the resistive strip. The traditional method to solve for double and triple diffractions is to repeatedly employ a uniform diffraction coefficient with the incident field being the diffracted field from a previous edge. This method requires all incident fields be ray-optical which is not satisfied when the argument of the transition function in the diffracted field is small. The ESRM is used to eliminate the problem.

The ESRM is a generalization of the Spectral Theory of Diffraction (STD) (5:29). The STD states a field can be represented as an integral or summation of spectral plane waves. Tiberio (23) has shown that a field diffracted by an edge can be interpreted as an infinite sum of inhomogeneous plane waves, each of which has a ray representation. The application of the ESRM to double diffractions is to write the incident field on a second edge as an integral of inhomogeneous plane waves, then multiply the integrand by the known plane wave diffraction coefficient after its analytic continuation in the complex plane.

Single Diffraction on Resistive Strip. Consider the strip shown in figure 3.3. The scattered field in Eq (3.7) can be used to find the single diffracted field at edge Q_1 or edge Q_2 , where r is a phase factor. If Q_1 is taken as the phase reference in figure 3.3, the phase factor is zero for the singularly diffracted field at Q_1 and is $-w(\cos \phi_o + \cos \phi)$ for the singularly diffracted field at Q_2 . Herman (5)

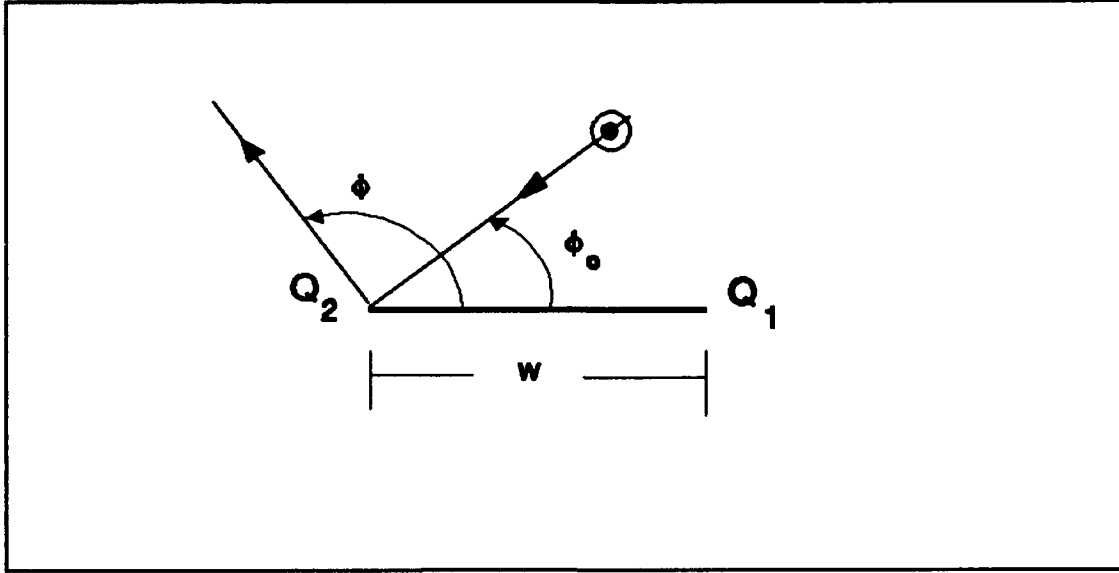


Figure 3.3. Geometry for an impedance strip.

considers the resistive strip component of Eq (3.7) to solve for the double and triple diffracted fields for a resistive strip.

Double Diffraction on Resistive Strip. The double diffracted field results when the incident field diffracts from Q_1 or Q_2 and then is diffracted again at Q_2 or Q_1 , respectively. There are four possible mechanisms for the double diffraction. Two travel on the top of the strip and two travel on the bottom of the strip. The four mechanisms are graphically shown in figure 3.4.

The exact integral representation of the field incident at Q_2 after diffraction at Q_1 is

$$E_1 = -\frac{j}{2\pi} \int_{s(0)}^{\infty} \frac{\sin \frac{\alpha}{2}}{\cos \phi + \cos \phi_o} K_{+c}(\alpha) K_{+}(\phi_o) e^{-jk\rho \cos(\alpha)} d\alpha \quad (3.8)$$

where

$$K_{\pm c}(\pm \alpha) = \frac{K_{\pm}(\pm \alpha)}{\sin(\pm \frac{\alpha}{2})} \quad (3.9)$$

Herman (5:37) states that Eq (3.8) is a complex plane wave diffracting from Q_1 at an angle α . Then using the ESRM, the field is a plane wave incident on Q_2 at an angle of $-\alpha$. Eq (3.9) can be evaluated non-uniformly as

$$E_2 = \frac{j}{2} \pi \sqrt{\frac{2\pi}{k\rho}} e^{\frac{j\pi}{4}} e^{-jk\rho} \frac{\sin(\frac{\alpha}{2})}{\cos \alpha + \cos \phi_2} K_{\pm c}(-\alpha) K_{\pm}(\phi_2) \quad (3.10)$$

where the angle ϕ_2 is measured from the strip at Q_2 .

Keeping with the ESRM, the integrand of Eq (3.8) can be multiplied by Eq (3.10) to yield the double diffracted field from edge Q_1 to edge Q_2 . Applying the ESRM yields the double diffracted field to be

$$E_{21}^d(\phi_2, \phi_o) = \frac{-\sqrt{2\pi} e^{\frac{j\pi}{4}} e^{-jk\rho}}{4\pi^2 \sqrt{k\rho}} \int_{S(0)} \frac{-\sin^2(\frac{\alpha}{2}) K_{\pm c}(-\alpha) K_{\pm c}(\alpha)}{[\cos \alpha + \cos \phi_o][\cos \alpha + \cos \phi_2]} \\ * K_{\pm}(\phi_o) K_{\pm}(\phi_2) e^{-jk\rho \cos \alpha} d\alpha \quad (3.11)$$

This integral can be evaluated asymptotically using the Method of Steepest Descents. Upon integration of Eq (3.11), the final double diffracted field is

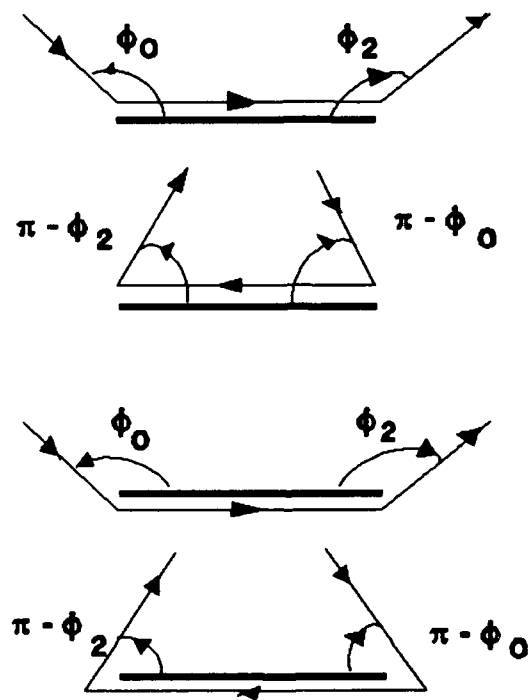


Figure 3.4. Double diffraction ray mechanisms on an impedance strip.

$$E_{21}^d(\phi_2, \phi_o) = j \frac{K_+(\phi_o) K_+(\phi_2)}{4\pi k} K_{+c}^2(0) a_3 e^{-jk_w} e^{-jk_p} \sqrt{\frac{1}{\rho w}} \quad (3.12)$$

$$* [A\{1 - F_{KP}(kwa_1)\} + B\{1 - F_{KP}(kwa_2)\} + C\{1 - F_{KP}(kwa_3)\}]$$

where

$$a_1 = 2 \cos^2\left(\frac{\phi_o}{2}\right) \quad (3.13)$$

$$a_2 = 2 \cos^2\left(\frac{\phi_2}{2}\right) \quad (3.14)$$

$$a_3 = 2 \cos^2\left(\frac{\theta}{2}\right) \quad (3.15)$$

$$A = -\frac{1}{(a_2 - a_1)(a_3 - a_1)} \quad (3.16)$$

$$B = -\frac{1}{(a_1 - a_2)(a_3 - a_2)} \quad (3.17)$$

$$C = -\frac{1}{(a_1 - a_3)(a_2 - a_3)} \quad (3.18)$$

and

$$F_{KP}(z^2) = \pm 2jz F_C(\pm z) \quad (3.19)$$

which is the Kouyoumjian and Pathak (11) UTD transition function in terms of

the Clemmow transition function

$$F_C(\pm z) = e^{k^2 z} \int_0^{\pm z} e^{-k^2 \tau} d\tau \quad (3.20)$$

which satisfies the identity

$$F_C(-z) = \sqrt{z} e^{-j\frac{\pi}{4}} e^{k^2 z} - F_C(z) \quad (3.21)$$

essential for maintaining total field continuity. In Eq (3.20), the minus sign is chosen when the argument of z is greater than $\pi/4$ and less than $5\pi/4$, otherwise the positive sign is used.

Triple Diffraction on Resistive Strip. Now the triple diffractions on the strip are presented. There are eight different triple diffractions on a strip. Four propagate from Q_1 to Q_2 and back to Q_1 . Another four are from Q_2 to Q_1 and back to Q_2 . All sets of four triple diffractions are of equal strength. Graphically, these eight diffractions are shown in figure 3.5.

Herman (5:40-43) uses the double diffracted field and the ESRM to derive the triple diffractions. The triple diffracted field is given by

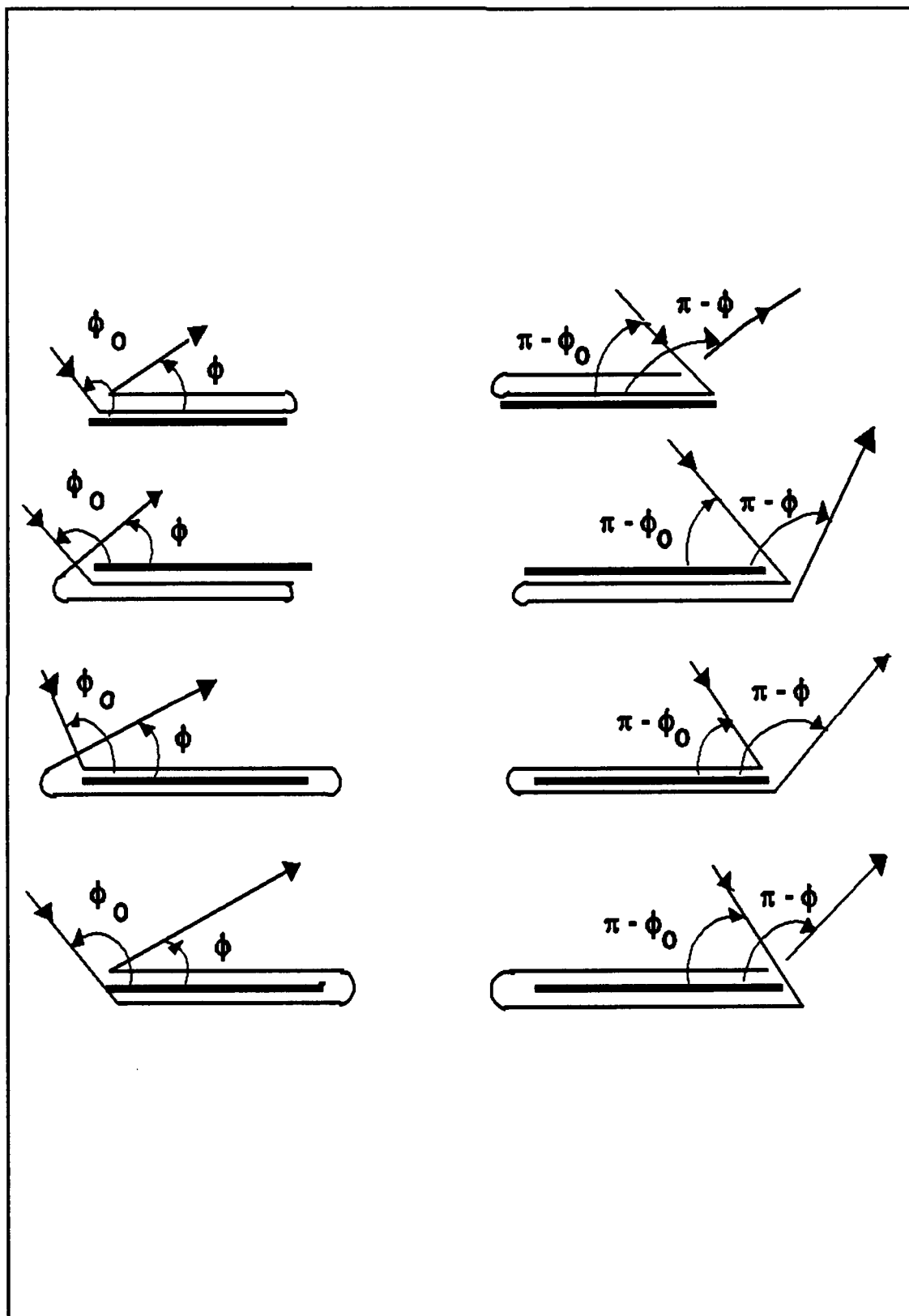


Figure 3.5. Triple diffraction ray mechanisms on an impedance strip.

$$\begin{aligned}
E_{121}^d(\phi, \phi_o) = & j \frac{\sqrt{2}}{16(k\pi)^{\frac{3}{2}}w} e^{\frac{3\pi}{4}} e^{-j2kw} K_{\frac{3}{2}}^A(0) a_3^2 K_{\frac{3}{2}}(\phi_o) K_{\frac{3}{2}}(\phi) \\
& \left[\frac{1}{(2-a_1)(a_3-a_1)} \{1 - F_{KP}(kwa_1)\} + \frac{1}{(a_1-2)(a_3-2)} \{1 - F_{KP}(kwa_2)\} \right. \\
& \quad \left. + \frac{1}{(a_1-a_3)(2-a_3)} \{1 - F_{KP}(kwa_3)\} \right] \\
& * \frac{1}{(a_3-a_4)} \{F_{FP}(kwa_3) - F_{KP}(kwa_4)\} \frac{e^{-jk\rho}}{\sqrt{\rho}}
\end{aligned} \tag{3.22}$$

where

$$a_4 = 2\cos^2\left(\frac{\phi}{2}\right) \tag{3.23}$$

Conductive and Impedance Strips. Herman (5:44-46) derives the double and triple diffractions of the conductive and impedance strips from the resistive strip's double and triple diffractions, respectively.

The double diffracted fields for the conductive strip and impedance strip are

$$E_{21_{conductive}}^d = 4\eta^2 \cos\left(\frac{\phi_o}{2}\right) \cos\left(\frac{\phi_2}{2}\right) E_{21}^d(\phi_2, \phi_o) \tag{3.24}$$

$$E_{21_{impedance}}^d = E_{21_{conductive}}^d(\phi_2, \phi_o) + E_{21}^d(\phi_2, \phi_o)$$

where $E_{21}^d(\phi, \phi_o)$ is given in Eq (3.12).

Likewise, the triple diffracted fields for the conductive strip and impedance strip are

$$E_{121_{\text{conductive}}}^d(\phi, \phi_o) = -8\eta^3 \cos\left(\frac{\phi_o}{2}\right) \cos\left(\frac{\phi}{2}\right) E_{121}^d(\phi, \phi_o) \quad (3.25)$$

$$E_{121_{\text{impedance}}}^d = E_{121_{\text{conductive}}}^d(\phi, \phi_o) + E_{121}^d(\phi, \phi_o)$$

where $E_{121}^d(\phi, \phi_o)$ is given in Eq (3.22).

Impedance Wedge

Maliuzhinets (12) derived the integral representation of the diffracted field for a solid isolated wedge, shown in figure 3.6, when illuminated by a plane wave

$$\left. \begin{matrix} E_z^i \\ H_z^i \end{matrix} \right\} = e^{jk(x \cos \phi_o + y \sin \phi_o)} \quad (3.26)$$

When the illuminating plane wave is E_z , the incident wave is called E-polarization (horizontal polarization). The other case, when the illuminating plane wave is H_z , is called H-polarization (vertical polarization). This integral representation is

$$u_1^d(\phi, \phi_o) = \frac{-\sin\left(\frac{\phi_o}{n}\right)}{2n\pi j \Psi(\Phi - \phi_o)} \int_c \left[\frac{\Psi(\alpha + \Phi - \phi)}{\cos\left(\frac{\alpha - \phi}{n}\right) - \cos\left(\frac{\phi_o}{n}\right)} \right] e^{jk\rho \cos \alpha} d\alpha \quad (3.27)$$

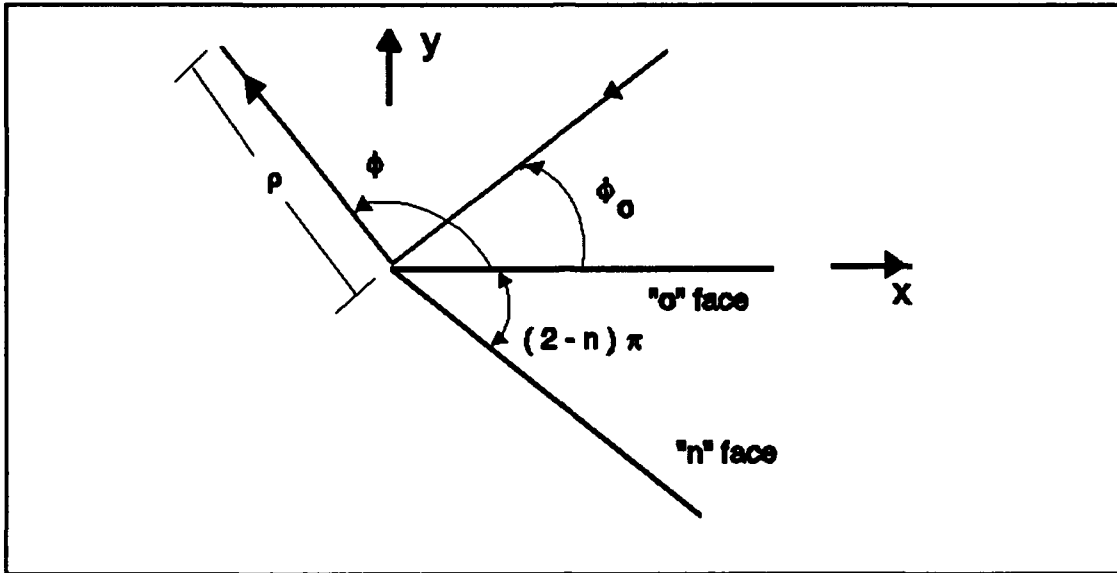


Figure 3.6. Geometry for an impedance wedge.

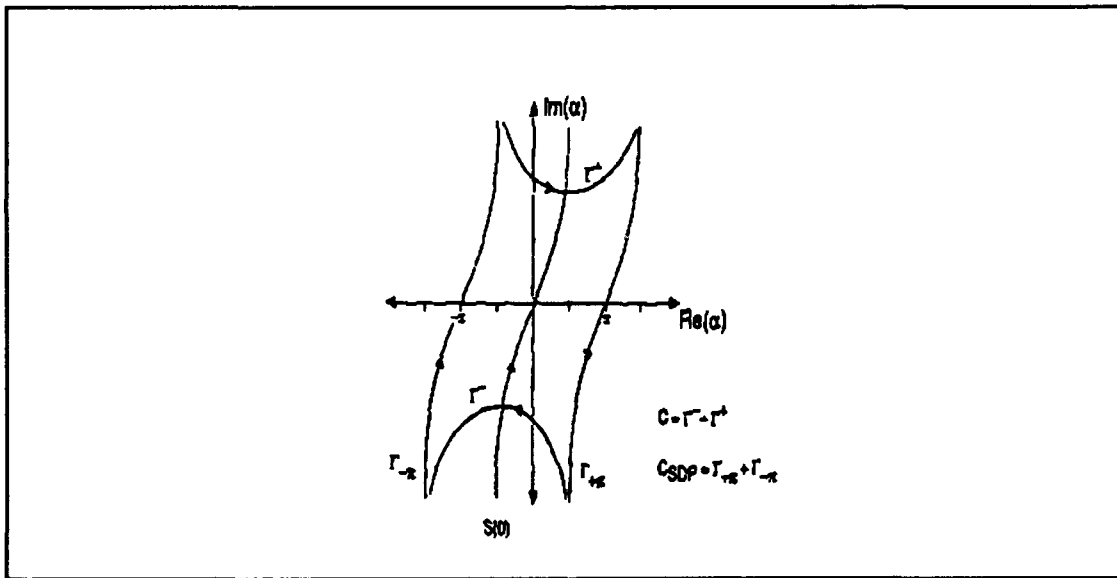


Figure 3.7. Steepest descent path used in the impedance wedge formulation from the Sommerfeld contour in the complex plane.

where C is the Sommerfeld contour shown in figure 3.7, 2Φ is the external wedge angle ($\Phi = n\pi/2$), ϕ is the observation angle, ϕ_0 is the incident angle, and u^d represents either E_z or H_z . The function, $\Psi(\alpha)$, is called the Maliuzhinets meromorphic function and is defined as

$$\Psi(\alpha) = \Psi_{\Phi}(\alpha + \Phi + \frac{\pi}{2} - \theta^+) \Psi_{\Phi}(\alpha - \Phi - \frac{\pi}{2} + \theta^-) \Psi_o(\alpha) \quad (3.28)$$

where Ψ_o is given by

$$\Psi_o = \Psi_{\Phi}(\alpha + \Phi - \frac{\pi}{2} + \theta^+) \Psi_{\Phi}(\alpha - \Phi \frac{\pi}{2} - \theta^-) \quad (3.29)$$

and

$$\theta^{\pm} = \begin{cases} \sin^{-1}(\frac{1}{\eta}) & E\text{-}Pol. \\ \sin^{-1}(\eta) & H\text{-}Pol. \end{cases} \quad (3.30)$$

where η is the equivalent surface impedance of the material normalized to free space impedance, 377 Ω . The plus and minus superscripts on θ corresponds to the "o" face and "n" face of the wedge, respectively.

The function Ψ_{Φ} is defined by Maliuzhinets (12) as

$$\Psi_{\Phi}(z) = \exp\left[-\frac{j}{8\Phi} \int_0^z \int_{-\infty}^{\infty} \tan\left(\frac{\pi v}{4\Phi}\right) \frac{du dv}{\cos(v-u)}\right] \quad (3.31)$$

Until recently, the evaluation of the integral in Eq (3.31) has not been possible for an arbitrary wedge angle. Volakis and Senior (27) have derived accurate approximations for the integral in Eq (3.31). For small arguments of z ,

$$\Psi_{\Phi}(z) \approx 1 - z^2 \left(\frac{\delta}{\Phi^2} \right) \quad (3.32)$$

where $\delta = 0.04626 + 0.054\Phi - 0.0078\Phi^2$ and for large arguments,

$$\Psi_{\Phi}(z) \approx \sqrt{\cos\left(\frac{\pi z}{4\Phi}\right)} e^{-\frac{\gamma}{\pi}} \quad (3.33)$$

where $\gamma = 2.556343\Phi - 3.259678\Phi^2 + 1.659306\Phi^3 - 0.3883548\Phi^4 + 0.03473964\Phi^5$.

When the imaginary part of z is greater than 4 for the large argument form, or less than 4 for the small argument form, these approximations provide less than two percent error (4:92). The approximations will give 0.5 percent error provided the argument in Eq (3.33) has an imaginary part greater than 10. For arguments with imaginary parts less than 10 and for 0.5 percent error, a five point numerical integration is required

$$\Psi_{\Phi}(z) = \exp\left[-\frac{1}{2}(u + jv)\right] \quad (3.34)$$

where

$$u = 0.3 \sum_{n=1}^5 \frac{\cosh[\xi x] \cos[\xi y] - 1}{\xi \cosh\left[\frac{\pi \xi}{2}\right] \sinh[2\Phi \xi]} \quad (3.35)$$

$$v = 0.3 \sum_{n=1}^5 \frac{\sinh[\xi x] \sin[\xi y] - 1}{\xi \cosh[\frac{\pi \xi}{2}] \sinh[2\Phi \xi]} \quad (3.36)$$

and $z = x + jy$, $\xi = 0.3n - 0.15$.

To simplify the analysis, the Sommerfeld contour shown in figure 3.7 can be deformed so that Eq (3.27) can be recast as

$$u_1^d(\phi, \phi_o) = \frac{j}{2\pi n} \int_{c_{SDP}} \frac{\sin(\frac{\phi_o}{n})}{\Psi(\Phi - \phi_o)} e^{-jk\rho \cos \alpha} \left\{ \frac{\Psi(\alpha + \pi + \Phi - \phi)}{\cos(\frac{\alpha + \pi - \phi}{n}) - \cos(\frac{\phi_o}{n})} - \frac{\Psi(\alpha - \pi + \Phi - \phi)}{\cos(\frac{\alpha - \pi - \phi}{n}) - \cos(\frac{\phi_o}{n})} \right\} d\alpha \quad (3.37)$$

Herman (5) states the first order asymptotic evaluation of Eq (3.37) corresponds to the diffracted field from an isolated wedge whose non-uniform solution is

$$u_1^d(\phi, \phi_o) = \frac{j}{2\pi n} \sqrt{\frac{2\pi}{k\rho}} e^{-jk\rho} e^{\frac{j\pi}{4}} \frac{\sin(\frac{\phi_o}{n})}{\Psi(\frac{n\pi}{2} - \phi_o)} * \left\{ \frac{\Psi(\pi + \frac{n\pi}{2} - \phi)}{\cos(\frac{\pi - \phi}{n}) - \cos(\frac{\phi_o}{n})} - \frac{\Psi(-\pi + \frac{n\pi}{2} - \phi)}{\cos(\frac{\pi + \phi}{n}) - \cos(\frac{\phi_o}{n})} \right\} \quad (3.38)$$

In this evaluation, the normalized equivalent surface impedance is assumed to be constant for all incident angles. Eq (3.38) will be used as the singularly diffracted field from an impedance double wedge at the phase reference. For other edges on a double wedge, Eq (3.38) can be used provided a phase term $\exp(-jkr)$ is included where r is the appropriate phase factor.

Impedance Double Wedge

The geometry of an impedance double wedge is shown in figure 3.8. The single diffractions at Q_1 and Q_2 and the double diffractions and triple diffractions on the common wedge will be presented. Throughout the analysis Q_1 is taken as the phase reference, and all local angles are measured with respect to the common, "o", wedge face. The normalized equivalent surface impedances of the 3 wedge sections will be denoted η_0 , η_1 , and η_2 for the common wedge face, outer wedge face at Q_1 , and the outer wedge face at Q_3 , respectively.

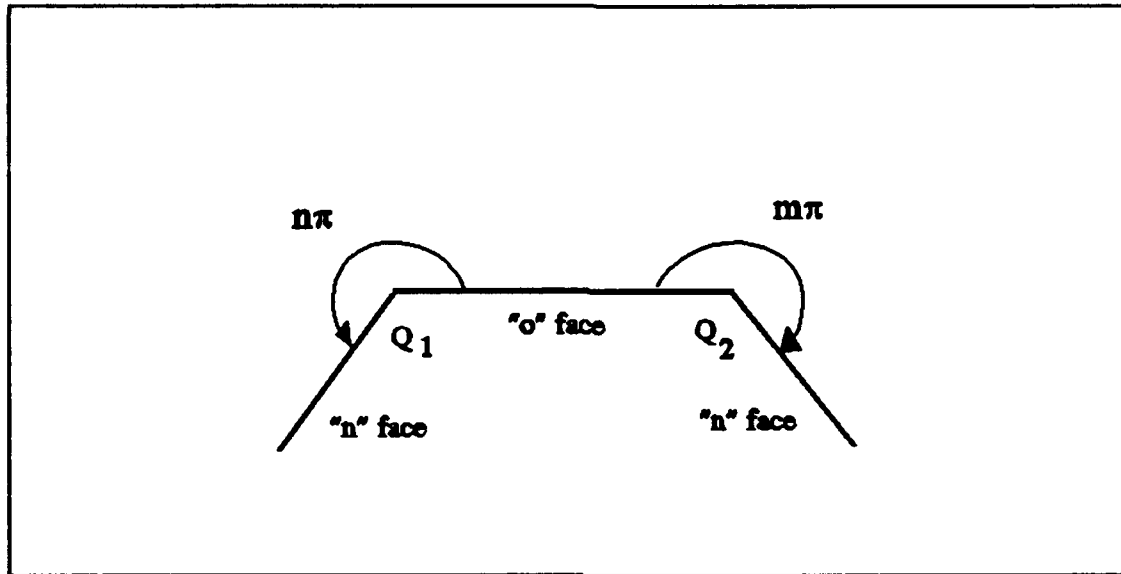


Figure 3.8. Geometry for an impedance double wedge.

Single Diffractions. The primary diffractions at Q_1 and Q_2 are given in Eq (3.38) where the appropriate phase factor for Q_1 is zero and for Q_2 is $-w(\cos \phi + \cos \phi_0)$.

Double Diffractions. The geometry for the double diffraction from Q_1 to Q_2 is shown in figure 3.9. The ESRM will be used to derive the double diffraction as in the derivation of the double diffractions for the resistive strips. Upon applying the ESRM, the integral for the double diffraction from Q_1 to Q_2 is

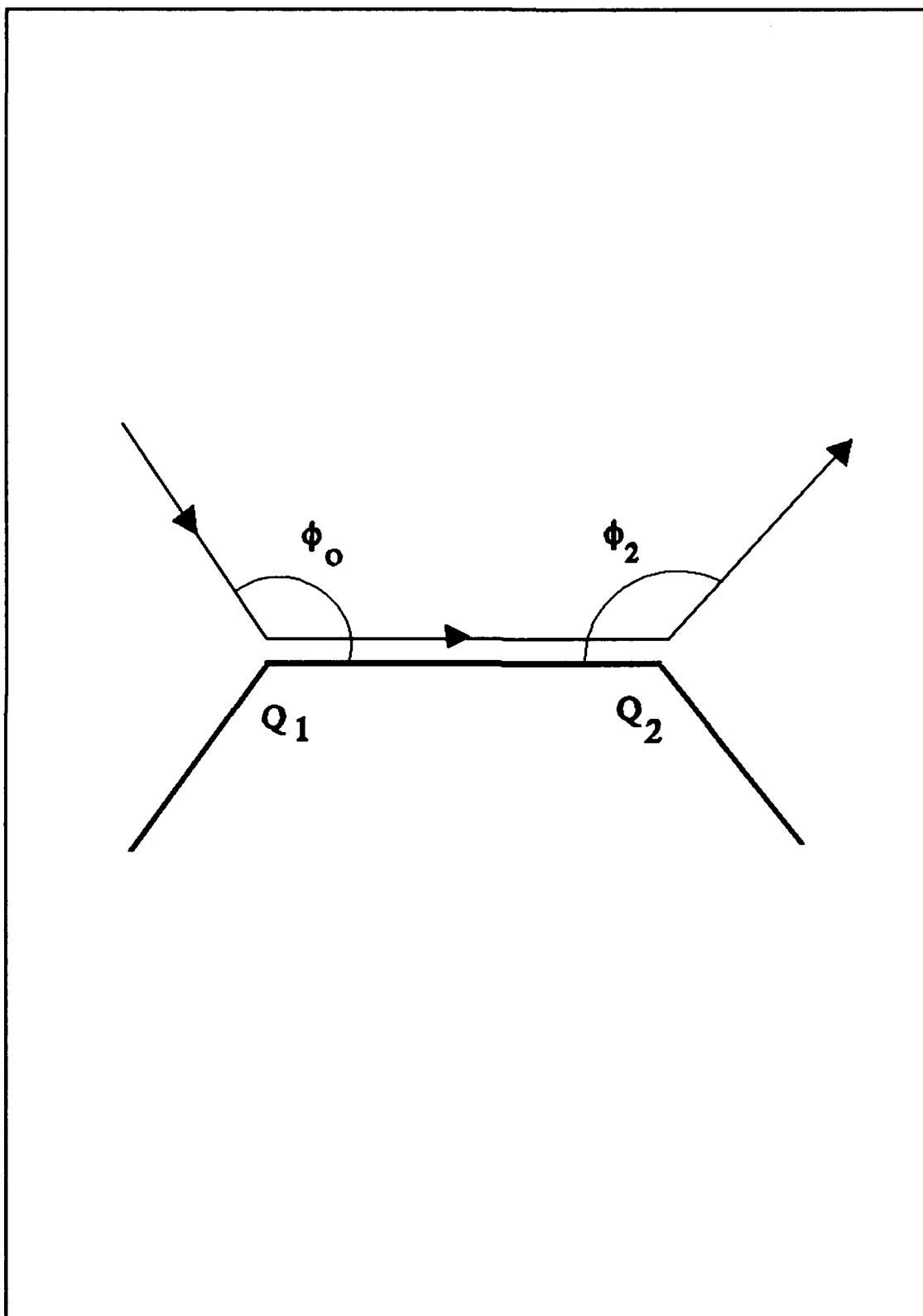


Figure 3.9. Double diffraction ray mechanism from Q_1 to Q_2 on an impedance double wedge.

$$\begin{aligned}
u_{21}^d(\phi_2, \phi_o) = & \frac{-1}{4\pi^2 mn} \sqrt{\frac{2\pi}{k\rho}} e^{-jk\rho} e^{j\frac{\pi}{4}} \frac{1}{\Psi(\frac{n\pi}{2} - \phi_o) \Psi(\frac{m\pi}{2} - \phi_2)} \\
& * \int_{S(0)} e^{-jkw \cos \alpha} \sin(\frac{\alpha}{n}) \sin(\frac{\alpha}{m}) \Psi(\alpha + \frac{n\pi}{2} + \pi) \Psi(-\alpha + \frac{m\pi}{2} + \pi) \\
& * \left\{ \frac{1}{\cos(\frac{\pi + \phi_o}{n}) - \cos(\frac{\alpha}{n})} - \frac{1}{\cos(\frac{\pi - \phi_o}{n}) - \cos(\frac{\alpha}{n})} - \frac{\sin(\frac{\phi_o}{n}) C_{on}(\alpha)}{\cos(\frac{\pi - \alpha}{n}) - \cos(\frac{\phi_o}{n})} \right\} \\
& \left\{ \frac{1}{\cos(\frac{\pi - \phi_2}{m}) - \cos(\frac{\alpha}{m})} - \frac{1}{\cos(\frac{\pi + \phi_2}{m}) - \cos(\frac{\alpha}{m})} \right. \\
& \left. + \frac{\sin(\frac{\phi_2}{m}) C_{om}(-\alpha)}{\cos(\frac{\pi + \alpha}{m}) - \cos(\frac{\phi_2}{m})} \right\}
\end{aligned} \quad (3.39)$$

where

$$C_{o,l}(\alpha) = \frac{0.25 \sin(\zeta^+) - \sin(\zeta^-) - 2 \sin(\frac{\pi}{l}) \cos(\frac{\alpha}{l}) + \sin(\iota^+) + \sin(-\iota^-)}{\sin(\frac{\alpha + \pi - \theta^+}{2l}) \sin(\frac{\alpha + \theta^+}{2l}) \cos(\frac{\alpha + \pi - \theta^-}{2l}) \cos(\frac{\alpha + \theta^-}{2l})} \quad (3.40)$$

and

$$\zeta^\pm = \frac{\theta^\pm}{l} \quad (3.41)$$

$$\iota^\pm = \frac{\pi - \theta^\pm}{l} \quad (3.42)$$

and l is the appropriate wedge angle integer, n or m . Eq (3.39) can be integrated uniformly to find the doubly diffracted field from Q_1 to Q_2 . Upon integration using the modified Pauli-Clemmow approach, the diffracted field becomes

$$\begin{aligned}
 u_{21}^d(\phi_2, \phi_o) = & -\frac{j}{\pi k(mn)^2} \frac{e^{-jk_w} e^{-jk_p}}{\sqrt{w} \sqrt{\rho}} \frac{\Psi(\frac{n\pi}{2} + \pi) \Psi(\frac{m\pi}{2} + \pi)}{\Psi(\frac{n\pi}{2} - \phi_o) \Psi(\frac{m\pi}{2} - \phi_2)} \\
 & * a_1 a_2 a_3 [A \{1 - F_{KP}(kwa_1)\} + B \{1 - F_{KP}(kwa_2)\} + C \{1 - F_{KP}(kwa_3)\}] \\
 & * \left\{ \frac{1}{1 - \cos(\frac{\pi - \phi_o}{n})} - \frac{1}{1 - \cos(\pi + \frac{\phi_o}{n})} - \frac{\sin(\frac{\phi_o}{n}) C_{om}(0)}{\cos(\frac{\pi}{n}) - \cos(\frac{\phi_o}{n})} \right\} \\
 & * \left\{ \frac{1}{1 - \cos(\frac{\pi + \phi_2}{m})} - \frac{1}{1 - \cos(\frac{\pi - \phi_2}{m})} - \frac{\sin(\frac{\phi_2}{m}) C_{om}(0)}{\cos(\frac{\pi}{m}) \cos(\frac{\phi_2}{m})} \right\} \frac{e^{-jk_r}}{2}
 \end{aligned} \tag{3.43}$$

where

$$a_1 = 2 \cos^2\left(\frac{\phi_o}{2}\right) \tag{3.44}$$

$$a_2 = 2 \cos^2\left(\frac{\phi_2}{2}\right) \tag{3.45}$$

$$a_3 = 2 \sin^2\left(\frac{\theta}{2}\right) \quad (\theta \text{ of common face}) \tag{3.46}$$

$$A = -\frac{1}{(a_2 - a_1)(a_3 - a_1)} \tag{3.47}$$

$$B = -\frac{1}{(a_1 - a_2)(a_3 - a_2)} \quad (3.48)$$

$$C = -\frac{1}{(a_1 - a_3)(a_2 - a_3)} \quad (3.49)$$

and $r = -w \cos(\phi)$. A factor of one half was included to account for grazing on the common wedge face. Also, the integration accounts for the presence of the geometrical optics poles and the surface wave poles.

The above equations can be used for the reciprocal double diffraction from Q_2 to Q_1 by substituting $r \rightarrow -w \cos(\phi_o)$, $\phi_o \rightarrow \pi - \phi_o$, $\phi_2 \rightarrow \pi - \phi_2$, $m \rightarrow n$, and $n \rightarrow m$ in Eq (3.43).

Triple Diffractions. The geometry for the triple diffraction at Q_1 is shown in figure 3.10. Once again using the ESRM, the integral representation for the triple diffracted field from Q_1 to Q_2 and back to Q_1 is

$$u_{121}^d(\phi, \phi_o) = \frac{j}{2\pi n} \int_{S(O)} e^{-jkwc \cos \alpha} \sin\left(\frac{\alpha}{n}\right) u_{21}^d(\alpha, \phi_o) \frac{\Psi\left(\alpha + \frac{n\pi}{2} + \pi\right)}{\Psi\left(\frac{n\pi}{2} - \phi\right)} \quad (3.50)$$

$$* \left\{ \frac{1}{\cos\left(\frac{\pi + \phi}{n}\right) - \cos\left(\frac{\alpha}{n}\right)} - \frac{1}{\cos\left(\frac{\pi - \phi}{n}\right) - \cos\left(\frac{\alpha}{n}\right)} - \frac{\sin\left(\frac{\phi}{n}\right) C_{on}(\alpha)}{\cos\left(\frac{\pi - \alpha}{n}\right) - \cos\left(\frac{\phi}{n}\right)} \right\}$$

where $u_{21}^d(\alpha, \phi_o)$ is the double diffracted field from Q_1 to Q_2 .

After the integration of Eq (3.50) using the modified Pauli-Clemmow

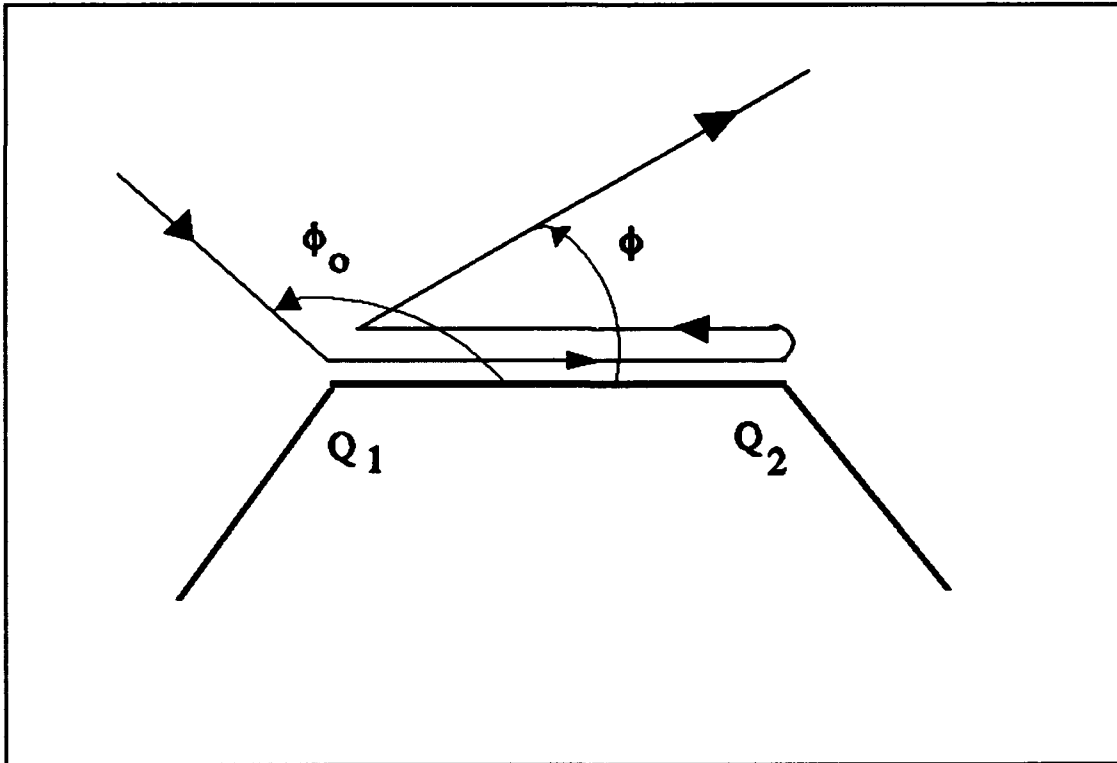


Figure 3.10. Triple diffraction ray mechanism on an impedance double wedge at Q_1 .

method of steepest descents, while accounting for the geometrical optics and surface wave poles, the triple diffracted field is then

$$\begin{aligned}
u_{121}^d(\phi, \phi_o) = & \frac{j2\sqrt{2}e^{-jk_w}e^{j\frac{3\pi}{4}}}{(k\pi)^{\frac{2}{3}}w(nm)^3n} \frac{e^{-jk\rho}}{\sqrt{\rho}} \frac{\Psi^2(\frac{n\pi}{2} + \pi) \Psi(\frac{m\pi}{2} + \pi)}{\Psi(\frac{n\pi}{2} - \phi_o) \Psi(\frac{n\pi}{2} - \phi) \Psi(\frac{m\pi}{2})} \\
& * \left\{ \frac{a_1 a_3^2 a_4}{(a_3 - a_4)} [A\{1 - F_{KP}(kwa_1)\} + B\{1 - F_{KP}(kwa_2)\} + C\{1 - F_{KP}(kwa_3)\}] \right. \\
& \quad * [F_{KP}(kwa_3) - F_{KP}(kwa_4)] \frac{e^{-jk_r}}{4} \\
& \quad * \left\{ \frac{1}{1 - \cos(\frac{\pi - \phi_o}{n})} - \frac{1}{1 - \cos(\frac{\pi + \phi_o}{n})} - \frac{\sin(\frac{\phi_o}{n}) C_{om}(0)}{\cos(\frac{\pi}{n}) - \cos(\frac{\phi_o}{n})} \right\} \\
& \quad * \left\{ \frac{1}{1 - \cos(\frac{\pi - \phi}{n})} - \frac{1}{1 - \cos(\frac{\phi + \phi}{n})} - \frac{\sin(\frac{\phi}{n}) C_{om}(0)}{\cos(\frac{\pi}{n}) - \cos(\frac{\phi}{n})} \right\} \\
& \quad * \left\{ \frac{-2\sin(\frac{\pi}{m})}{[1 - \cos(\frac{\pi}{m})]^2} - \frac{C_{om}(0)}{1 - \cos(\frac{\pi}{m})} \right\} \quad (3.51)
\end{aligned}$$

where

$$a_4 = 2\cos^2\left(\frac{\phi}{2}\right) \quad (3.52)$$

and a one fourth factor was included to account for grazing on the common wedge face. Also, the phase factor is zero.

If the triple diffraction starting at Q_2 going to Q_1 and back to Q_2 is desired, Eq (3.51) is still correct providing the transformations $\phi_o \rightarrow \pi - \phi_o$, $\phi \rightarrow \pi - \phi$, $m \rightarrow n$, and $n \rightarrow m$ are used. Now, the phase factor would be $r = -w(\cos\phi + \cos\phi_o)$.

Convex Cylindrical Polygon

The combination of many impedance double wedges can be used to construct a convex impedance cylindrical polygon. A section of this polygon is illustrated in figure 3.11. If all the parameters are applied to the local geometry of each double wedge in the polygon, the previously presented diffraction fields for single, double, and triple diffractions can be used. For the polygon, one can envision an additional diffraction as shown in figure 3.11.

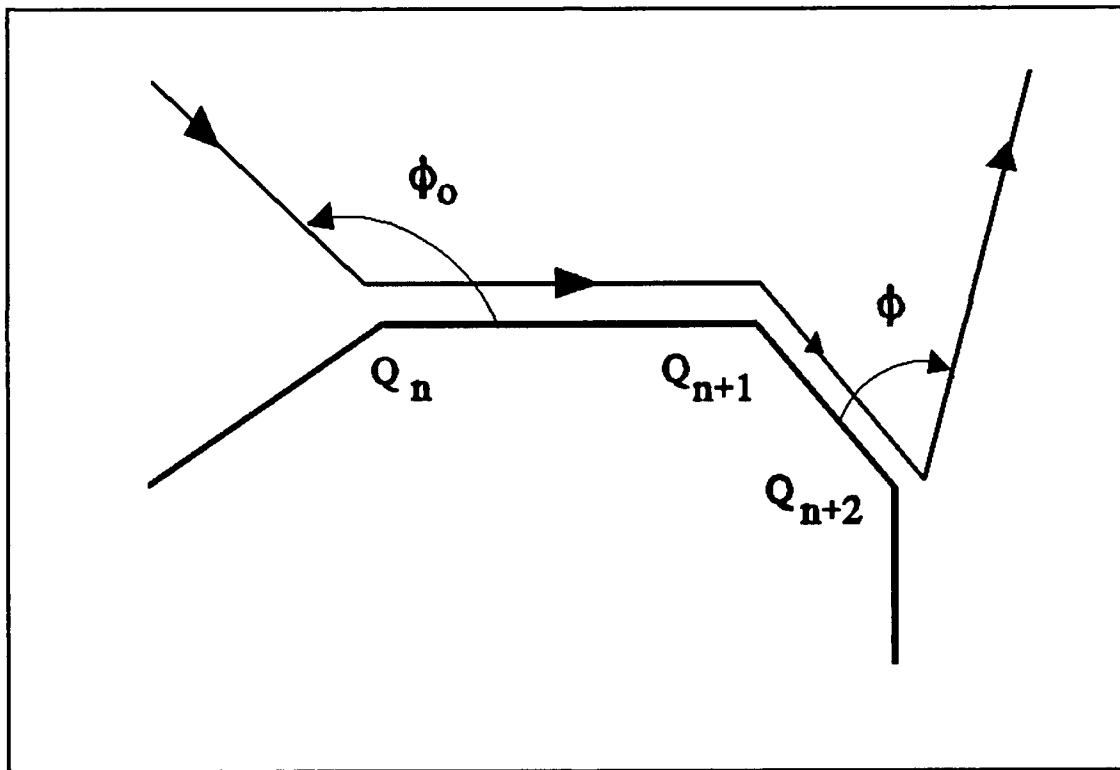


Figure 3.11. Three vertex triple diffraction ray mechanism on an impedance polygon.

Herman (5) has derived such a diffraction. The three vertex triple diffraction is described by an incident wave on Q_n generating spectral waves diffracting at an angle $-\alpha$ and propagating toward Q_{n+1} . This ray incident at Q_{n+1} then diffracts at

a local angle α . The diffracted field is the double diffraction field already derived. The diffracted ray then can travel to Q_{n+2} and diffract toward the observer. The diffraction will be called a three vertex triple diffraction.

The diffracted field has the integral representation

$$u_{121}^d(\phi, \phi_o) = \frac{j}{2\pi p} \int_{s(o)} e^{-jk w_2 \cos \alpha} \sin \frac{\alpha}{p} u_{21}^d(2\Phi - \alpha, \phi_o) \frac{\Psi(\alpha + \frac{p\pi}{2} + \pi)}{\Psi(\frac{p\pi}{2} - \phi)} \quad (3.53)$$

$$* \left\{ \frac{1}{\cos(\frac{\pi + \phi}{p}) - \cos(\frac{\alpha}{p})} - \frac{1}{\cos(\frac{\pi - \phi}{p}) - \cos(\frac{\alpha}{p})} - \frac{\sin(\frac{\phi}{p}) C_{op}(\alpha)}{\cos(\frac{\pi - \alpha}{p}) - \cos(\frac{\phi}{p})} \right\}$$

where $p\pi$ is the external wedge angle at Q_{n+2} and $n\pi$ and $m\pi$ are the external wedge angles at vertices Q_n and Q_{n+1} , respectively. Also, $u_{21}^d(\alpha, \phi_o)$ is the double diffraction field in Eq (3.43).

Eq (3.53) can be integrated uniformly using the modified Pauli-Clemmow method of steepest descent while accounting for the presence of the surface wave and geometrical optics poles. The result is

$$\begin{aligned}
u_{121}^d(\phi, \phi_o) = & \frac{j\sqrt{2}e^{-jk(w_1+w_2)}e^{j\frac{3\pi}{4}}}{(k\pi)^{\frac{3}{2}}\sqrt{w_1w_2}(nm)^2p^2m}\frac{e^{-jk\rho}}{\sqrt{\rho}}\frac{\Psi(\frac{n\pi}{2}+\pi)\Psi(\frac{m\pi}{2}+\pi)\Psi(\frac{p\pi}{2}+\pi)}{\Psi(\frac{n\pi}{2}-\phi_o)\Psi(\frac{p\pi}{2}-\phi)\Psi(-\frac{m\pi}{2})} \\
& \frac{a_1a_2a_3a_4a_5}{a_5-a_4}[A\{1-F_{KP}(kw_1a_1)\}+B\{1-F_{KP}(kw_1a_2)\}+C\{1-F_{KP}(kw_1a_3)\}] \\
& * [F_{KP}(kw_2a_3)-F_{KP}(kw_2a_4)]\frac{e^{-jk\rho}}{4} \\
& * \left\{ \frac{1}{1-\cos(\frac{\pi-\phi_o}{n})} - \frac{1}{1-\cos(\frac{\pi+\phi_o}{n})} - \frac{\sin(\frac{\phi_o}{n})C_{on}(0)}{\cos(\frac{\pi}{n})-\cos(\frac{\phi_o}{n})} \right\} \\
& * \left\{ \frac{1}{1-\cos(\frac{\pi-\phi_o}{n})} - \frac{1}{1-\cos(\frac{\pi+\phi}{p})} - \frac{\sin(\frac{\phi}{p})C_{on}(0)}{\cos(\frac{\pi}{p})-\cos(\frac{\phi_o}{p})} \right\} \\
& * \left\{ \frac{-2\sin(\frac{\pi}{m})}{[1-\cos(\frac{\pi+m\pi}{m})][1-\cos(\frac{\pi-m\pi}{m})]} + \frac{C_{on}(0)}{1+\cos(\frac{\pi}{m})} \right\}
\end{aligned} \tag{3.54}$$

where

$$a_5 = 2\sin^2\left(\frac{\theta_{n+1}}{2}\right) \tag{3.55}$$

and θ_{n+1} is associated with the common wedge between Q_{n+1} and Q_{n+2} . The phase factor is $r = -w'_2 \cos(\phi) - w'_1 \cos(\phi_o)$ where ϕ , ϕ_o , w'_1 , and w'_2 are shown in figure 3.12.

Flat Impedance Structure

The convex impedance polygon can be made into a flat impedance

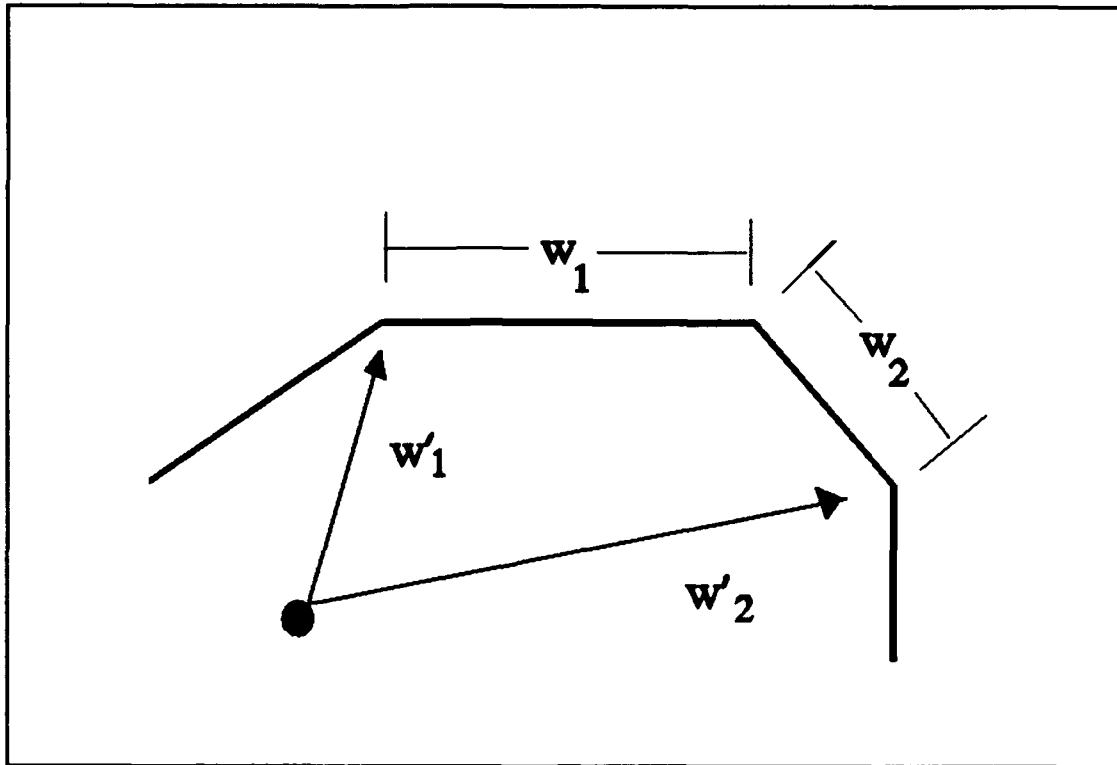


Figure 3.12. Geometry for the three vertex triple diffraction ray mechanism on an impedance polygon.

structure by collapsing the interior angles to zero. This situation is an example of a loaded strip or a tapered strip, i. e., flat impedance strips junctioned together. The objective of this thesis is to analyze perfectly conducting strips with constant loads. Therefore, the diffracted field derived by Herman (4) for convex impedance polygons is applicable.

The single diffracted field, Eq (3.38), double diffracted field, Eq (3.43), and triple diffracted field, Eq (3.51) for the impedance double wedge are applicable to a strip if the local geometry of the structure is considered. The three vertex triple diffracted field, Eq (3.54), is applicable, but the derivation assumed the structure was convex, i.e, the external wedge angle integers (n , m , and p) were not equal to

1. Inspecting Eq (3.54), one can see the following terms become unbounded when $m = 1$

$$\frac{-2\sin(\frac{\pi}{m})}{[1 - \cos(\frac{\pi + m\pi}{m})][1 - \cos(\frac{\pi - m\pi}{m})]} + \frac{C_{om}(0)}{1 + \cos(\frac{\pi}{m})} \quad (3.56)$$

This occurs when the middle vertex of a three vertex triple diffraction has an external wedge angle of π .

Since the flat structure is a special case of a polygon, this diffracted field is applicable as the wedge approaches a flat junction. The diffracted field can be used if the unbounded behavior is eliminated. This is done by taking a small argument approximation and a limit on the cosine and sine terms in Eq (3.56). Doing so changes Eq (3.56) to

$$\frac{-\frac{\pi}{m}}{2 - (\frac{\pi}{m})^2} + \frac{C_{om}(o)}{2 - \frac{1}{2}(\frac{\pi}{m})^2} \quad (3.57)$$

Therefore, the three vertex triple diffracted field derived for the convex polygon can be used directly for a flat structure if Eq (3.57) is substituted for Eq (3.56) in Eq (3.54).

IV. Scattering Predictions

This chapter contains the scattering predictions for impedance strips and impedance-loaded strips. First, the diffraction sources on impedance strips and impedance-loaded strips are discussed. Second, a discussion of the diffraction sources included in the developed computer program is presented. Third, scattering predictions for impedance strips and impedance-loaded strips with several impedances are presented and compared to a perfectly conducting strip of equal length.

Diffraction Sources

The diffracted fields developed in Chapter 3 are now applied to impedance strips and impedance-loaded strips.

Strips. The diffracted fields for the impedance strip developed in Chapter 3 can be applied to constant impedance strips with different impedances on the top and bottom of the strip. There are two primary diffraction sources on a strip and they are simply the two edges (external wedge angles of 2π) on the strip. There are many possible secondary diffractions that occur on a strip. For example, there are double diffractions which arise after a single diffraction at an edge travels down the strip to the other edge and diffracts toward the observer. This diffraction occurs at both edges, and travels on the top and the bottom of the strip. Other diffraction mechanisms which are possible on a strip are the triple, fourth, fifth, and so on. In short, the diffraction order refers to the number of

diffractions that occur on the strip before the energy scatters back to the observer. Also, each of these possible diffractions occurs on the top and bottom of the strip. The number of secondary diffraction mechanisms required to accurately model a strip will depend on the length of the strip. As a secondary diffraction propagates down the length of a strip, it attenuates. Obviously, an n^{th} diffraction mechanism will have $n-1$ attenuation paths. The length of a strip is an important factor in determining the number of secondary diffractions required. More secondary diffractions must be considered on a strip as the strip becomes shorter.

In this thesis, only the single, double, and triple diffractions are considered. There are twelve diffractions considered in the analysis of the constant impedance strip. There are two single diffractions: one at each edge. There are four double diffractions. One set of two occurs on the top of the strip while the second set of two exist on the bottom of the strip. Also, each set of two are of equal strength. Finally, there are eight triple diffractions on the strip. A set of four triple diffractions exist with two on the top of the strip and two on the bottom of the strip. Another set of four triple diffractions exist where two begin on the bottom of the strip and two begin on the top of the strip. Likewise, the two sets of triple diffractions on the strip are of equal strength.

Loaded Strips. A loaded impedance strip is basically a series of constant impedance strips junctioned together. In this thesis, loaded impedance strips are considered to be perfectly conducting strips with impedance loads attached on each edge of the conductor. Therefore, each loaded strip will have two edges (external wedge angles of 2π) and multiple junctions (external wedge angles of π).

In this configuration, the perfectly conducting strip can have constant impedance loads or tapered loads. The tapered loads on the strip can be modelled as a series of different impedance loads of different lengths and impedance values to simulate the required taper.

The diffracted fields developed from the double wedge formulation in Chapter 3 will be used for the analysis of impedance-loaded conducting strips. The primary diffractions on a loaded strip occur at the edges and junctions on the loaded strip. The secondary diffractions on the loaded strip are numerous. All of the secondary diffractions mentioned for a strip will be present plus many other secondary diffractions which bypass junctions and diffract on other junctions or edges. These diffractions will be called by-junctional diffractions, since they bypass junctions before diffracting back to the observer. Other secondary diffractions are ones which diffract at a number of vertices before diffracting back to the observer. These diffractions are called n-vertex secondary diffractions. An example of a three-vertex secondary diffraction is shown in figure (3.11).

The formulation of the impedance double wedge assumes there are only multiple diffractions on the top of the structure. For a loaded strip with two or more junctions, there may be a triple diffraction on the bottom of an edge, but it is neglected in this thesis. Also, there could be by-junctional diffractions, but their presence and strength would depend on the number of impedance strip sections on the loaded strip. The by-junctional diffractions will not be considered since they are not derivable in the context of the double wedge formulation. Therefore, in this thesis, the primary diffractions at edges and junctions will be considered,

the double and triple secondary diffractions on a section of a strip will be considered, and a three-vertex secondary diffraction will be considered. The last secondary diffraction mechanism is considered because it is expected that non-adjacent strips will have diffraction mechanisms between them. Herman (5) originally developed the diffraction mechanisms for an impedance polygon. The three-vertex secondary diffraction mechanism is a dominant diffraction on a polygon (5).

Application of the Double Wedge Diffraction Mechanisms.

Herman (4) has used the presented diffraction mechanisms in Chapter 3 to predict the scattering from impedance strips and impedance polygons. His work showed the diffraction mechanisms agreed extremely well with method of moment predictions. Method of moments codes were not available for comparison in this thesis. Therefore, the accuracy of the predictions can only be compared against measurements.

A computer code for the analysis of multiply loaded impedance strips was written in Fortran that takes into account all of the diffraction mechanisms presented in Chapter 3 for an impedance double wedge and the three-vertex secondary diffraction considered for impedance polygons. This code can be used to model constant impedance strips or strips with multiple loads. It should be noted that if the code is used for constant impedance strips, the multiple diffractions on the bottom of the strip are not considered.

Herman (5) wrote a computer code to predict the scattering from

impedance strips using the impedance half plane formulation in Chapter 3 and a code to predict the scattering from impedance polygons using the impedance wedge formulation in Chapter 3. The impedance strip program allows the impedance strip to have different impedances on the top and bottom of the strip. Because of the limitations of the double wedge formulation when applied to constant impedance strips, Herman's (5) code is used to predict the scattering from constant impedance strips.

Scattering Prediction Results

This section presents sample scattering predictions for impedance strips and impedance-loaded conducting strips.

Strips. Several impedances are now investigated to determine the amount of scattering an impedance strip exhibits compared to a perfectly conducting strip of the same length. The impedances investigated were $j3.0$, $-j3.0$, 1.2 , and 6.0 . These impedances were chosen such that a capacitive impedance, inductive impedance, low non-reactive impedance, and high non-reactive impedance are analyzed. Figures 4.1 through 4.4 show the predictions for 4λ impedance strips for the following impedance values and polarizations: $j3.0$ and $-j3.0$ for E-polarization, $j3.0$ and $-j3.0$ for H-polarization, 1.2 and 6.0 for E-polarization, and 1.2 and 6.0 for H-polarization, respectively. Referencing figures 4.1 and 4.2, the scattering level of the mainbeam for the impedances $j3.0$ and $-j3.0$ are the same for both polarizations. These mainbeam levels are also the same for the perfectly conducting strip. The differences in the patterns for the two impedances depend

significantly on polarization. For E-polarization, the inductive impedance would reduce the pattern for angles lower than 45 degrees and significantly reduce the pattern at 0 degrees (edge-on). On the other hand, the inductive impedance scattering prediction increases at 80 degrees and then violently oscillates with broad sidelobes of 0 dB or better. For H-polarization, the impedances have the opposite effect. Now, the capacitive impedance produces a more desirable pattern. The capacitive material produces a reduction in RCS at 65 degrees, but the edge-on RCS is significantly increased over the perfectly conducting strip at edge-on. The inductive material produces a larger RCS beginning at the second sidelobe and the edge-on RCS is even greater than the capacitive impedance. In summary, each of the impedances behave drastically different depending on polarization, which is an extremely undesirable characteristic when wanting to reduce the scattering for arbitrary incident polarization.

Figures 4.3 and 4.4 show the scattering predictions for large and small real impedances for both polarizations. The predictions show a reduction in RCS over the perfectly conducting strip for both impedances and both polarizations. However, the small impedance causes a drastic reduction in RCS. The large impedance value provides some reduction, but not a significant amount. One problem that occurs with both impedances for H-polarization is that the edge-on RCS is significantly increased.

Loaded Perfectly Conducting Strips. Figures 4.5 thru 4.8 are the scattering predictions for both E- and H-polarizations for a 2λ perfectly conducting strip with 1λ impedance loads of $j3.0$, $-j3.0$, 1.2 , and 6.0 attached on the edge of the 2λ

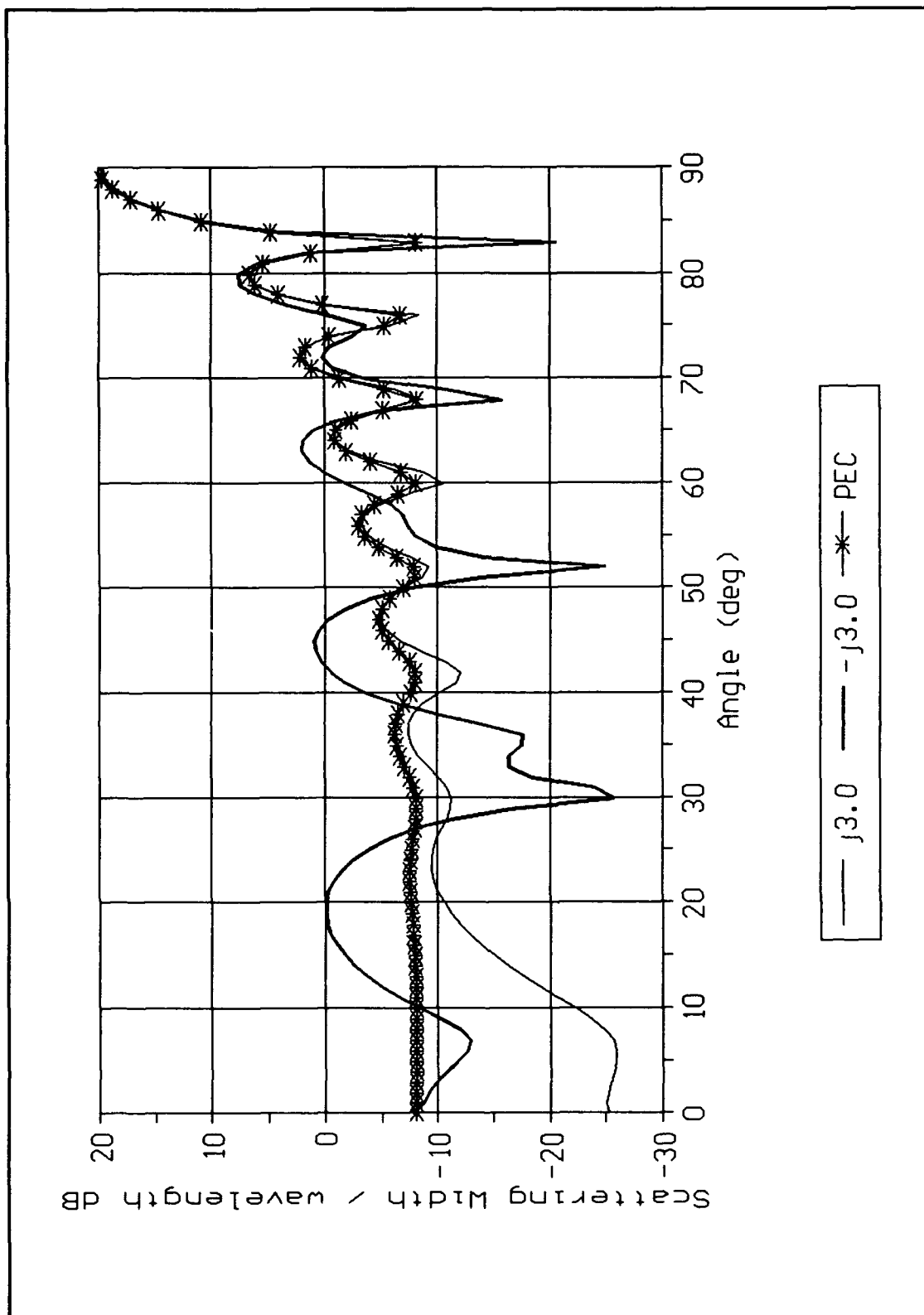


Figure 4.1. Scattering Predictions for 4λ impedance strips of impedances $j3.0$, $-j3.0$, and PEC, E-Polarization.

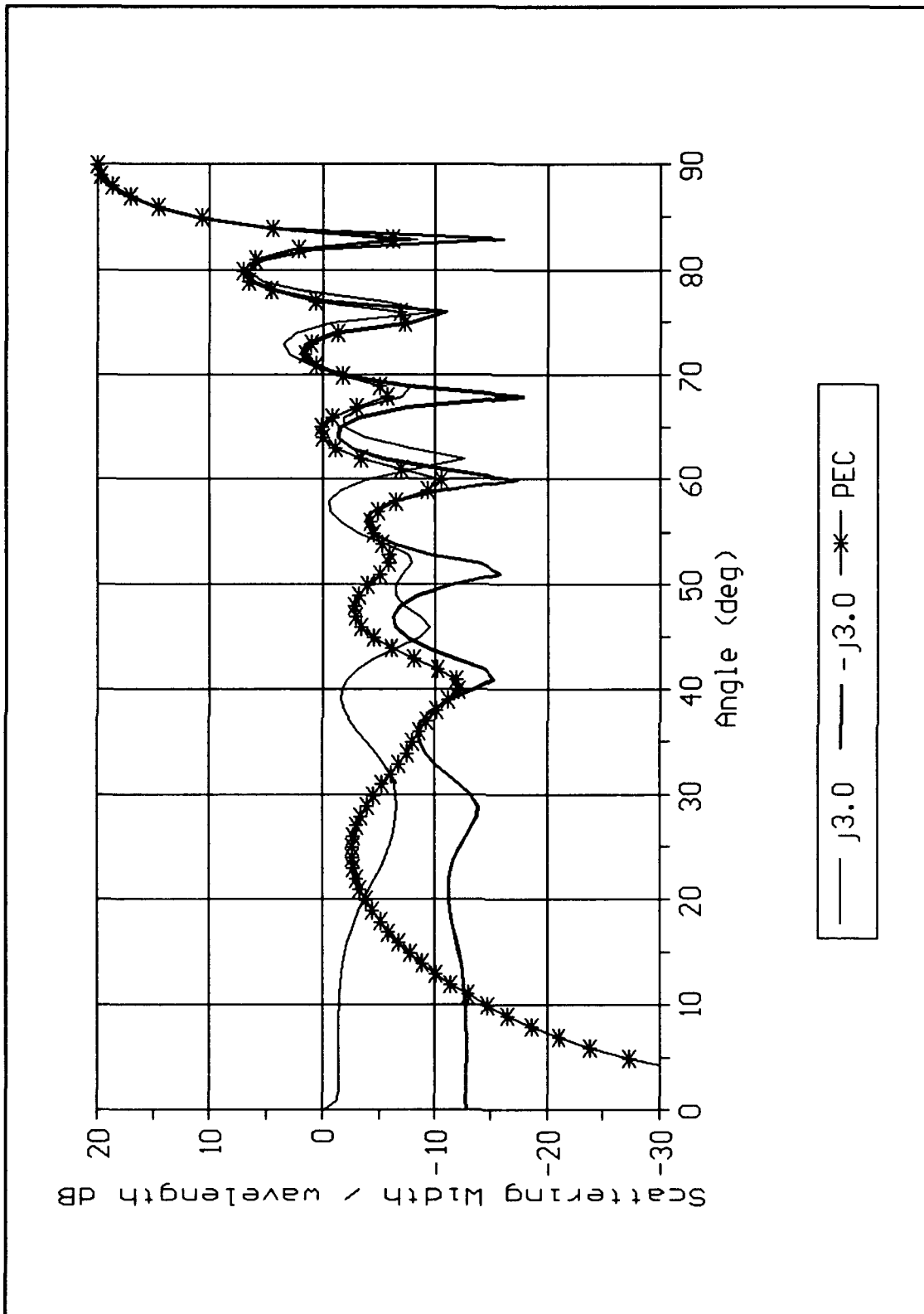


Figure 4.2. Scattering Predictions for 4λ impedance strips of impedances $j3.0$, $-j3.0$, and PEC, H-Polarization.

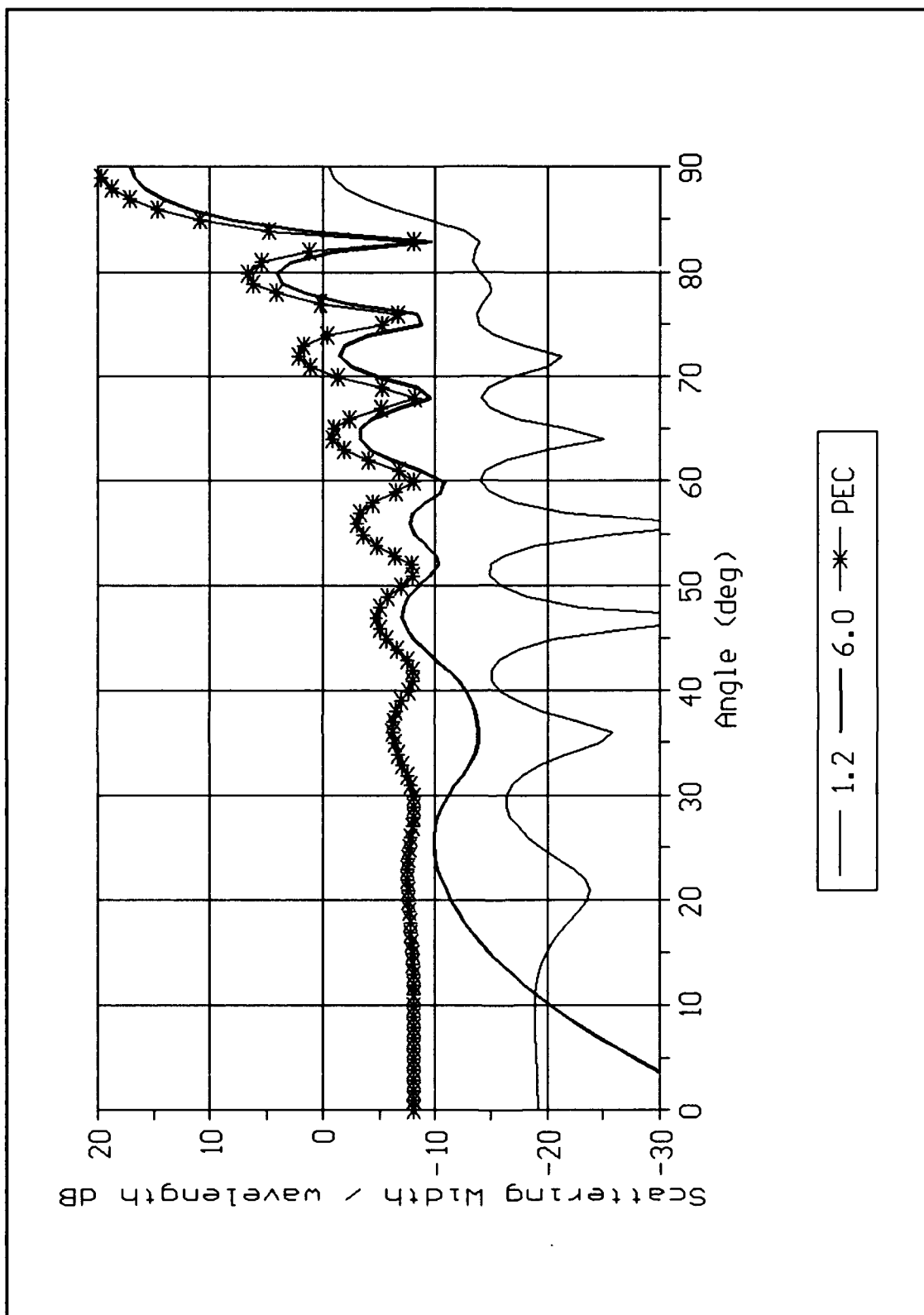


Figure 4.3. Scattering Predictions for 4λ impedance strips of impedances 1.2, 6.0, and PEC, E-Polarization.

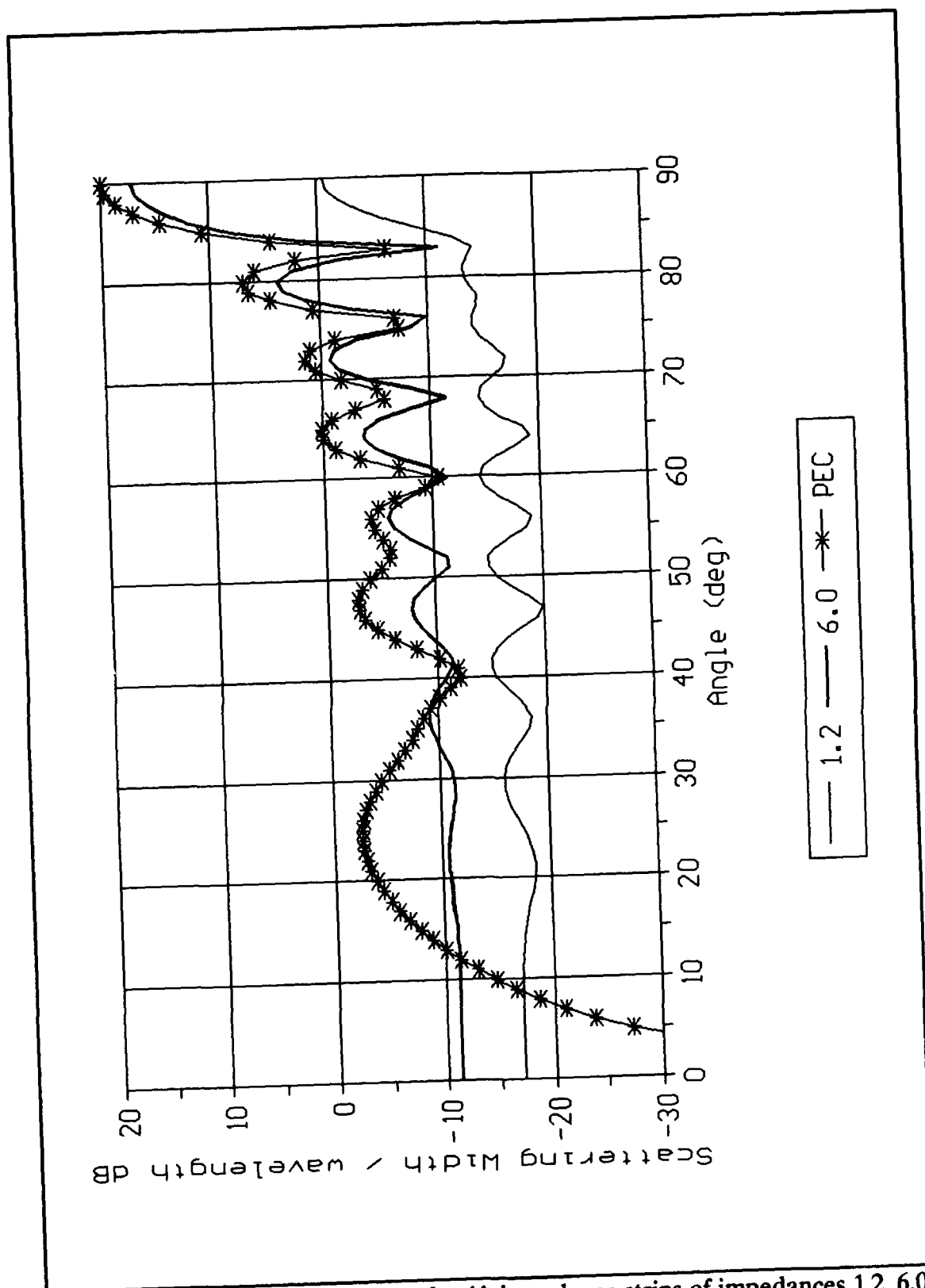


Figure 4.4. Scattering Predictions for 4λ impedance strips of impedances 1.2, 6.0, and PEC, H-Polarization.

strip.

For the capacitive and inductive loads, the RCS is greatly increased in the sidelobes over a 4λ perfectly conducting strip for both polarizations. A dominant scattering characteristic for both impedances and polarizations is the forming of a null at 90 degrees (broadside to the strip). However, higher sidelobe levels are produced and a mainbeam is formed at 81 degrees. An interesting trend in the predictions for E-polarization with capacitive and inductive impedances is the capacitive impedances scatters more than the inductive impedance for angles less than 55 degrees, but less for angles greater than 55 degrees. The reverse characteristic occurs for H-polarization.

The scattering of a 4λ perfectly conducting strip is not reduced by loading the edges with 1λ loads of either high or low purely real impedances. The higher impedance load produces a null at 90 degrees and higher sidelobes for both polarizations. The smaller impedance causes the mainbeam to lower by 7 dB, but widens by 10 degrees. For E-polarization, both impedances show a reduction in edge-on scattering. On the other hand, the scattering for both impedances is increased for H-polarization.

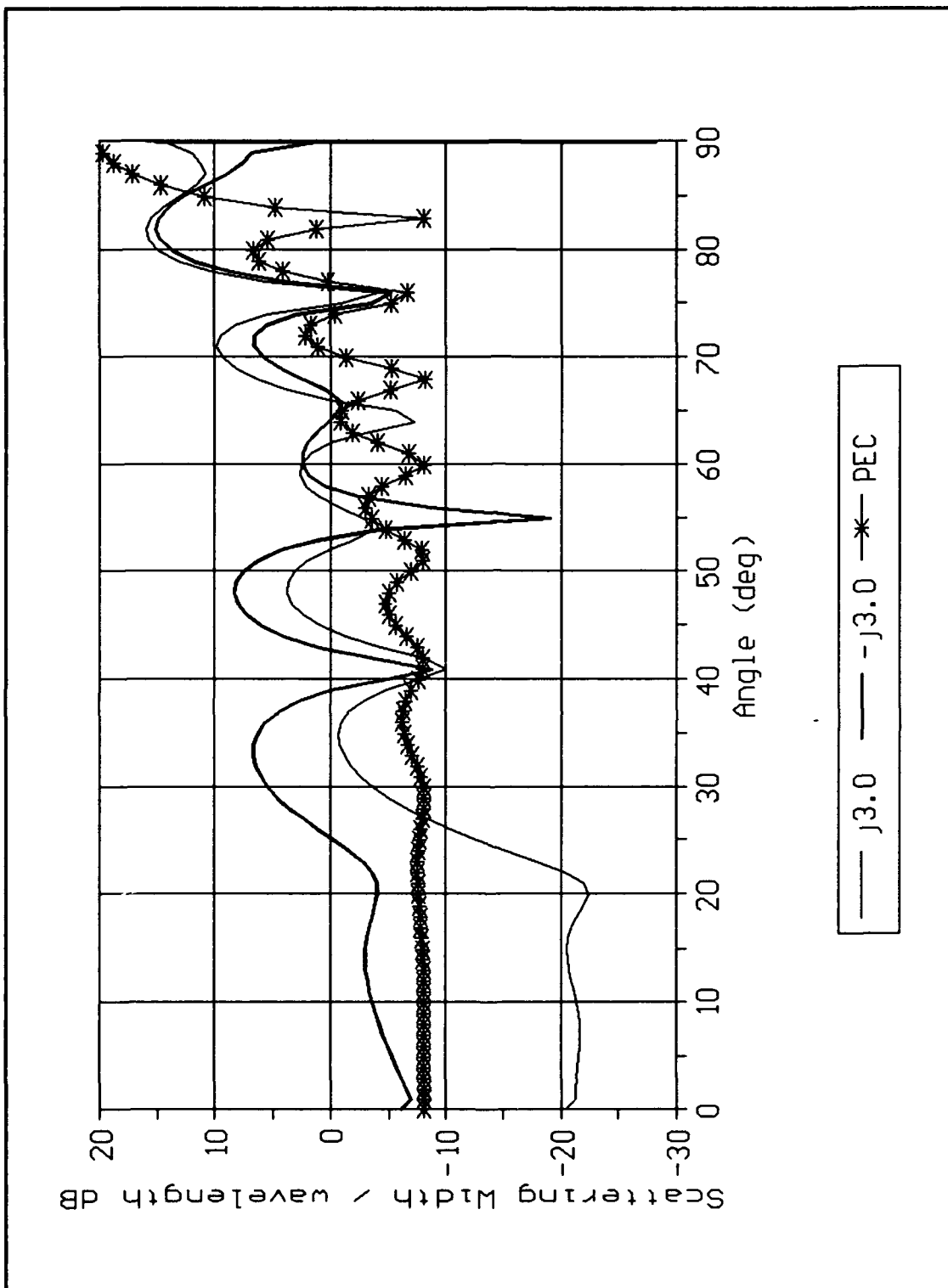


Figure 4.5. Scattering Predictions for a 4λ perfectly conducting strip and 2λ perfectly conducting strips with 1λ loads of impedances, $j3.0$ and $-j3.0$, E-Polarization.

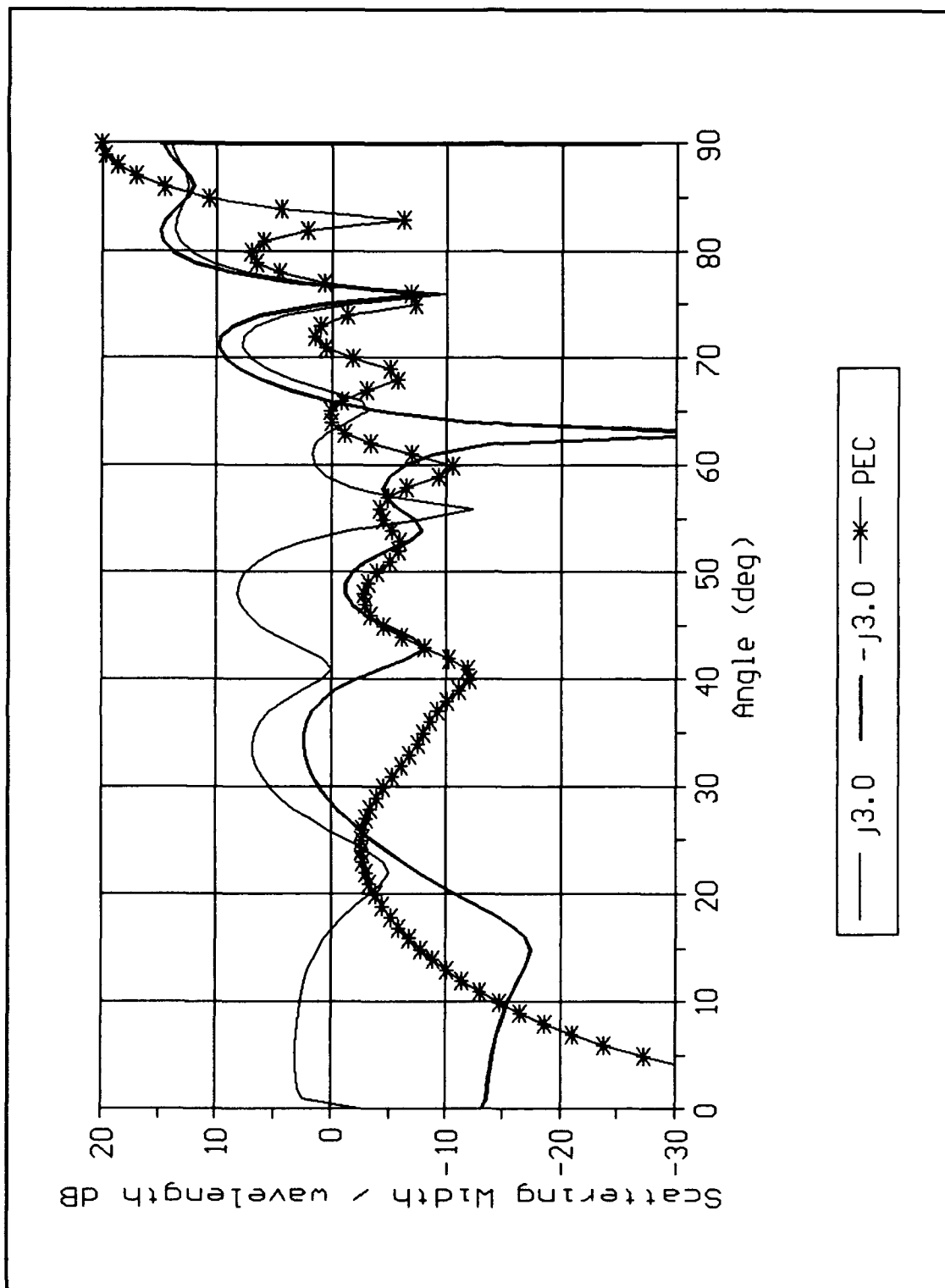


Figure 4.6. Scattering Prediction for a 4λ perfectly conducting strip and 2λ perfectly conducting strips with 1λ loads of impedances, $j3.0$ and $-j3.0$, H-Polarization.

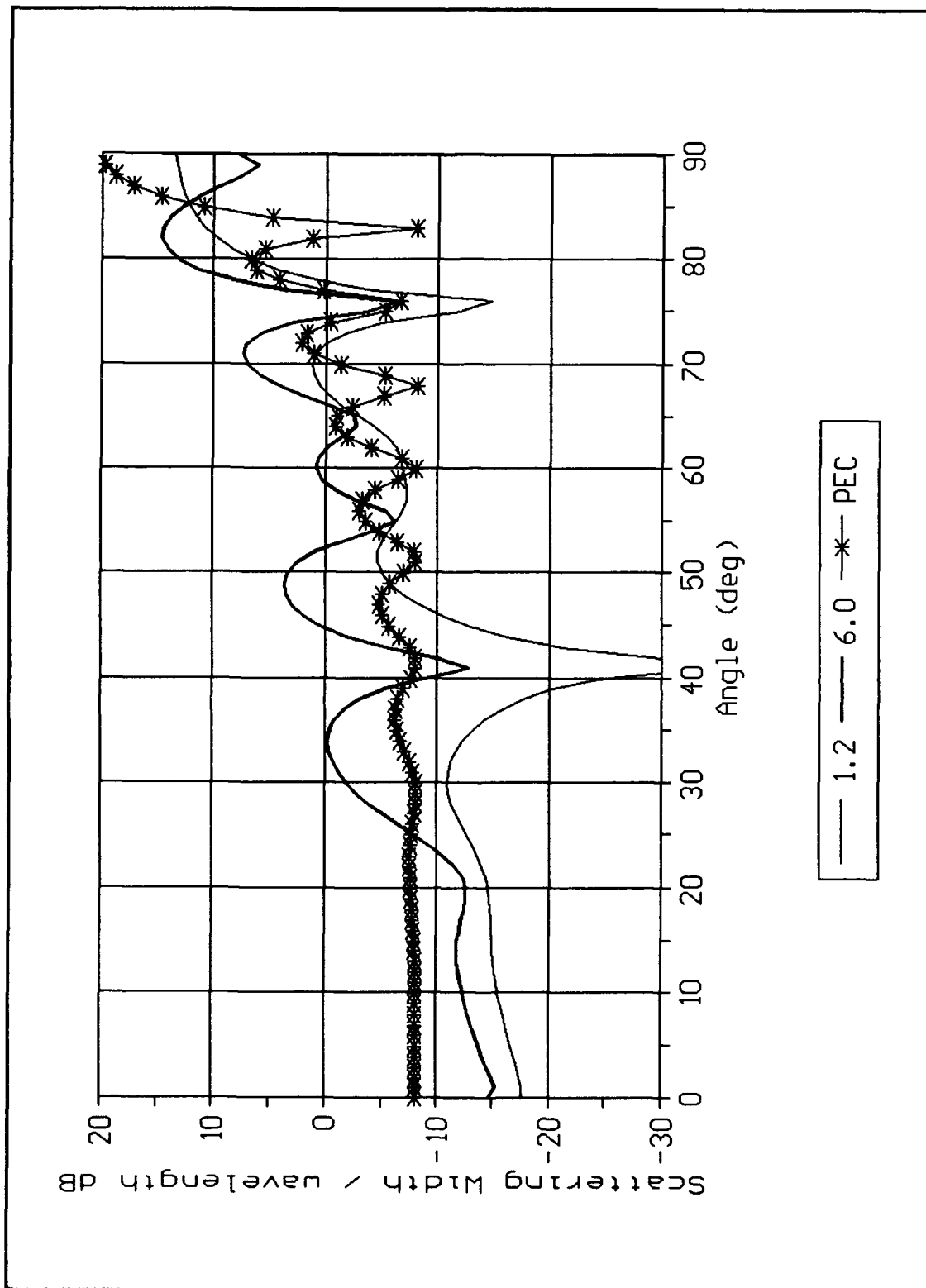


Figure 4.7. Scattering Prediction of a 4λ perfectly conducting strip and 2λ perfectly conducting strips with impedances, 1.2 and 6.0, E-Polarization.

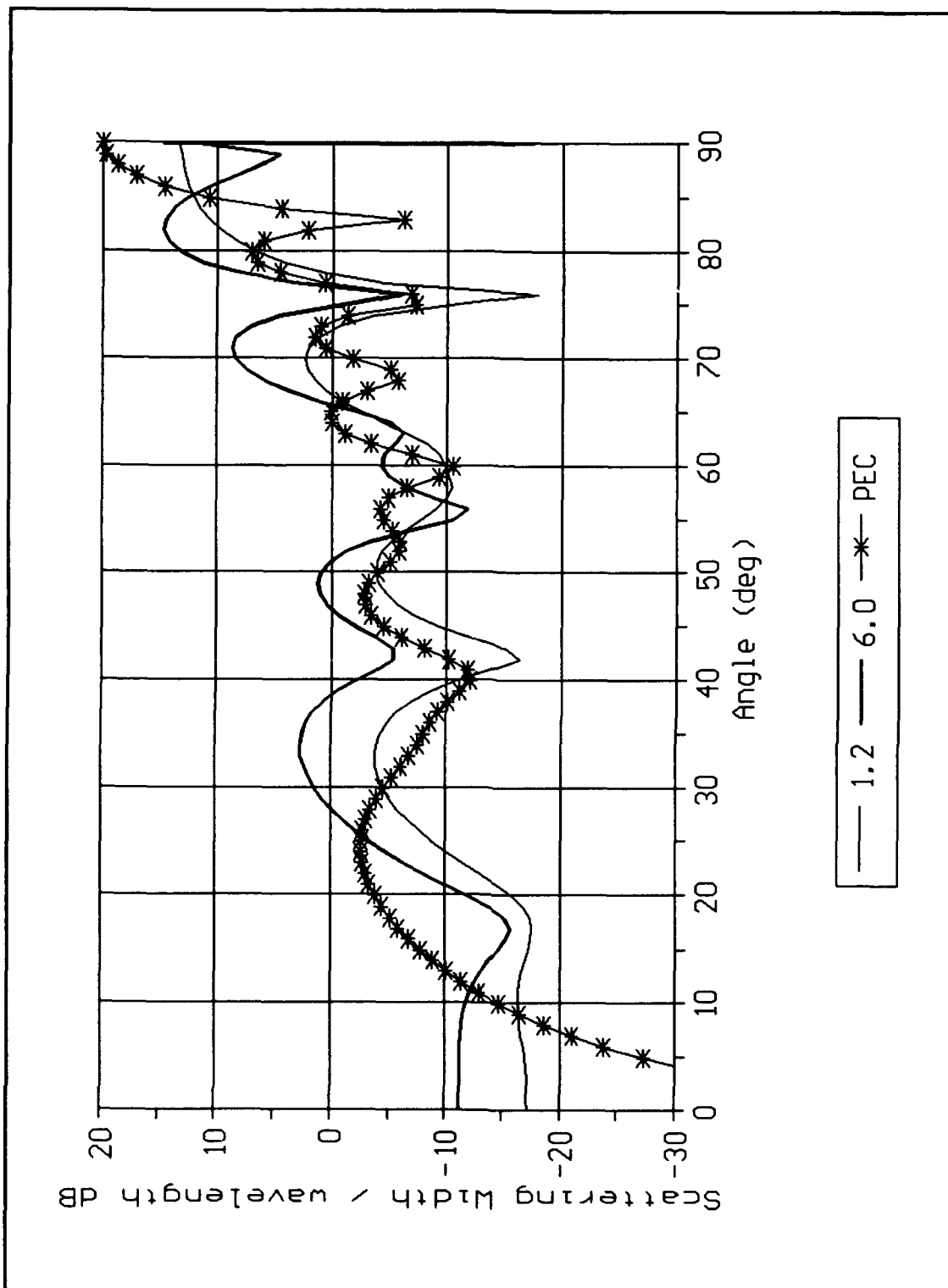


Figure 4.8. Scattering Predictions for a 4λ perfectly conducting strip and 2λ perfectly conducting strips with 1λ loads of impedances, 1.2 and 6.0, H-Polarization.

V. Scattering Measurements

This chapter contains the procedures used to measure the impedance of the materials, and the scattering from the impedance strips and impedance loaded conducting strips, as well as a comparison between predictions and measurements for several strip configurations. First, the procedure is presented to measure the impedance of the four materials used. Second, the procedure used to measure the scattering from the four configurations is presented. Third, an analysis of the accuracy of the code developed is presented.

Impedance Materials

Four materials are used in the thesis. The four materials are Eccosorb SC 100, Eccosorb VF 10, Eccosorb SF 10, and Eccosorb FG 40. The Eccosorb SC 100 is a non-magnetic, 100 ohms per square resistivity, thin (thickness = 0.254 mm), lossy space cloth material made from carbon bonded to a fabric mesh. Eccosorb VF 10 is a non-magnetic, 377 ohms per square resistivity, thin (thickness = 0.254 mm) lossy space cloth material made from carbon in a plastic film. The other two materials are magnetic-dielectric materials. The Eccosorb SF 10 is a thin (thickness = 1 mm), flexible, narrowband, resonant absorber made from a silicon rubber composition. The Eccosorb FG 40 is a thin (thickness = 1.11 mm), hard, broadband absorber made from a silicon rubber.

The SF 10 and FG 40 materials are magnetic radar absorbing materials. In the context of this thesis, they would be impedance materials because their permabilities and permittivities are other than free space and are usually complex.

The thickness of SF 10 and FG 40 compared to the wavelength of measurement (0.0254 m) is 0.03937 and 0.0437, respectively. Therefore, SF 10 and FG 40 satisfy the constraint that the thickness be small with respect to wavelength mentioned in Chapter 2. The requirement of the material being highly absorbing or having a thickness greater than the skin depth will be addressed later in this chapter. The normal attenuation for the frequency of measurement, 11.8 GHz, was not provided in the specification for the two materials. The SF 10 and FG 40 materials are applicable to the impedance boundary conditions.

The SC 100 and VF 10 materials are resistive materials. A resistive material has a permeability of free space and a complex or real permittivity. In addition, a resistive material has a permittivity with the real part not significantly greater than the imaginary part or vice versa. The term R-card is used in the literature for a thin resistive material having a permittivity with an imaginary part significantly greater than the real part. This means the material has a high conductivity, but is extremely thin. An example of an R-card is silver (metal) sputtered on a kaptan substrate (approximately free space substrate).

Measurement.(8) The impedance of the materials were measured at 11.8 GHz using a waveguide precision load, EIP 575 Frequency Counter, 8350B Sweep Oscillator, 8515A Test Set, and a HP 8510B Network Analyzer. The network

analyzer is calibrated to the two waveguides by using a sliding short and a waveguide termination procedure. Once the Network Analyzer is calibrated, the impedance material is placed between the two waveguides. Now the relative permittivity and relative permeability of the material can be calculated from S_{11} and S_{21} values given by the network analyzer (8). S_{11} is a reflection coefficient seen at Port 1, while S_{21} is a transmission coefficient seen at Port 2. Once the permittivity and permeability of the material are known, the surface impedance of the material can be approximated by using Eq (2.6).

Another way to model the surface impedance of the material is via the HP 8510 Smith Chart function which displays the impedance of the material normalized to the wave impedance in the waveguide. The wave impedance in the waveguide is the ratio of the transverse components of the electric and magnetic fields in the waveguide at a specific operating frequency. In free space, the wave impedance is equal to the intrinsic impedance, $120\pi \Omega$.

The waveguide had dimensions $a = 22.86 \text{ mm}$ and $b = 10.16 \text{ mm}$ and the waveguide only supports the TE_{10} mode for the operating frequency 11.8 GHz . The wave impedance in the waveguide is given by

$$Z_{TE, nm} = \frac{120\pi}{\sqrt{1 - (f_{c, nm}/f)^2}} \quad (5.1)$$

and

$$f_{c, nm} = \frac{c}{2\pi} \sqrt{\left(\frac{n\pi}{a}\right)^2 + \left(\frac{m\pi}{b}\right)^2} \quad (5.2)$$

where

c is the speed of light,

n and m are the mode numbers,

f is the operating frequency,

a is the long dimension of the waveguide,

b is the short dimension of the waveguide.

Using Eqs. (5.2) and (5.1), the cutoff frequency for the TE₁₀ mode is 6.557 GHz and the wave impedance in the waveguide is 453.5 Ω.

Heaton (4), using this method measured the impedance of the VF 10 and SC 100 materials normalized to the waveguide as 0.267 + j0.099 and 0.397 + j0.212, respectively. Therefore, the impedances of the VF 10 and SC 100 normalized to free space impedance are 0.3212 + j0.1191 and 0.4775 + j0.255, respectively. The impedances of the other two materials, SF 10 and FG 40, were measured as part of this effort.

When normalized to the free space impedance, the impedance of the SF 10 material is 0.2057 + j0.1816 and the impedance of the FGM 40 material is 0.2201 + j0.1720.

Scattering Configurations

Four configurations were measured: constant impedance strips, constant impedance strips with a perfectly conducting backing, impedance loaded perfectly conducting strips, and impedance loaded perfectly conducting strips with a perfectly conducting backing. All constant impedance strips were 4λ by 6λ . The loaded strips were made of 2λ by 6λ conducting strips loaded with 1λ by 6λ impedance strips on each side of the conducting strip.

The impedance strip with a perfectly conducting backing was chosen as a configuration to determine the accuracy of the impedance strip formulation when the impedance is different on the top and bottom of the strip. Likewise, the impedance loaded strip with a perfectly conducting backing was chosen as a configuration to determine the accuracy of the double wedge formulation when applied to impedance polygons. The impedance loaded strip with a perfectly conducting backing can be modelled as a triangle with one side being an impedance loaded strip and the two other sides being perfect conductors. If the angles between the loaded strip side and perfectly conducting sides are zero then the configuration is an impedance loaded strip with a perfectly conducting backing.

Target Construction. The loaded impedance strips were constructed by sandwiching the impedance material (6 inches by 4 inches) between two perfectly conducting strips (6 inches by 2 inches) and then the conducting strips were taped together. The tape used was a special tape which is made to have a low radar cross section. This tape is called flash breaker tape. The loaded strips with a

perfectly conducting backing were constructed by placing the impedance material (6 inches by 4 inches) on top of a perfectly conducting plate (6 inches by 4 inches) then another perfectly conducting plate (6 inches by 2 inches) was placed on top of the impedance material. The smaller conducting plate was taped to the larger conducting plate using the flash breaker tape. The only other configuration which needed construction was the impedance strip with a conducting backing. This configuration was constructed by taping the impedance material (6 inches by 4 inches) on top of a conducting plate (6 inches by 4 inches).

All of the configurations were placed inside a styrofoam frustrum for measurement. The styrofoam frustrum was split in half so that the strips could be taken in and out easily. The two halves were taped together with the flash breaker tape during measurements. The frustrum also kept the strips vertical so that the strips did not lean forward or backward as they rotated during the measurement. Scattering from the frustrum was low because most of the energy was reflected upward away from the receiver. In addition, the backscatter that did exist from the frustrum was constant for all incident angles. Thus, the frustrum mounting technique provided symmetric scattering patterns for the impedance strip and impedance-loaded strip measurements.

Measurements. All measurements were taken at the AFIT School of Engineering's anechoic chamber. The chamber is a 6 to 18 GHz monostatic far field measurement facility. All of the measurements in this thesis were taken at 11.8 GHz such that the wavelength is 1 inch. Therefore, all the strips measured

were 6λ by 4λ . The plane of measurement is across the width of the strip, 4 inches.

For the predictions, the strips are considered two dimensional. The third dimension in the measurements is 6 inches.

The measurements from the anechoic chamber are in dBsm, decibels per square meter (3 dimensional) and the predictions are made in dB/ λ , decibels per wavelength (2 dimensional), a conversion is required to compare the two sets of scattering data. The dB per wavelength prediction data is converted to dBsm by using the conversions

$$\sigma_{3D} \approx \frac{2l^2}{\lambda} \sigma_{2D} \quad (5.3)$$

and

$$\frac{\sigma_{2D}}{\lambda} (dB) = \sigma_{2D}(dBsm) - 10\log(\lambda) \quad (5.4)$$

where l is the length (third dimension) of the target and λ is the wavelength of the incident energy. The wavelength is 1 inch and the length of the strips is 6 inches. Using the above conversion formulas, -13.33 dB must be added to the prediction data to convert it to decibel per square meter, dBsm.

Predictions vs Measurements

As a reminder, the impedance strip predictions (with and without a conductor backing) are made using the impedance half plane formulation, the loaded strip predictions are made using the impedance wedge formulation with the revised three-vertex triple diffraction, and the loaded strip with conductor backing predictions are made using the impedance wedge formulation with the three-vertex triple diffraction.

The impedances for the materials used in all predictions are the impedances measured using the waveguide technique. The measured impedances for the SC 100, VF 10, SF 10, and FG 40 are $0.4775 + j0.255$, $0.3212 + j0.1191$, $0.2057 + j0.1816$, and $0.2201 + j0.1720$, respectively. The impedance of a perfect conductor is modelled as $0.0 + j0.0$.

The prediction program used for the impedance strips allows the impedances on the top and bottom of the strip be different. Therefore, for constant impedance strips the same impedance is assumed to be on the top and bottom of the strip. For constant impedance strips with a perfectly conducting backing, the top impedance is assumed to be the measured impedance of the material while the bottom is a perfectly conductor impedance ($0.0 + j0.0$).

The prediction program used for the impedance loaded strip does not consider the top and bottom of the strip to have different impedances. For the prediction of the impedance loaded strip with a perfectly conducting backing, the strip must be modeled as an impedance polygon. The loaded strip with a conductor backing is modelled by a triangle with sides of length 4λ , 2.000025λ ,

and 2.000025λ . The 4λ side is the loaded strip while the other two sides are perfectly conducting.

For the impedance strip predictions and measurements, the materials considered are SF 10 and FG 40. On the other hand, for the impedance loaded strip predictions and measurements, the materials considered are SC 100, VF 10, SF 10, and FG 40.

The impedance half plane formulation uses the impedance half plane IBC developed by Senior which considers an impedance half plane as the superposition of a resistive half plane and a conductive half plane. The impedance wedge formulation uses the half space IBC which does not make any distinction between resistive wedges and conductive wedges. Both formulations use the same assumptions for the equivalent surface impedance. During this thesis, it was found that the impedance wedge formulation gave excellent results compared to measurements of conducting strips loaded with SC 100 and VF 10 (figures 5.9 through 5.12). These materials are not impedance materials. They are resistive materials. Measurements and predictions were also made using the impedance half plane formulation for impedance strips with the materials SC 100 and VF 10. The predictions compared to measurements were low by 5 dBsm or more, but the lobe placement and number was the same. These comparisons are not presented.

The fact that the impedance wedge formulation gave excellent results for resistive materials and the impedance half plane formulation did not is not understood.

Impedance Strips. Figures 5.1 and 5.2 are the plots of the predictions and measurements for a 4λ (4 inches by 6 inches) perfectly conducting strip (flat plate) for E- and H-polarizations, respectively.

There are three formulas which can be used to confirm the predictions and measurements for a perfectly conducting strip (plate). One formula is the traveling wave lobe equation for H-polarization. For H-polarization, a traveling wave exists on a perfectly conducting strip. This traveling wave on the strip produces a lobe in the scattering pattern. The formula which provides the location of the traveling wave lobe is

$$\theta = 49.35 \sqrt{\frac{\lambda}{l}} \quad (5.5)$$

where

l is width of the strip,

λ is the wavelength of the incident wave,

θ is the observation angle measured from edge-on.

The second formula is for the prediction of the scattering at edge-on with the polarization parallel to the edge (E-polarization). The formula is

$$\sigma = \frac{l^2}{\pi} \quad (5.6)$$

where l is the length of the edge (6 inches for the plate). The third formula for the broadside scattering from a flat plate is

$$\sigma = 4\pi \frac{A^2}{\lambda^2} \quad (5.7)$$

where A is the area (6 inches by 4 inches) of the perfectly conducting plate and λ is the wavelength (1 inch) of the incident wave. This formula is polarization independent.

Using the traveling wave lobe formula, a traveling wave lobe should exist at 24.68 degrees from edge-on. Inspecting figure 5.2, the traveling wave lobe does exist in the measurements and predictions. Using Eq (5.6), the scattering at edge-on for E-polarization should be -21.31 dBsm. From figure 5.1, the scattering for the measurement at edge-on is -22 dBsm and for the prediction at edge-on is -21.5 dBsm. The edge-on scattering formula has better agreement with the prediction than the measurement. Using Eq (5.7), the broadside scattering for the strip (plate) should be 6.693 dBsm. In figure 5.1, the broadside scattering for the measurement is about 5.5 dBsm and for the predictions is about 6.5 dBsm. In figure 5.2, the broadside scattering for the measurement and for the prediction is about 6.5 dBsm. In general, the formulas agree better with the prediction than the measurement of the perfectly conducting plate. One characteristic of the measurements for both E- and H-polarization compared against the predictions is the sidelobes are shifted backward toward edge-on for E-polarization and shifted forward toward broadside for H-polarization. This shifted feature would mean

the plate was tilted backward for the E-polarization measurement and forward for the H-polarization measurement. A tilt of the plate during measurement would also give a lower broadside scattering.

Figures 5.3 to 5.8 show the measurements against predictions for the constant impedance strips with and without perfectly conducting backing for both E- and H- polarizations. The impedance materials considered are the SF 10 and FG 40. The impedance strips are 4λ in width and 6λ in length (4 inches by 6 inches impedance plate).

Figures 5.3 through 5.5 are the predictions against the measurements when the impedance material is SF 10 for an impedance strip with E-polarization, impedance strip with conducting backing for E-polarization, and impedance strip with H-polarization, respectively. Figure 5.3 exhibits the same shift in lobe placement as seen for the perfect conductor measurements. The mainbeam of the predictions is about 2 dBsm below the measurement. Since the prediction is low the difference in the mainbeam can not be explained by a possible tilt in the strip during measurement. The only way to explain a low prediction is by the surface impedance of the material used in the prediction being incorrect. At edge-on, the difference in the two patterns although small can be due to the impedance used in the prediction is for normal incidence. As mentioned in Chapter 2, the surface impedance is really a function of incident angle which the formulation does not consider: the surface impedance is assumed constant for all angles of incidence.

In figure 5.4, the prediction is 2 to 3 dBsm greater than the measurement. The difference in this plot must be due purely to the modelling of the surface

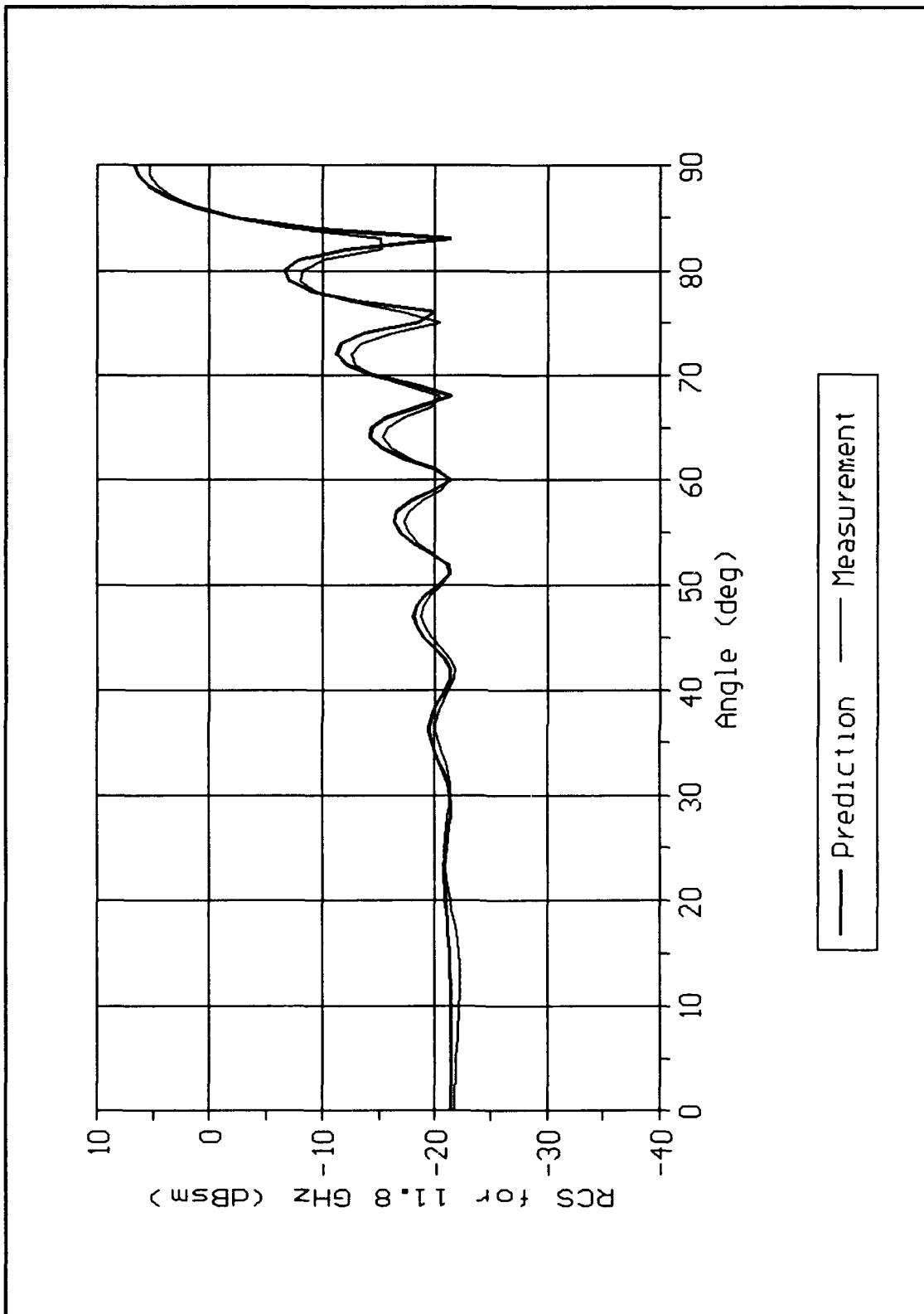


Figure 5.1. Comparison of measured and predicted monostatic scattering pattern for a 4 inches by 6 inches perfectly conducting strip at 11.8 GHz, E-polarization.

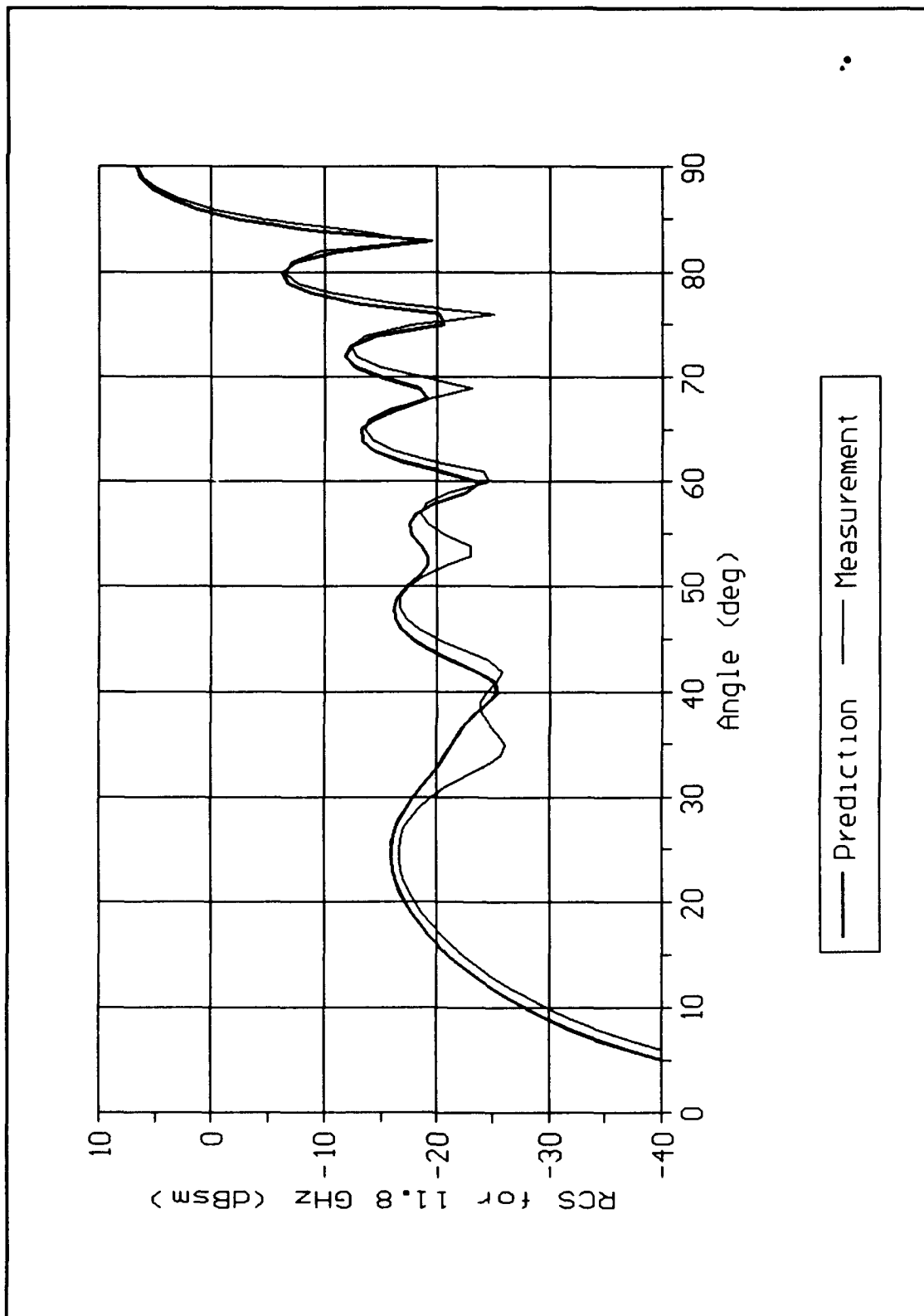


Figure 5.2. Comparison of measured and predicted monostatic scattering pattern for a 4 inches by 6 inches perfectly conducting strip at 11.8 GHz, H-polarization.

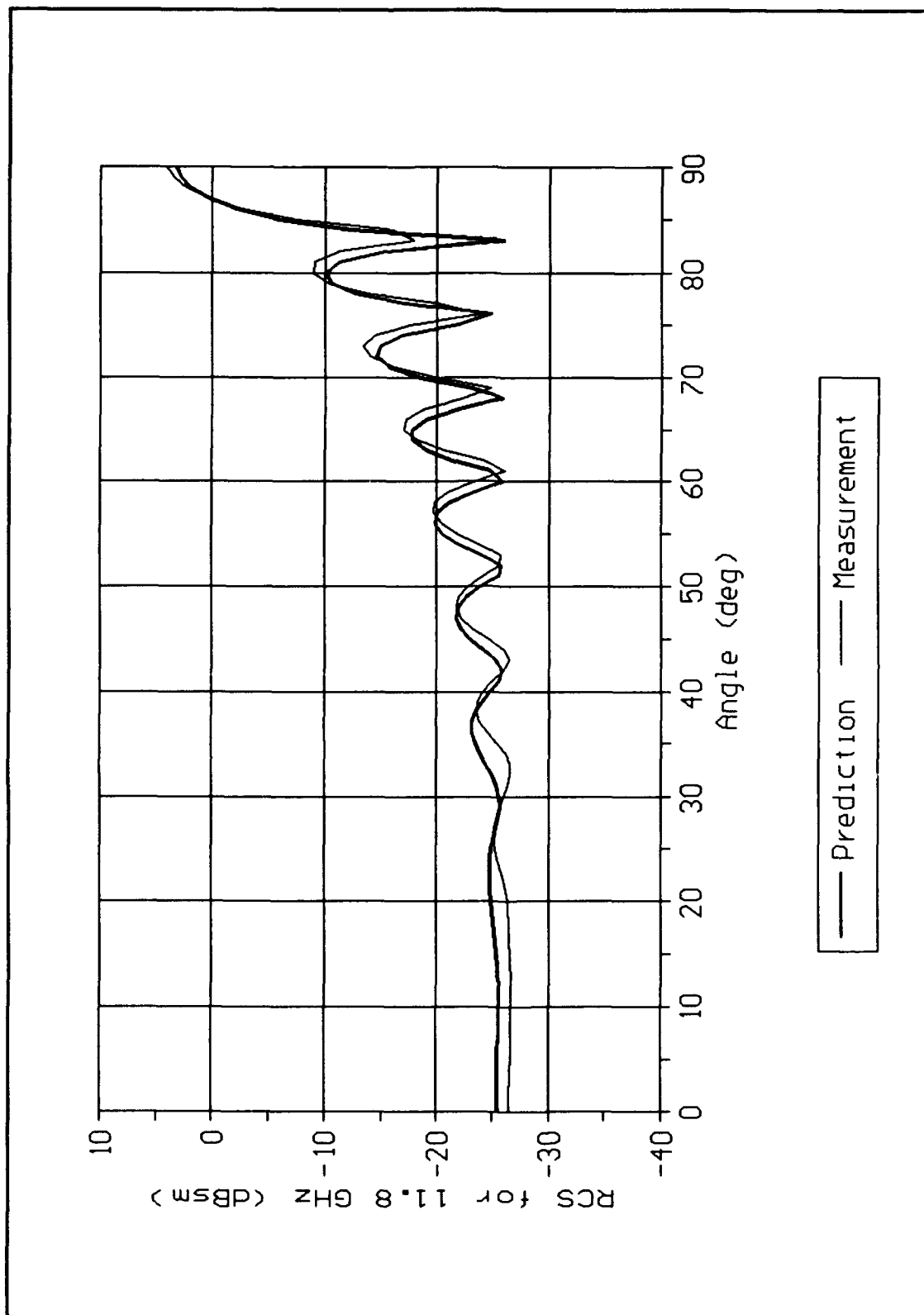


Figure 5.3. Comparison of measured and predicted monostatic scattering pattern for a 4 inches by 6 inches, SF 10, impedance strip at 11.8 GHz, E-polarization.

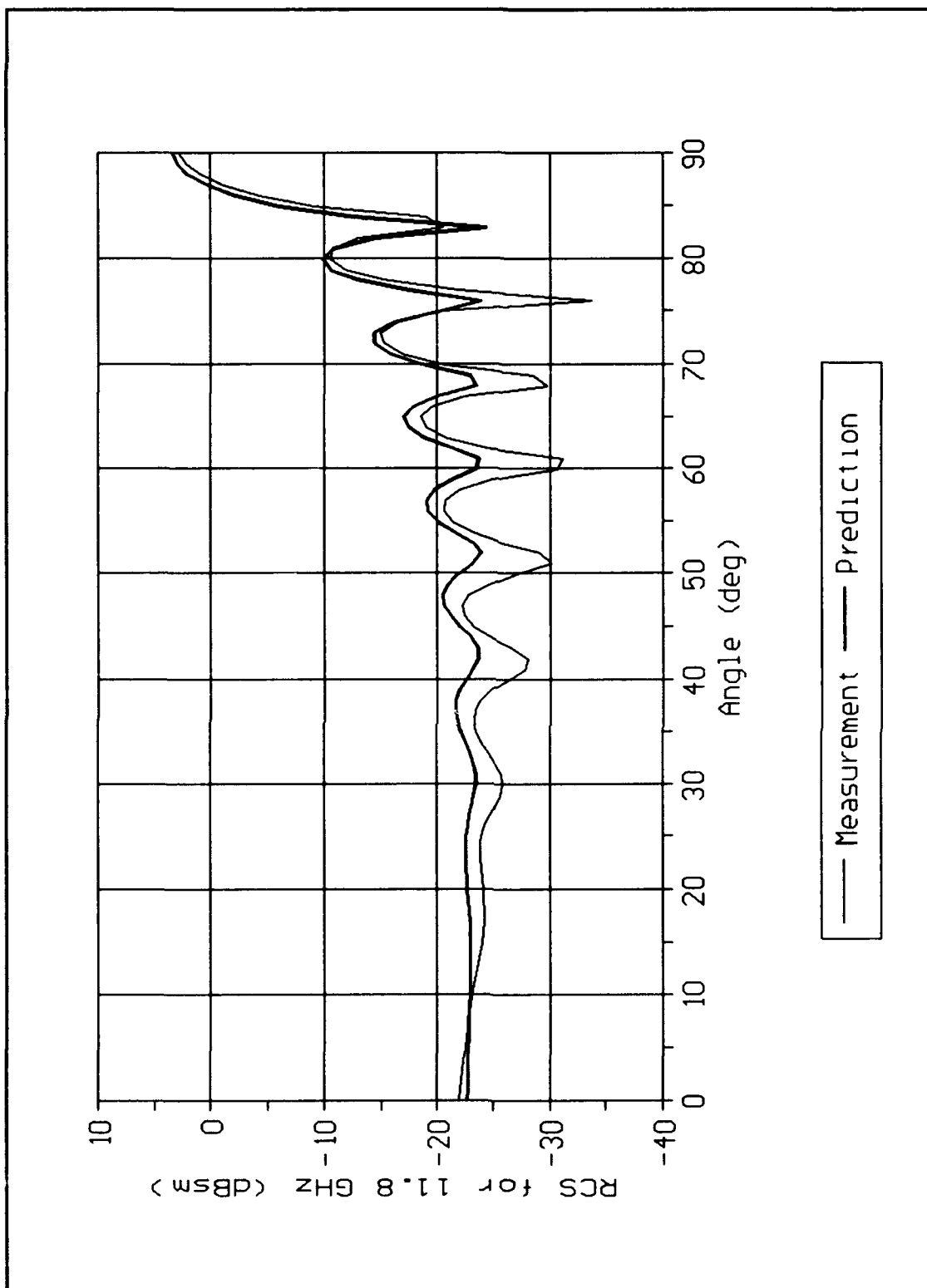


Figure 5.4. Comparison of measured and predicted monostatic scattering pattern for a 4 inches by 6 inches, SF 10, impedance strip with a perfectly conductor backing at 11.8 GHz, E-polarization.

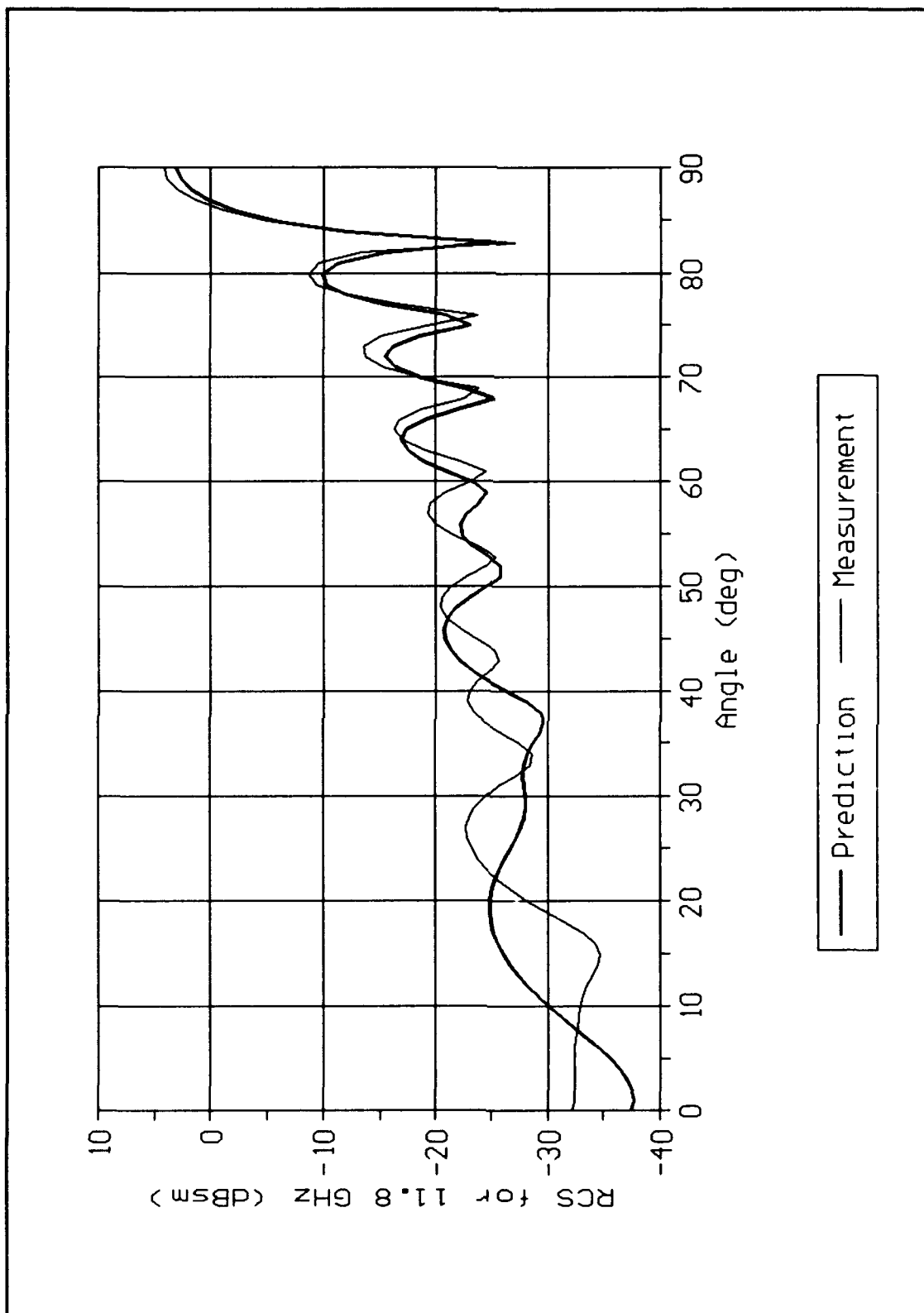


Figure 5.5. Comparison of measured and predicted monostatic scattering pattern of a 4 inches by 6 inches, SF 10, impedance strip at 11.8 GHz, H-polarization.

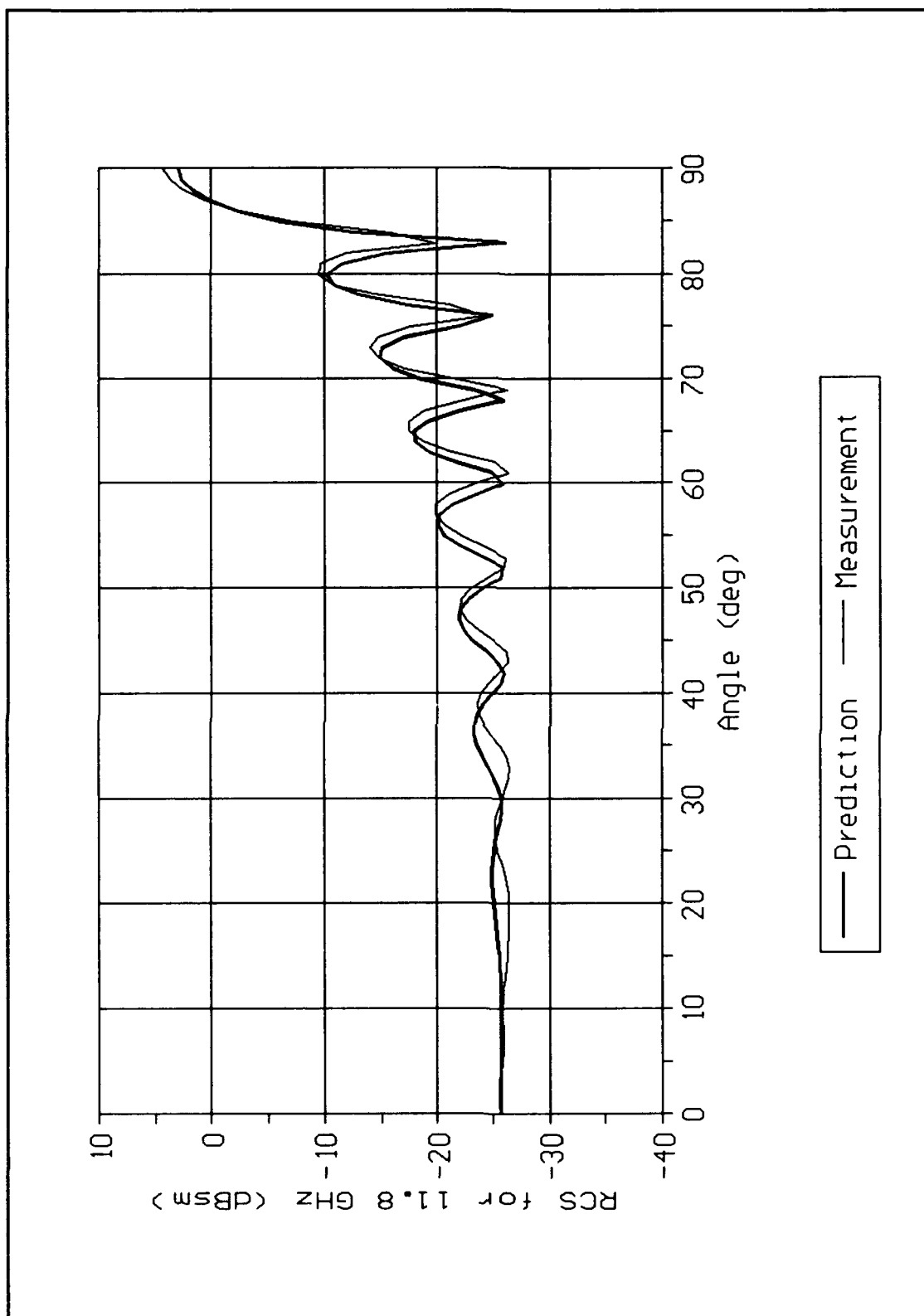


Figure 5.6. Comparison of measured and predicted monostatic scattering pattern for a 4 inches by 6 inches, FG 40, impedance strip at 11.8 GHz, E-polarization.

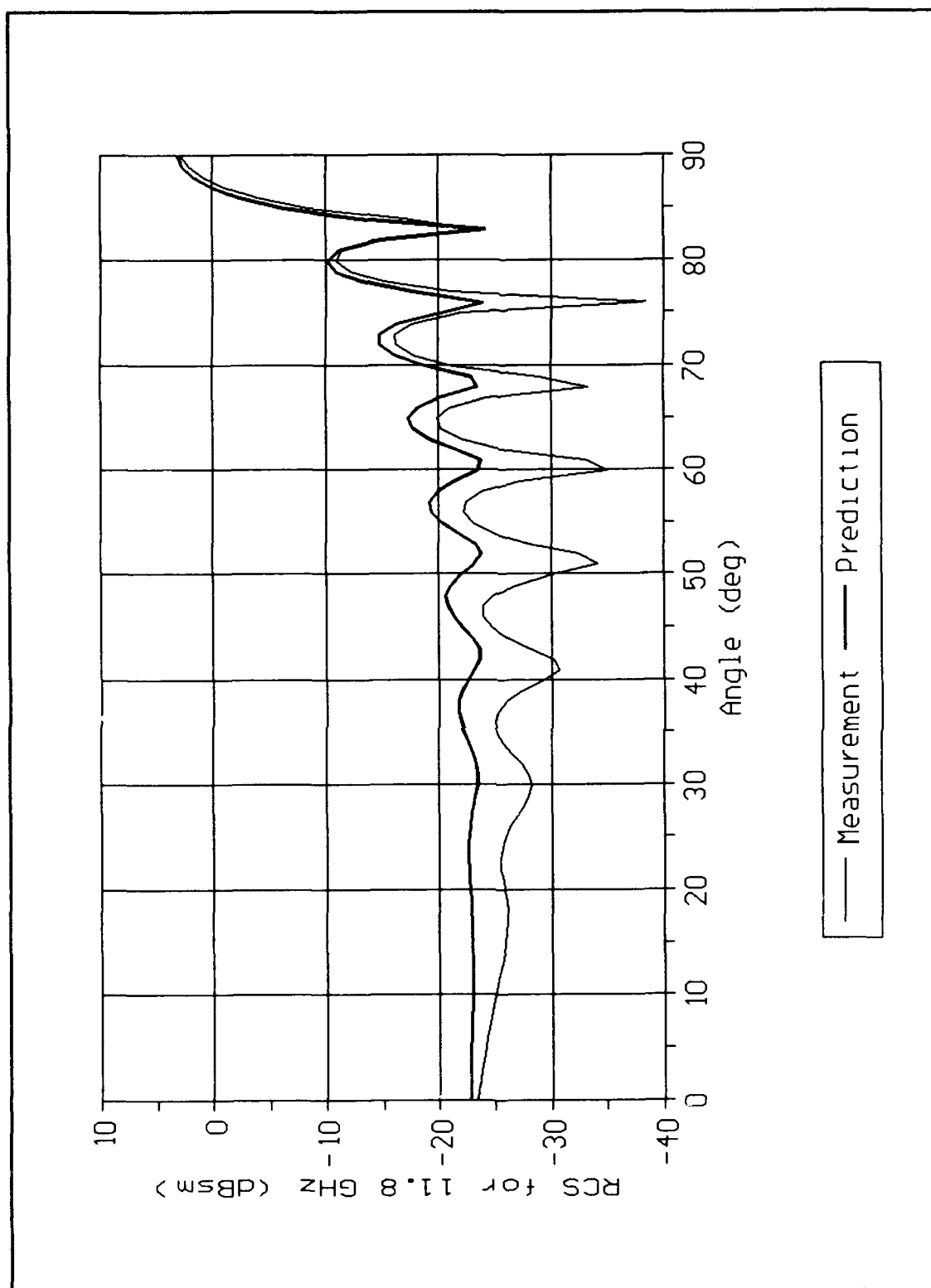


Figure 5.7. Comparison of measured and predicted monostatic scattering pattern for a 4 inches by 6 inches, FG 40, impedance strip with a perfect conductor backing at 11.8 GHz, E-polarization.

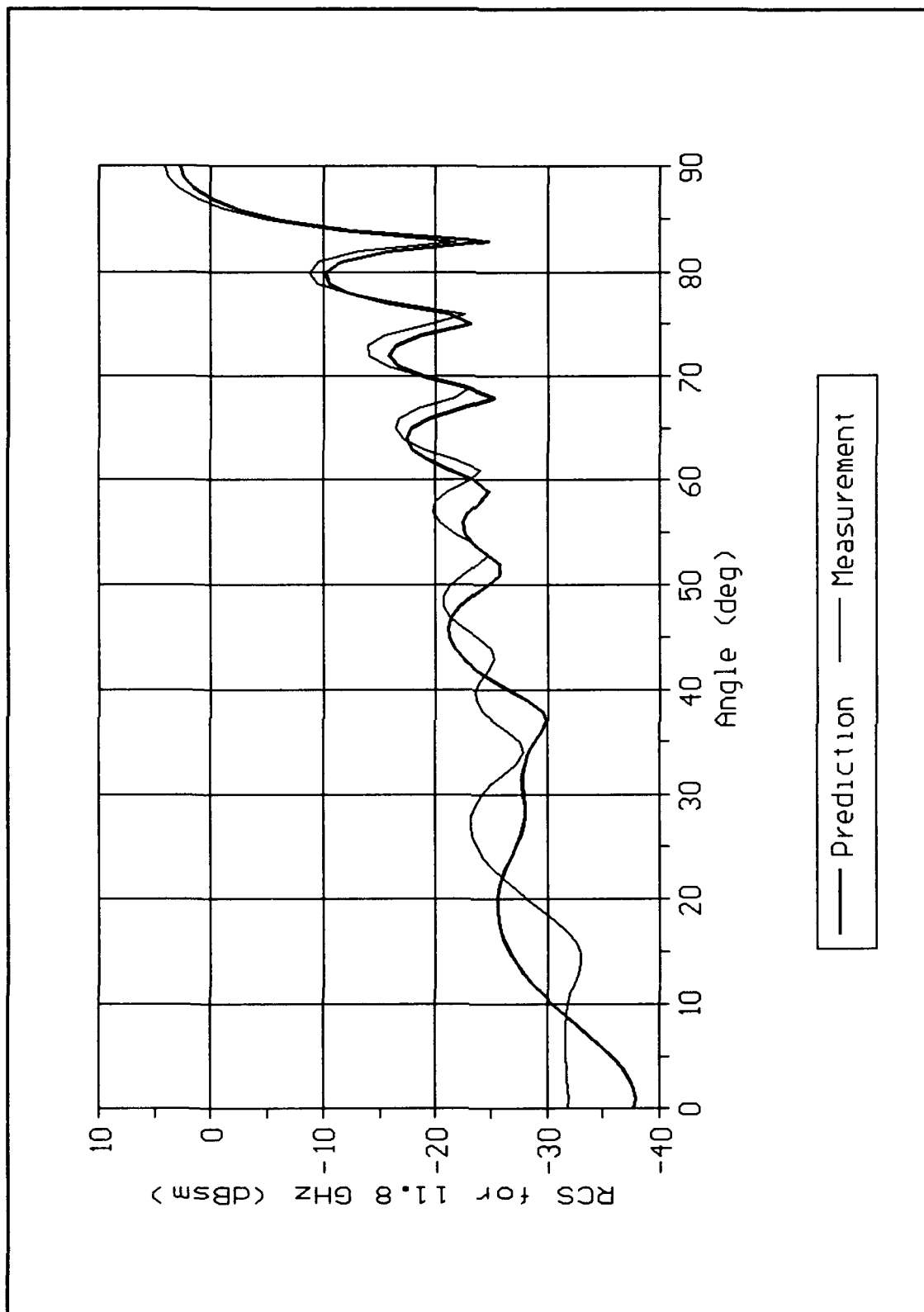


Figure 5.8. Comparison of measured and predicted monostatic scattering pattern for a 4 inches by 6 inches, FG 40, impedance strip at 11.8 GHz, H-polarization.

impedance. The strip is made of a magnetic absorbing material (SF 10) on top of a perfect conductor. The measurement shows the amount of absorption changing with incident angle. The measurement shows the absorption changing with incident angle, but at edge-on the scattering level is the same as the perfectly conducting strip measurement (figure 5.1). If the surface impedance was modelled correctly as a function of incident angle, the prediction would be expected to show a better agreement with the measurement.

Comparing figures 5.1 and 5.4, the amount of absorption at normal incidence provided by the SF 10 material is 2.52 dBsm. Remembering the SF 10 material is a magnetic radar absorbing material which is designed to absorb radar energy when placed on top of a perfect conductor, the surface impedance required in the prediction (IBC) is different when the SF 10 material is placed on top of the conductor. Therefore, the surface impedance measured in the waveguide with the SF 10 material alone is not necessarily the correct impedance value for the SF 10 on top of the conductor configuration. On the other hand, the measurement and prediction for the SF 10 material on top of the perfect conductor (figure 5.4) is only off at normal incidence by 0.5198 dBsm. This agreement is good, but the prediction is higher than the measurement at broadside. If the waveguide measurement for the surface impedance would of been with the SF 10 material on top of the conductor, the surface impedance used in the prediction for the SF 10 on top of the conductor have been different and more representative of the surface impedance seen by the incident wave during the measurement. Therefore, when modelling the surface impedance of a

configuration, the effective surface impedance is required in the prediction, not the surface impedance of the outer layer of the configuration. In addition, if the effective impedance of the configuration was not measurable then transmission line theory could be used to find the surface impedance for a multilayered configuration.

Figure 5.5 shows the measurement versus prediction for the SF 10 impedance strip and H-polarization. The prediction is low in the mainbeam by 2 dBsm and the shift in lobe structure in this plot is more prominent than exhibited in other plots. An explanation is the formulation is not accounting for the surface waves on the strip well.

As noticed there are no predictions for these materials for H-polarization with conducting backings, this is because the code gave incorrect values for the scattering. The measurements for this case were made but are not presented because of the inaccurate predictions achieved. The cause of the inaccurate H-polarization predictions may be contributed to a numerical problem in the prediction. For H-polarization, the equation $\sin \theta = 1/\eta$ must be solved for θ . The problem occurs in solving for the complex angle θ when $1/\eta$ is large.

Figures 5.6 through 5.8 are the predictions against the measurements when the impedance material is FG 40 for an impedance strip for E-polarization, impedance strip with conducting backing for E-polarization, and impedance strip for H-polarization, respectively. All three figures show the same discrepancies between measurements and predictions as the case when the strips were made of SF 10.

Loaded-Impedance Strips. Figures 5.9 thru 5.20 are the comparisons between predictions and measurements for all impedance loaded-strip configurations. The materials used for loading were SC 100, VF 10, SF 10, and FG 40. As a reminder, the loaded strip configuration is a 2λ perfectly conducting strip with 1λ impedance loads attached (2 inch by 1 inch conducting plate with 1 inch by 6 inches impedance loads). These 4λ loaded strips were measured and predicted for a perfectly conducting backing and without a perfectly conducting backing.

Figures 5.9 thru 5.12 show the comparisons between the measurements and predictions for both polarizations when the loads are the SC 100 and VF 10 materials. All of the predictions in figures 5.9 thru 5.12 are low in the mainbeam by 2 dB or less except for figure 5.9 where the prediction and measurement agree.

The prediction for the SC 100 loaded strip and E-polarization, figure 5.9, shows excellent agreement with the measurements for all angles. The prediction for the SC 100 loaded strip and H-polarization is off by 2 dBsm in the mainlobe, but the sidelobes for 50 degrees or more show good agreement with the measurement.

The predictions versus measurements for E-polarization and H-polarization when the strip is loaded with VF 10 are in figures 5.11 and 5.12, respectively. For both polarizations, the predictions accurately predict the first two sidelobes in placement, but the sidelobe levels are off by 5 dBsm or less. In addition, for both polarizations, the mainbeam prediction is low. Figures 5.13 thru 5.16 are the plots of the predictions vs measurements when the strip is loaded with SF 10 material for both polarizations and with and without a conductor backing. The

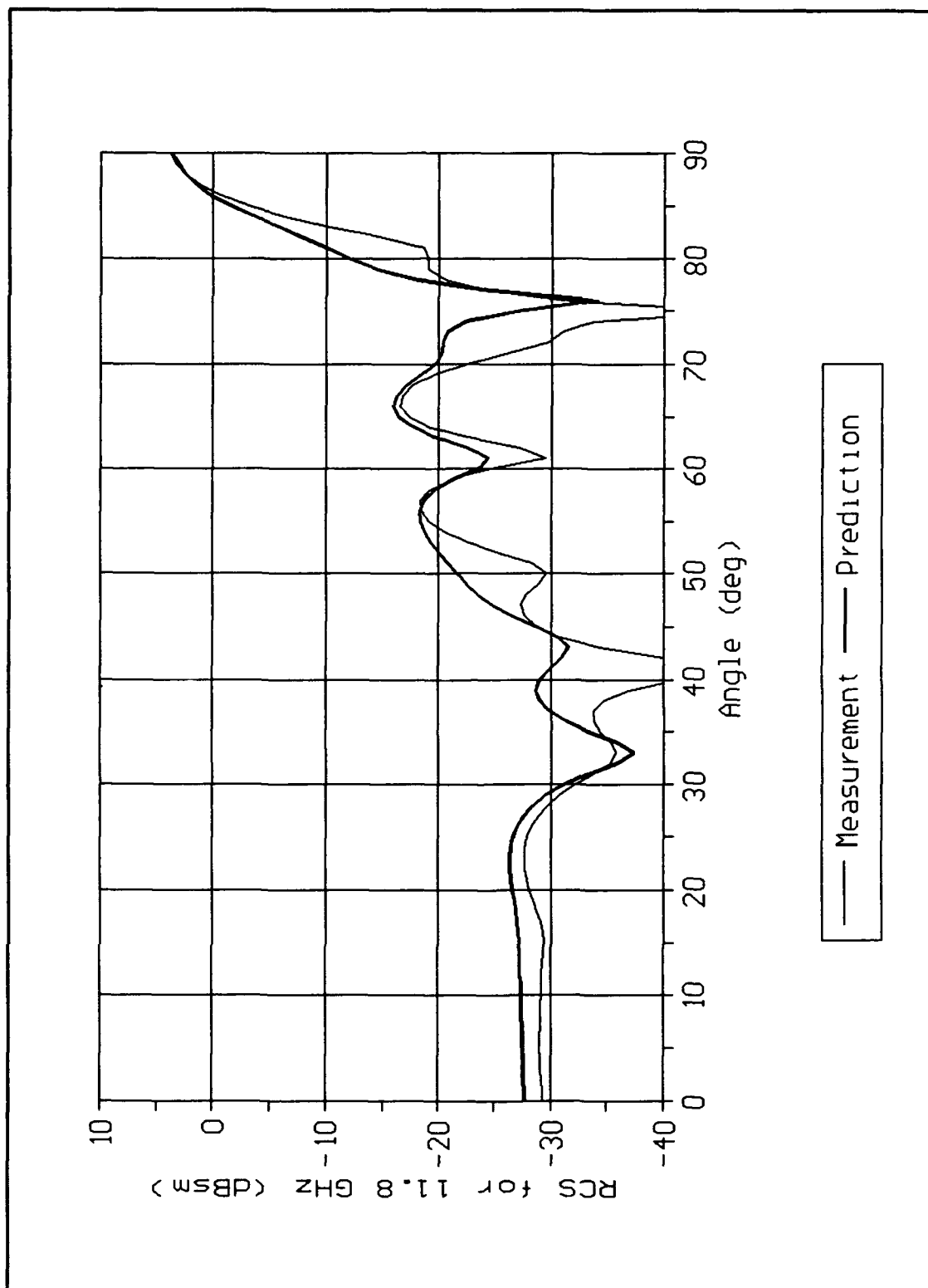


Figure 5.9. Comparison of measured and predicted monostatic scattering pattern for a 4 inches by 6 inches conducting strip with 1 inch by 6 inches loads, SC 100, at 11.8 GHz, E-polarization.

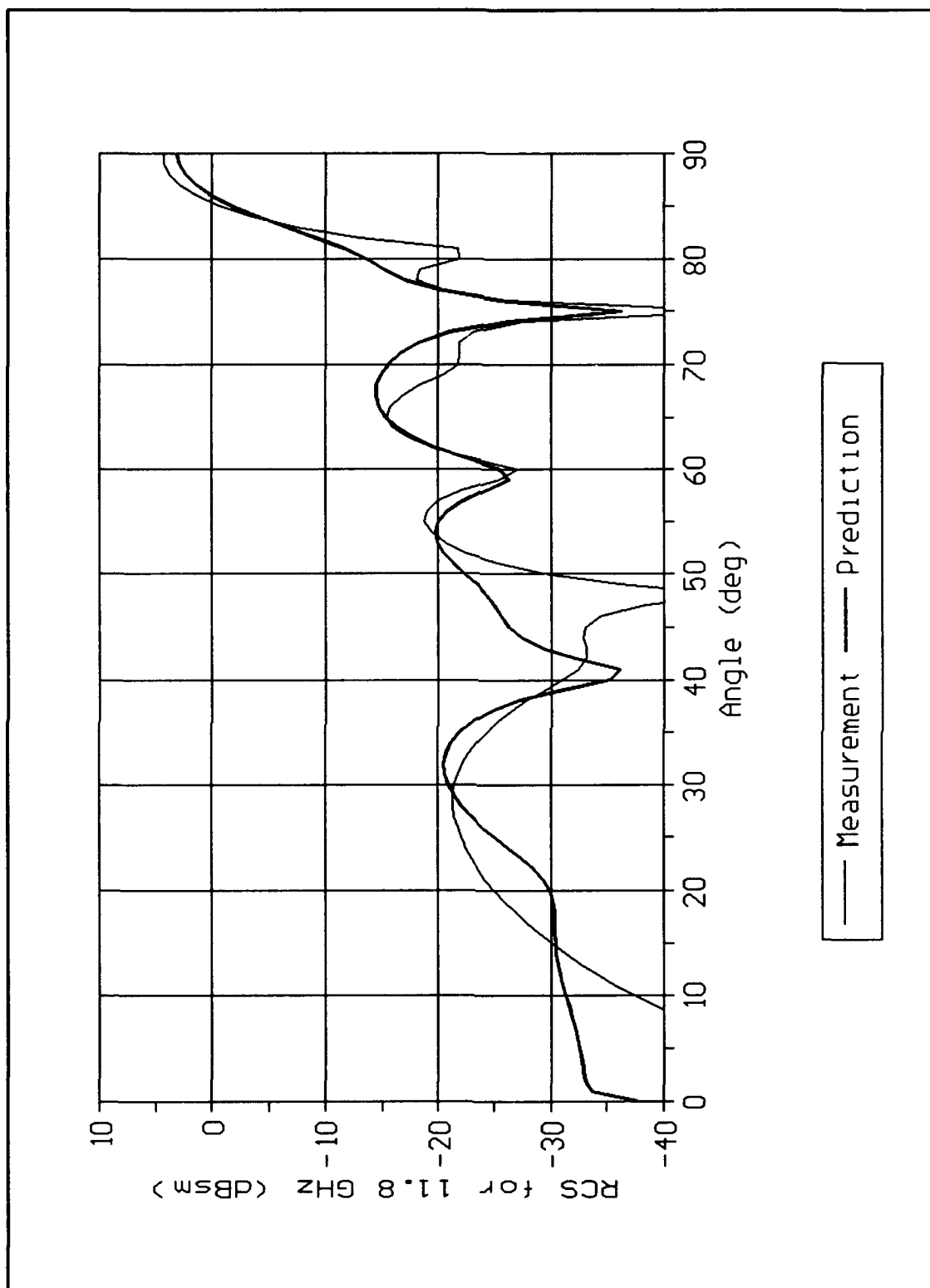


Figure 5.10. Comparison of measured and predicted monostatic scattering pattern for a 4 inches by 6 inches conducting strip with 1 inch by 6 inches loads, SC 100, at 11.8 GHz, H-polarization.

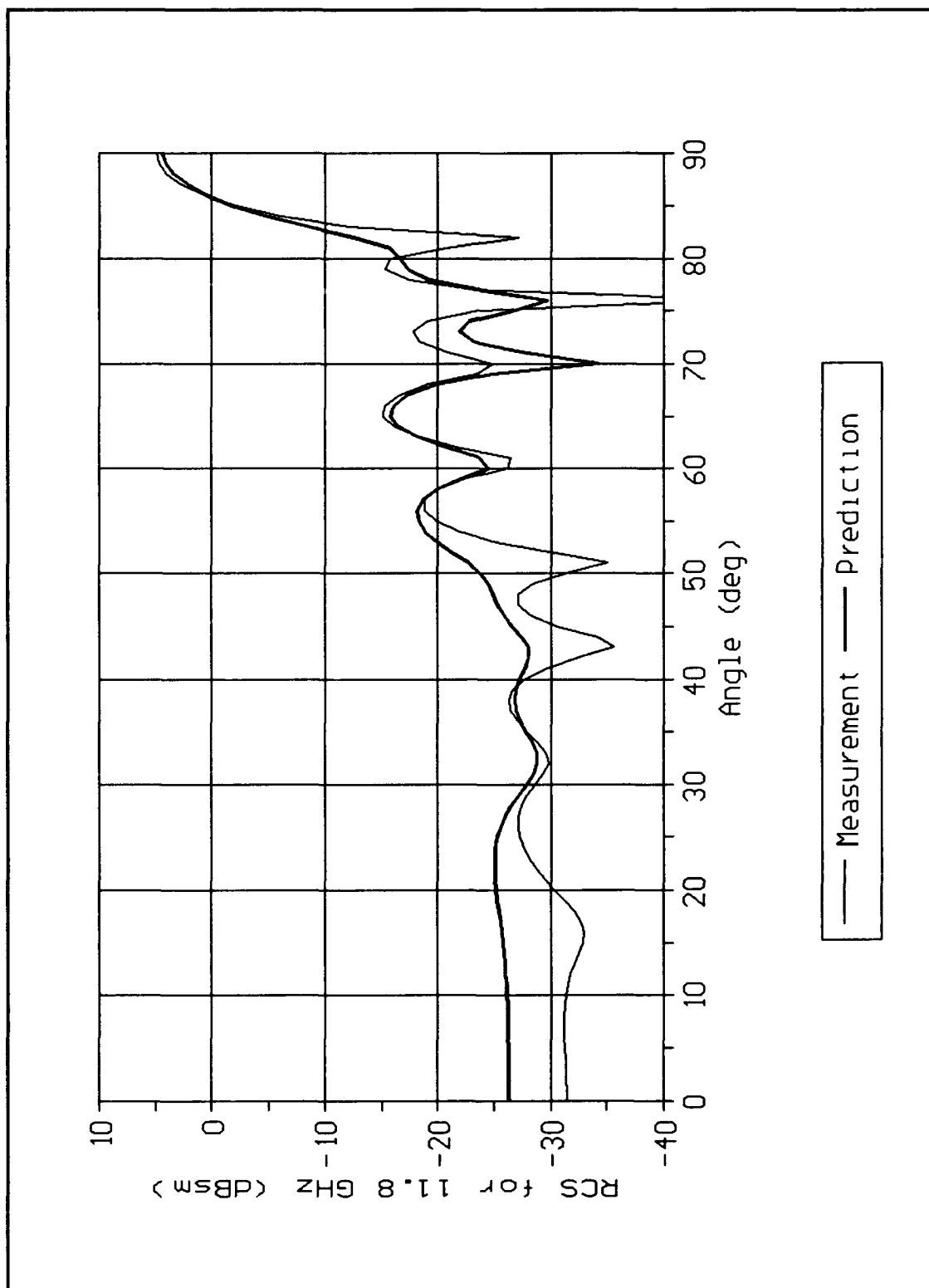


Figure 5.11. Comparison of measured and predicted monostatic scattering pattern for a 4 inches by 6 inches conducting strip 1 inch by 6 inches loads, VF 10, at 11.8 GHz, E-polarization.

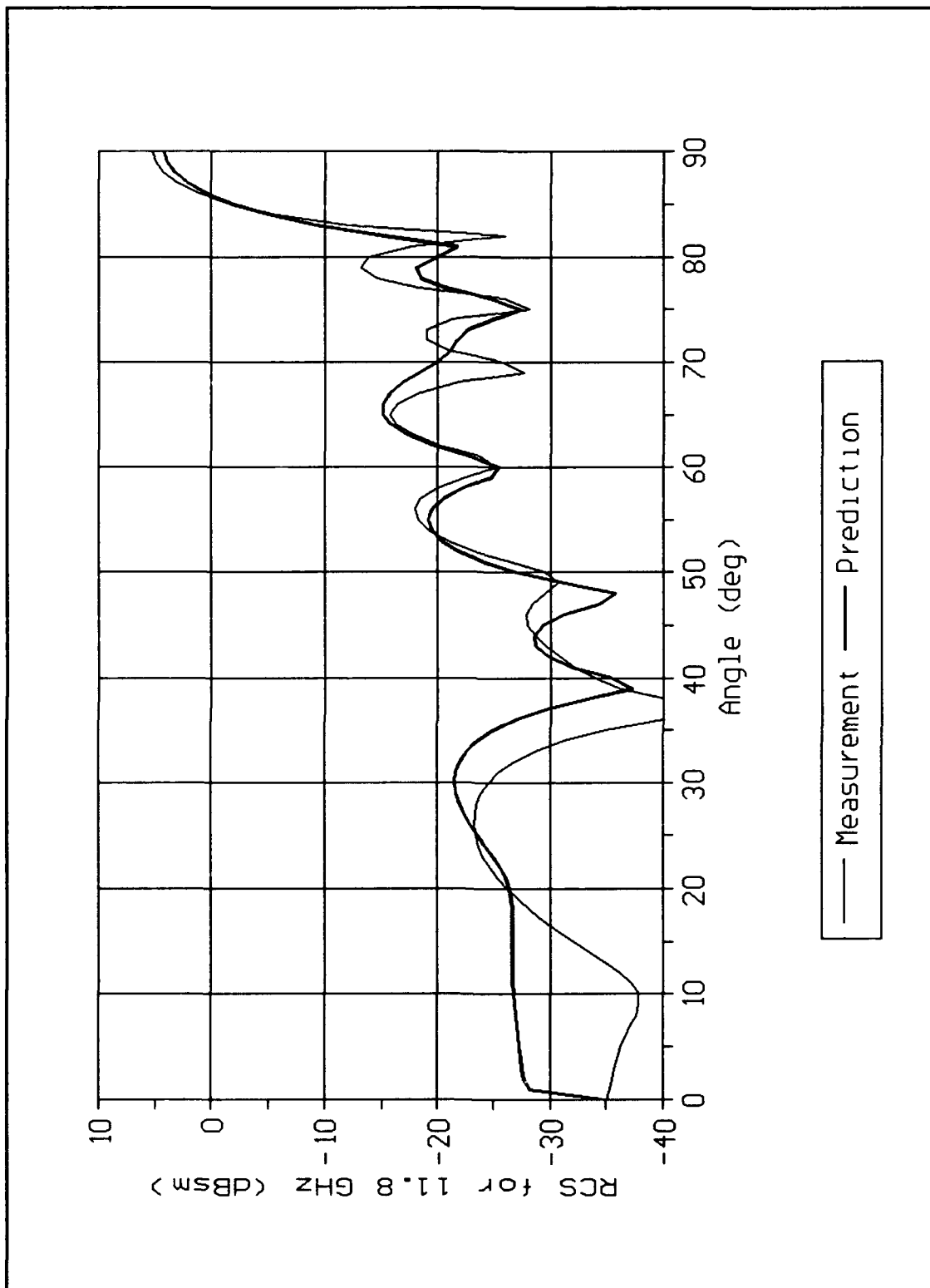


Figure 5.12. Comparison of measured and predicted monostatic scattering pattern for a 4 inches by 6 inches conducting strip with 1 inch by 6 inches loads, VF 10, at 11.8 GHz, H-polarization.

prediction for E-polarization and no backing shows the best agreement with the measurements when the load is SF 10. The prediction for E-polarization with a conductor backing, figure 5.14, compares well to the measurement for angles 50 degrees or greater. The H-polarization predictions, figures 5.15 and 5.16, do not compare to the measurements as well as the E-polarization predictions to measurements. Both H-polarization plots for SF 10 loads with and without a perfectly conducting backing exhibit the shift seen in the impedance strip predictions to measurements. In general, the conductor backed predictions do not compare as well as the non-backing predictions to the respective measurements. This may be explained by the surface impedance used to model the loads when the impedance loaded strip is mounted on top of a conductor backing not accounting for the change in surface impedance when a magnetic radar absorbing material is on top of a conductor. This change in surface impedance for a magnetic radar absorbing material was discussed in the impedance strip section.

Figures 5.17 thru 5.20 are the plots of the predictions vs measurements for the loaded strips being FG 40 material for both polarizations and with and without a conductor backing. The same trends are shown in these plots as in the case when the loads are SF 10 material.

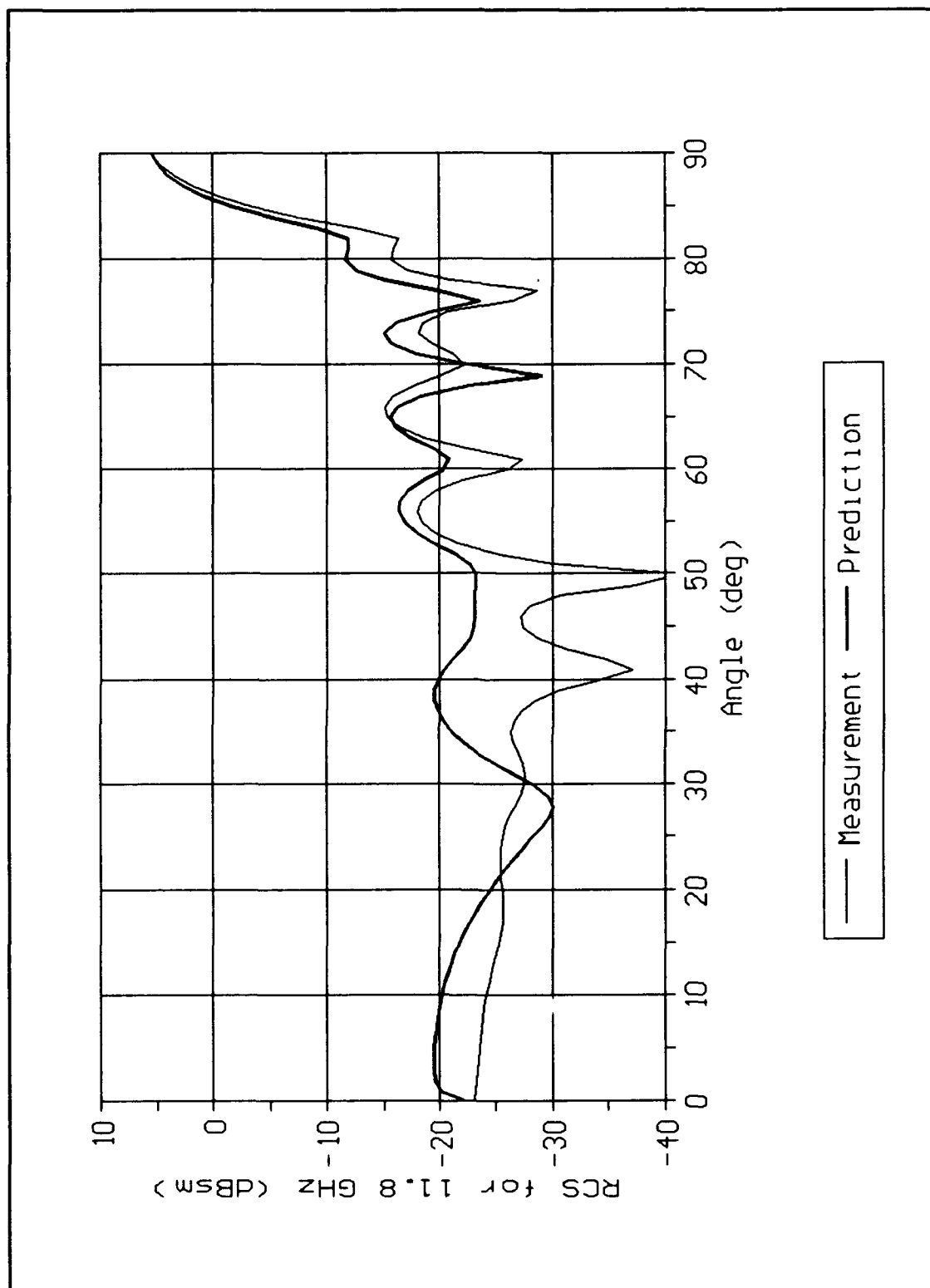


Figure 5.13. Comparison of measured and predicted monostatic scattering pattern for a 4 inches by 6 inches conducting strip with 1 inch by 6 inches loads, SF 10, and a perfect conductor backing at 11.8 GHz, E-polarization.

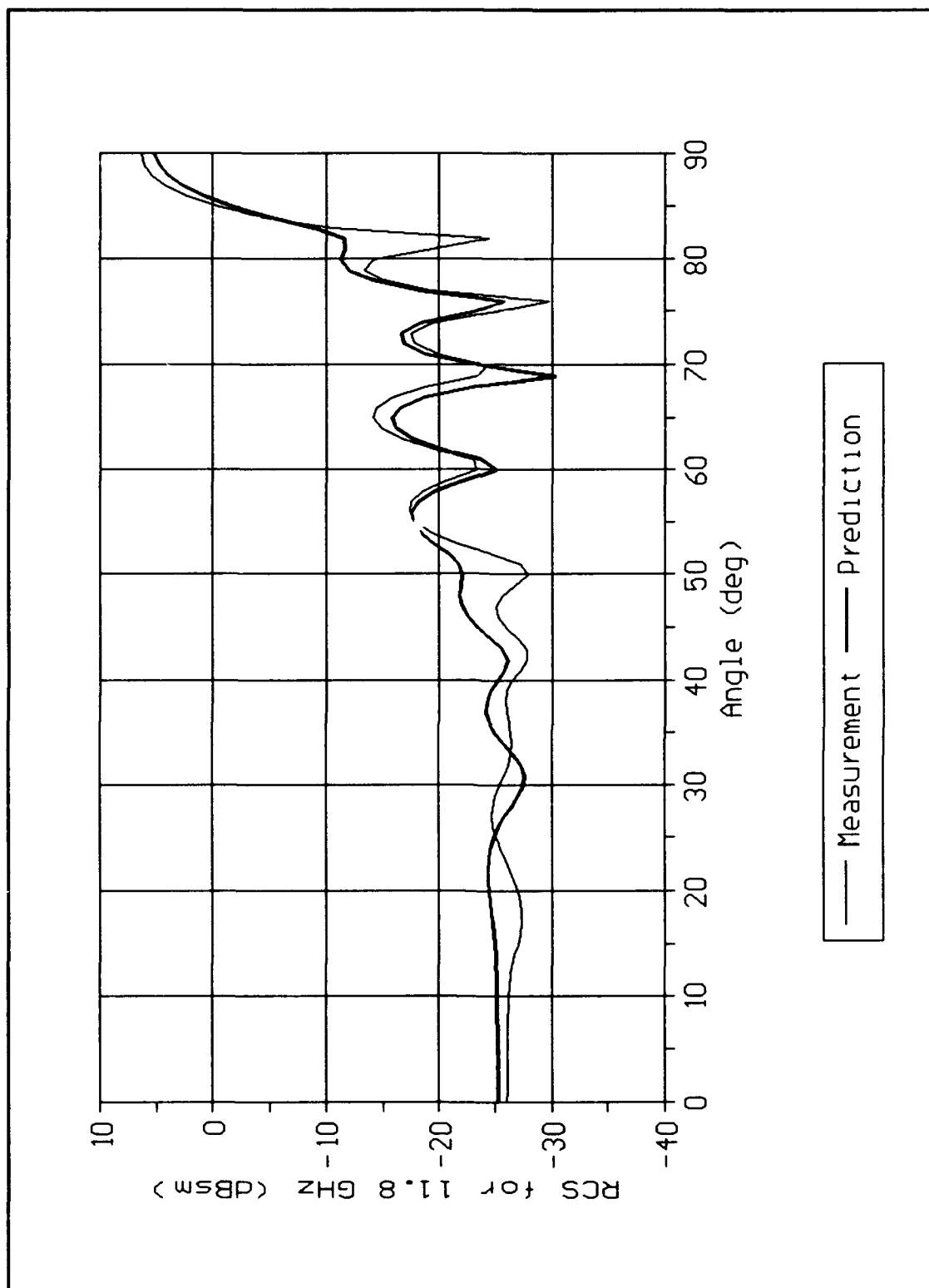


Figure 5.14. Comparison of measured and predicted monostatic scattering pattern for a 4 inches by 6 inches conducting strip with 1 inch by 6 inches loads, SF 10, at 11.8 GHz, E-polarization.

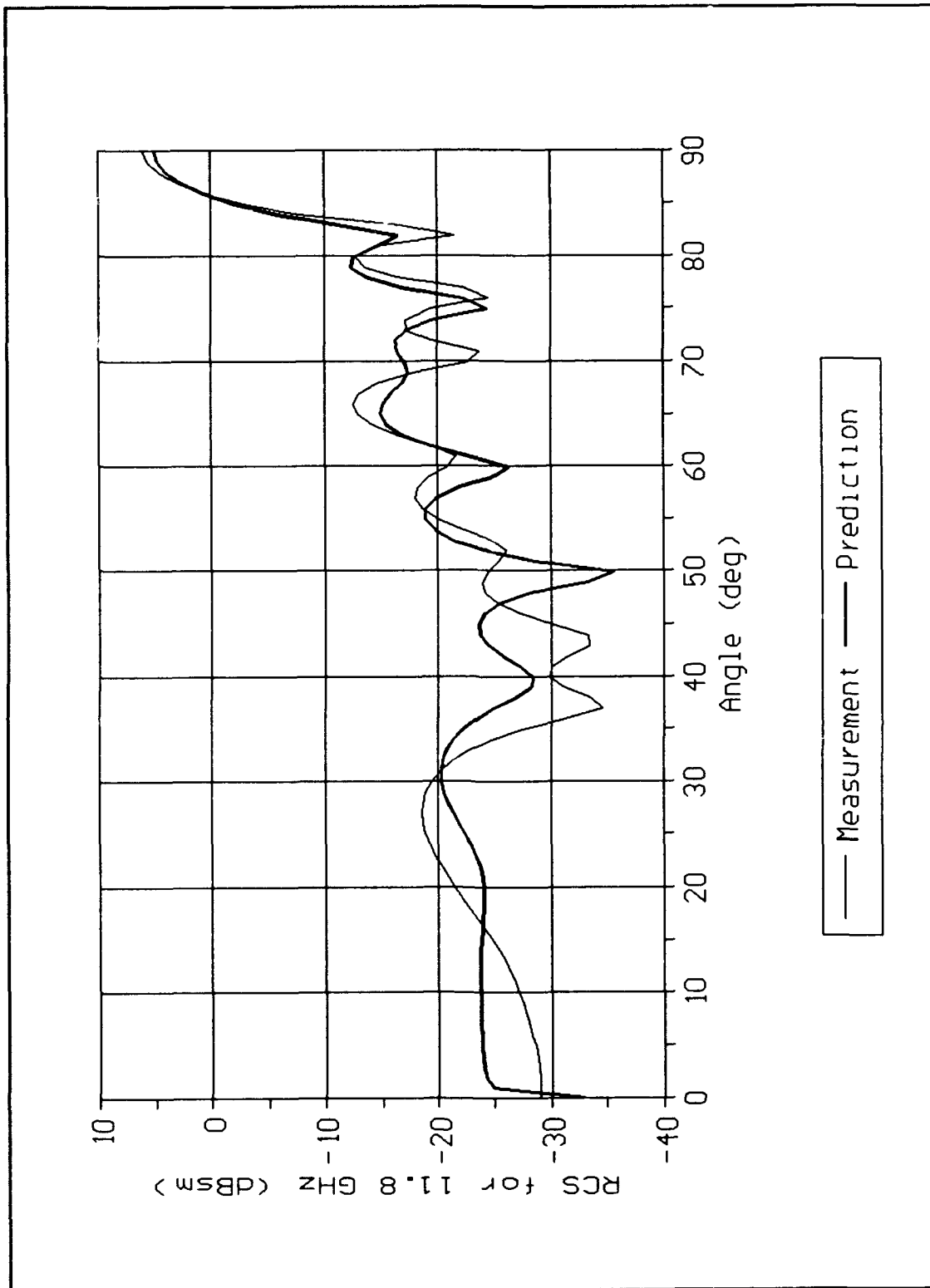


Figure 5.15. Comparison of measured and predicted monostatic scattering pattern for a 4 inches by 6 inches conducting strip with 1 inch by 6 inches loads, SF 10, at 11.8 GHz, H-polarization.

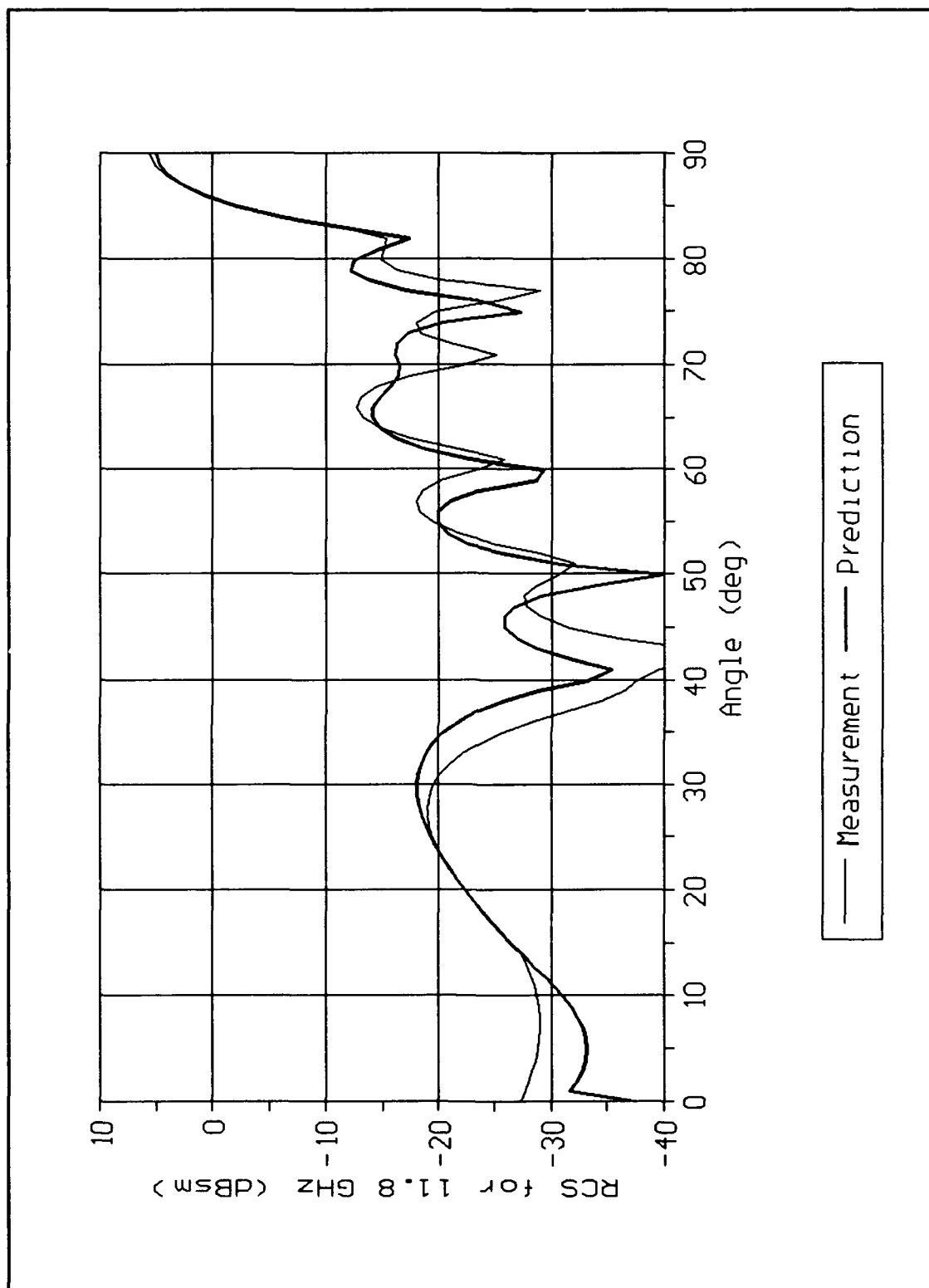


Figure 5.16. Comparison of measured and predicted monostatic scattering pattern for a 4 inches by 6 inches conducting strip with 1 inch by 6 inches loads, SF 10, and a perfect conductor backing at 11.8 GHz, H-polarization.

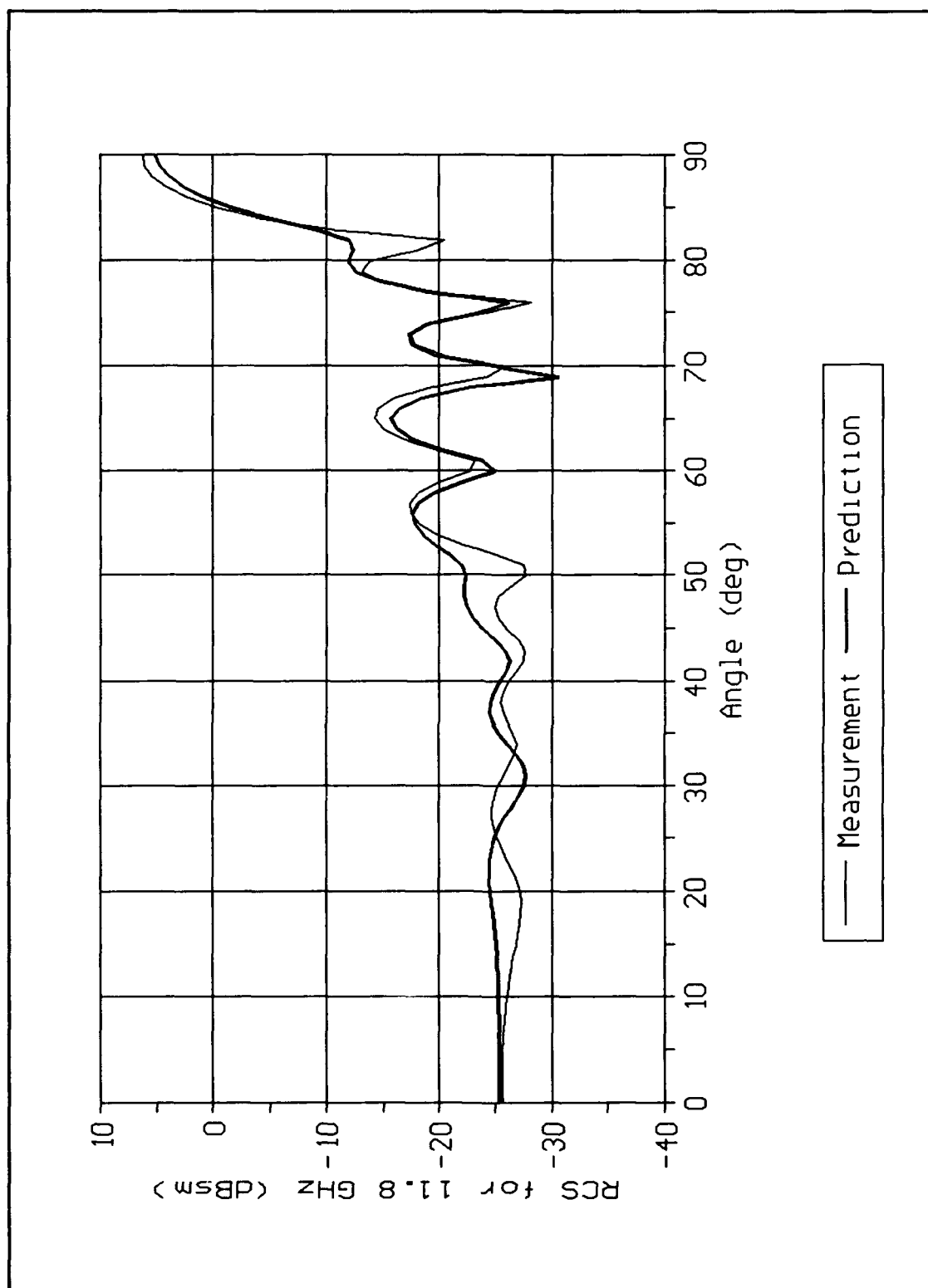


Figure 5.17. Comparison of measured and predicted monostatic scattering pattern for a 4 inches by 6 inches conducting strip with 1 inch by 6 inches loads, FG 40, at 11.8 GHz, E-polarization.

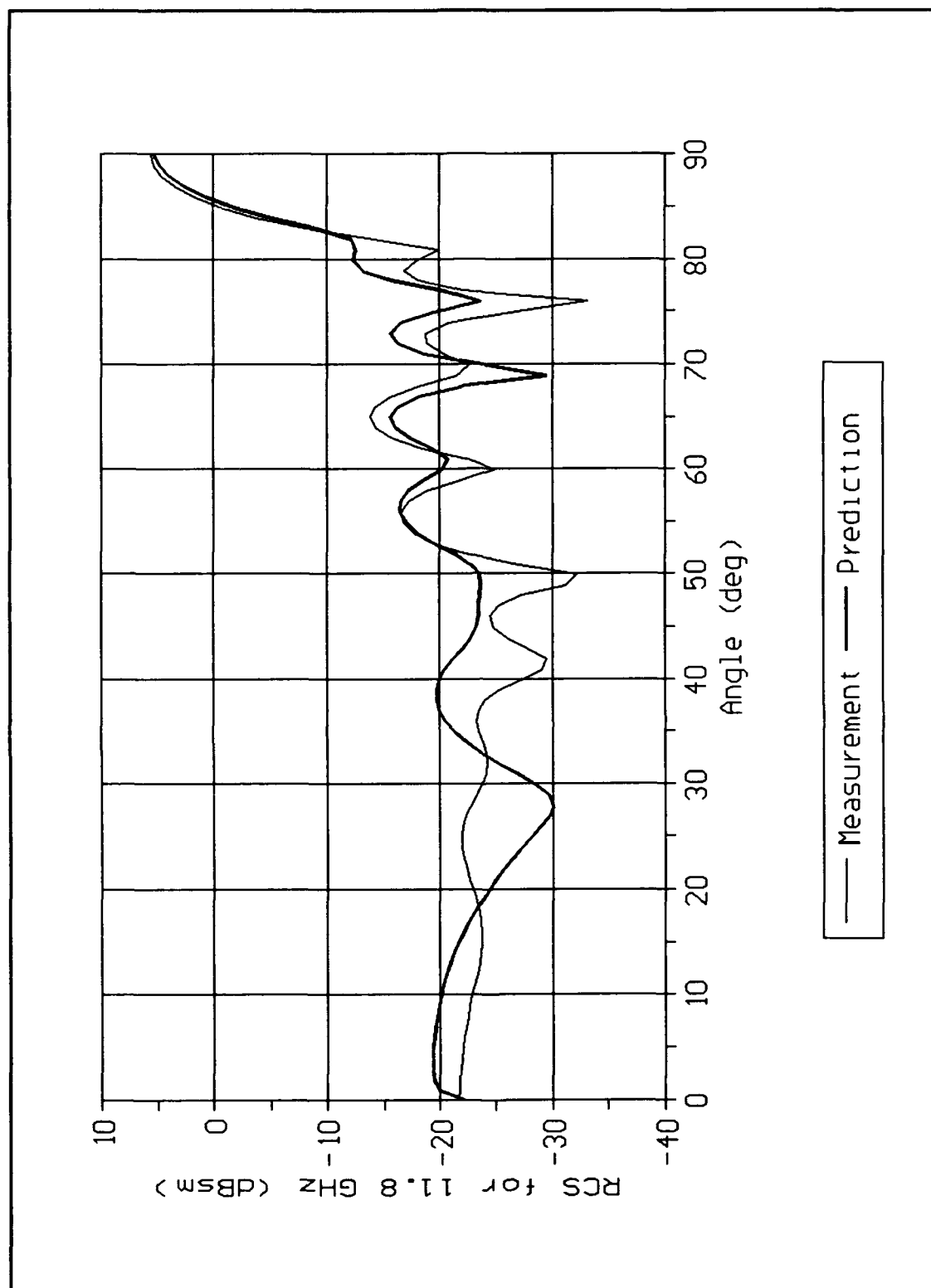


Figure 5.18. Comparison of measured and predicted monostatic scattering pattern for a 4 inches by 6 inches conducting strip with 1 inch by 6 inches loads, FG 40, and a perfect conductor backing at 11.8 GHz, E-polarization.

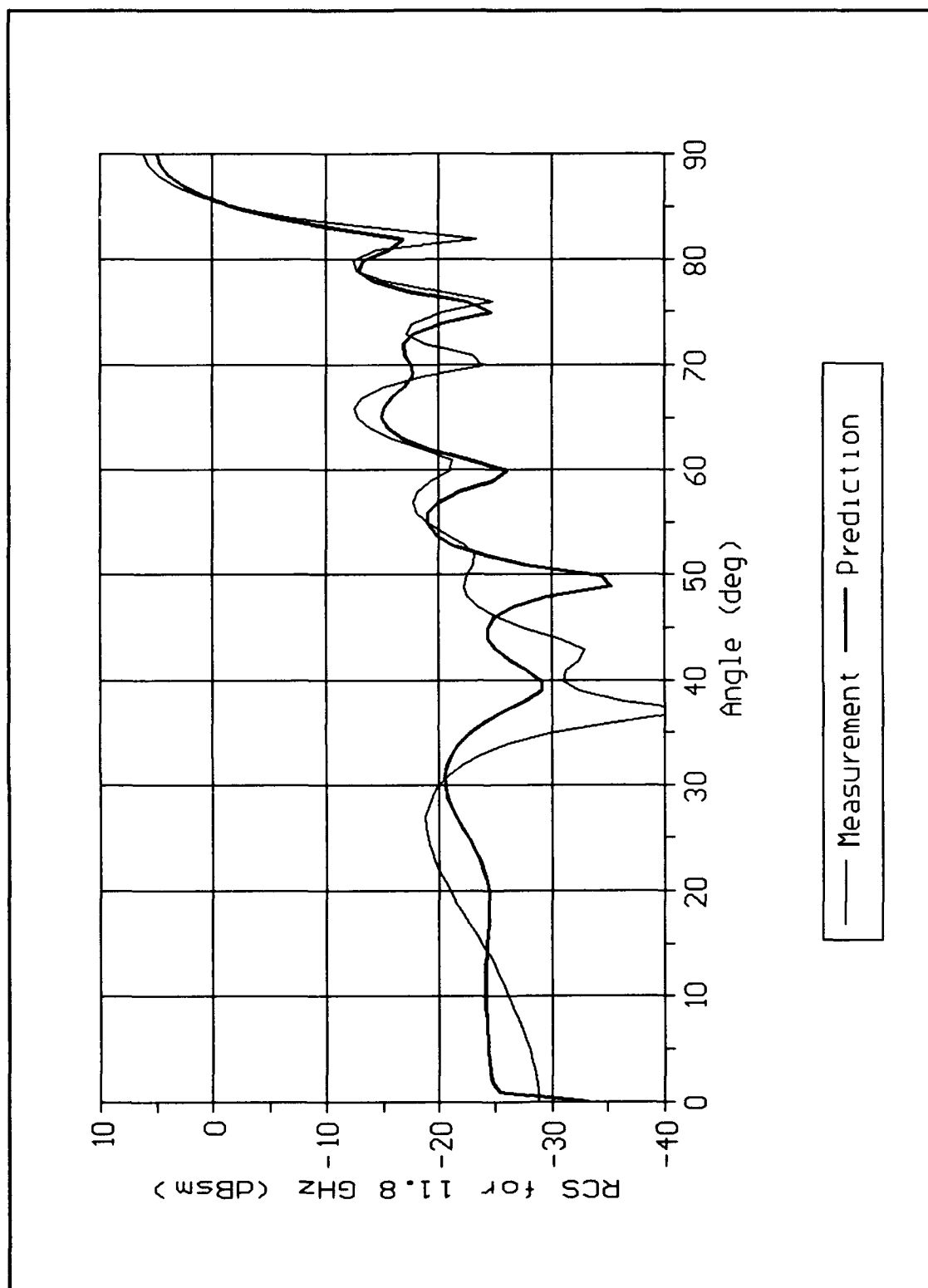


Figure 5.19. Comparison of measured and predicted monostatic scattering pattern for a 4 inches by 6 inches conducting strip with 1 inch by 6 inches loads, FG 40, at 11.8 GHz, H-polarization.

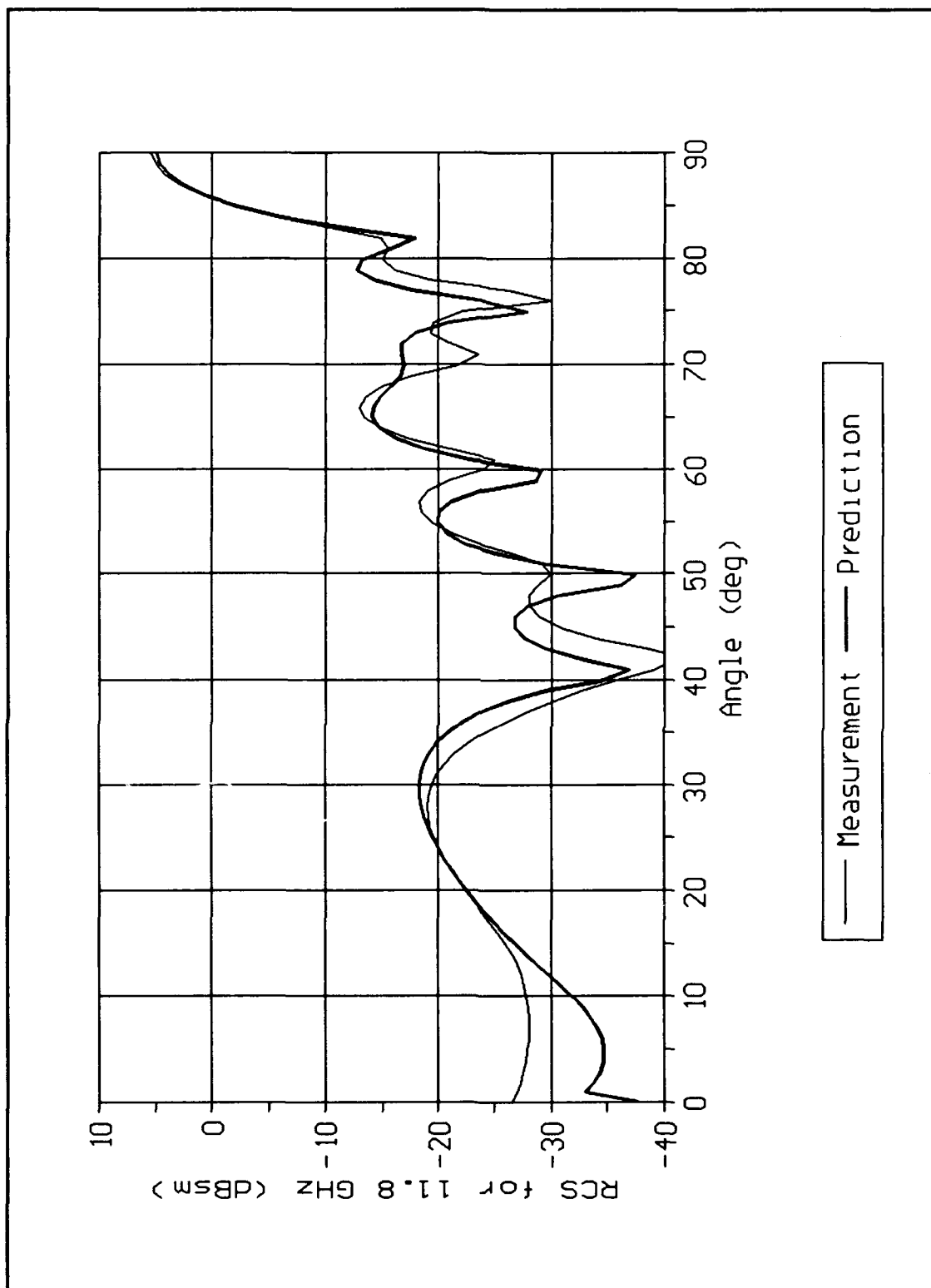


Figure 5.20. Comparison of measured and predicted monostatic scattering pattern of a 4 inches by 6 inches conducting strip with 1 inch by 6 inches loads, FG 40, and a perfect conductor backing at 11.8 GHz, H-polarization.

VI. Conclusions

Summary

This thesis investigated the scattering from impedance strips and impedance-loaded strips. The scattering from impedance strips was analyzed using the non-uniform primary diffraction and uniform secondary diffractions derived by Herman (5) for an impedance strip. Herman (5) derived a non-uniform primary diffraction for an impedance half plane from Senior's (19) impedance half plane formulation. Uniform secondary diffractions up to the third order on an impedance strip were derived by Herman (5) using the Extended Spectral Ray Method (ESRM).

The scattering from impedance loaded strips was analyzed using the non-uniform primary diffraction and uniform secondary diffractions derived by Herman (5) for an impedance polygon. Herman (5) derived a non-uniform primary diffraction for an impedance wedge from Maliuzhinets' (12) impedance wedge formulation. The uniform secondary diffractions up to the third order on the face of an impedance double wedge were derived by Herman (5) using the ESRM. A secondary diffraction which diffracts at three vertices before returning to the observer on an impedance polygon was derived by Herman (5) using the ESRM. This secondary diffraction is called a three vertex secondary diffraction. This secondary diffraction for an impedance polygon was revised in this thesis so it could be applied to an impedance-loaded strip.

Both the impedance half plane formulation and the impedance wedge

formulation use the Impedance Boundary Condition. The equivalent surface impedance was assumed constant for all incident angles in the diffraction mechanisms derived by Herman (5). For the predictions compared to measurements, the equivalent surface impedance was assumed to be the measured normal surface impedance of the material.

In this thesis, a Fortran code was written to predict the scattering from an impedance strip loaded with up to 100 loads. The diffractions mechanisms derived for the impedance double wedge and the revised three vertex secondary diffraction were used in the code. Herman (5) has written Fortran codes to predict the scattering from impedance strips and impedance polygons. Herman's (5) codes were used in this thesis to make predictions for impedance strips with and without conductor backings and loaded impedance strips with conductor backings.

Using Herman's impedance strip program and the developed impedance loaded strip program, several impedances and one loading scheme were investigated for scattering reduction by replacing a perfectly conducting strip with an impedance strip or an impedance loaded strip of equal length. The impedances and loading scheme chosen are not intended to be optimum. The impedances considered were large purely capacitive, large purely inductive, large real, and small real. The scattering for both strips using the capacitive and inductive impedances were polarization dependent. The impedances provided reduction in scattering for one polarization, but an increase in scattering for the other polarization. For the impedance strip, the real impedances provided

reduction in scattering for both polarizations. For the loaded impedance strips, the large real impedance formed a null at broadside, but the sidelobes in the scattering patterns were increased for both polarizations. The small real impedance provided reduction in the mainlobe, but the mainlobe beamwidth was increased for both polarizations.

Measurements were made to determine the accuracy of the diffraction mechanisms used in the predictions for impedance strips with and without a conductor backing and impedance loaded strips with and without a conductor backing. The impedance strip predictions compared well to the measurements for mainbeam levels and sidelobe structure. The impedance strip predictions agreed better to the measurements for E-polarization than H-polarization. The predictions for the impedance loaded strips with and without a conductor backing also compared well to the measurements for mainbeam levels and sidelobe structure for angles of 55 degrees off broadside. The predictions also were better for E-polarization than H-polarization. The differences in all predictions compared to the measurements are attributed to the equivalent surface impedance used in the predictions being modelled as a constant (not a function of incident angle) and being modelled as the normal surface impedance of the material.

The impedance wedge formulation provided predictions which compared well to measurements when the materials were resistive materials. On the other hand, the impedance half plane formulation did not give accurate predictions compared to measurements for resistive materials. This result is not explainable.

Recommendations for Further Study

The applications of tapered loads on perfectly conducting strips to reduce the scattering of a perfectly conducting strip can be investigated. The code written in this thesis for impedance loaded strips can be used in the analysis.

The equivalent surface impedance of a material could be modelled as a function of incident angle to achieve better accuracy in the predictions.

Bibliography

1. Anderson, Iain. "Plane Wave Diffraction by a Thin Dielectric Half-Plane," IEEE Transactions on Antennas and Propagation, 27: 584-589 (September 1979).
2. Harrington, Roger F. and Joseph R. Mautz. "Control of Radar Scattering by Reactive Loading," IEEE Transactions Antennas and Propagation, 20: 446-454 (July 1972).
3. Haupt, Randy L. and Valdis V. Liepa. Synthesis of Resistive Tapers to Control Scattering Patterns of Strips. PhD Thesis. University of Michigan, Ann Arbor MI, 1988.
4. Heaton, Mark C. Electromagnetic Scattering From Impedance Strips and Impedance-Loaded Conducting Strips. MS Thesis. School of Engineering, Air Force Institute Technology (AU), Wright-Patterson AFB OH, December 1990.
5. Herman, Martin I. High Frequency Scattering from Canonical Impedance PhD Thesis. University of Michigan, Ann Arbor MI, 1988.
6. Herman, Martin I. and John L. Volakis. "High-Frequency Scattering a by Resistive Strip and Extensions to Conductive and Impedance Strips," Radio Science, 22: 335-349 (May-June 1987).
7. Herman, Martin I. and John L. Volakis. "A Uniform Asymptotic Evaluation of Integrals," Proceedings of the IEEE, 74:1043-1044 (July 1986).
8. Hewlett Packard Product Note - 8510-3, "Material Measurements using the HP 8510B," August 1985.
9. Keller, J. B. "Geometrical Theory of Diffraction," Journal of the Optical Society of America, 52: 116-130 (February 1962).
10. Knott, Eugene F. and others. Radar Cross Section. Norwood MA: Artech House, 1985.
11. Kouyoumjian, Robert G. and Prabhakar H. Pathak. "A Uniform Geometrical Theory of Diffraction for an Edge in a Perfectly Conducting Surface," Proceedings of the IEEE, 62: 1448-1461 (November 1974).

12. Maliuzhinets, G. D. "Excitation, Reflection and Emission of Surface Waves from a Wedge with given Face Impedance," Soviet Physics Dolaky, 3: 752-755 (1958).
13. Medgyesi-Mitschang, L. N. and John M. Putnam. "Integral Equation Formulations for Imperfectly Conducting Spheres," IEEE Transactions on Antennas and Propagation, 32: 206-214 (February 1985).
14. Richmond, Jack H. "Scattering by Thin Dielectric Strips," IEEE Transactions on Antennas and Propagation, 33: 64-68 (January 1985).
15. Sebak, A. and L. Shafai. "Scattering from Arbitrarily-Shaped Objects with Impedance Boundary Conditions," IEE Proceedings, Part H, 136: 371-376 (October 1989).
16. Senior, Thomas B. A. "Approximate Boundary Conditions," IEEE Transactions on Antennas and Propagation, 29: 826-829 (Sept 1981).
17. Senior, Thomas B. A. "Backscattering from Resistive Strips," IEEE Transactions on Antennas and Propagation, 27: 808-813 (November 1979).
18. Senior, Thomas B. A. "Combined Resistive and Conductive Sheets," IEEE Transactions on Antennas and Propagation, 33: 577-579 (May 1985).
19. Senior, Thomas B. A. "Diffraction by a Semi-infinite Metallic Sheet," Proceedings of the Royal Society (London), 213: 436-458 (1952).
20. Senior, Thomas B. A. "Impedance Boundary Conditions for Imperfectly Conducting Surfaces," Applied Science Research, Section B, 8: 418-436 (1960).
21. Senior, Thomas B. A. "A Note on Impedance Boundary Conditions," Canadian Journal of Physics, 40: 663-665 (1962).
22. Senior, Thomas B. A. and Valdis V. Liepa. "Backscattering from Tapered Resistive Strips," IEEE Transactions on Antennas and Propagation, 32: 747-751 (July 1984).
23. Tiberio, Roberto and R. G. Kouyoumjian. "Calculation of High-Frequency Diffraction by Two Nearby Edges Illuminated at Grazing Incidence," IEEE Transactions on Antennas and Propagation, 32: 1186-1196, (1984).
24. Tiberio, Roberto and Giuseppe Pelosi. "High Frequency Scattering from the Edges of Impedance Discontinuities on a Flat Plane," IEEE Transactions on Antennas and Propagation, 31: 590-596 (July 1983).

25. Tiberio, Roberto and others. "A Uniform GTD Formulation for the Diffraction by a Wedge with Impedance Faces," IEEE Transactions on Antennas and Propagation, 33: 867-872 (August 1985).
26. Uzgoren, G. and others. "Diffraction Coefficient Related to a Discontinuity formed by Impedance and Resistive Halfplanes," IEE Proceedings, Part H, 136: 23 (February 1989).
27. Volakis, John L. and Thomas Senior. "Simple Expressions for a Function Occurring in Diffraction Theory," IEEE Transactions on Antennas and Propagation, 33: 678-680 (June 1985).
28. Volakis, John L., Associate Professor, Department of Electrical Engineering and Computer Science, University of Michigan. Personal conversation. Ann Arbor MI, 25 September 1991.